Synthesis and physicochemical evaluation of metal oxide powders which reveal antibacterial activity under dark conditions

Nguyen Phuong Thi Minh

Doshisha University

March 2020

<u>Contents</u>

CHAPTER 1

General Introduction

1.1 Antibacterial materials - overview

Microorganisms have a diverse existence, in form of bacteria, virus, fungi, algae and several other living species since millions of years ago, and have unprecedented influence in almost every aspects of human life. The majority of human diseases is related to infections with some kind of microorganisms in one way or another, directly or indirectly. Surface bio-contamination is being concerned as a severe problem that contributes to outbreaks of community and nosocomial or medical infections through contiguous fomite transmission of diseases. Each year, more than 90,000 patients died in the United States alone due to the nosocomial infections by pathogens [1, 2].

With that being talked, antibacterial materials which are defined as the subject materials for medical devices because of their nature against bacteria and the ability to resist infection. They are also used to effectively carry medical substances whose major function is to prevent, treat, or reduce the potential or existing infections. For this purpose, injectable or implantable antibacterial biomaterials should own a strong bactericidal ability to control pre-existing infections [3-6].

Currently, there are many antibacterial materials are somehow effective and serving as powerful tools to prevent infections. Inorganic metal oxides are being increasingly used for

antimicrobial applications. The main advantages of using inorganic oxides when compared with organic antimicrobial agents are their stability, robustness, and long shelf life. In addition, the antimicrobial activity of nanoparticles has been studied with different pathogenic and nonpathogenic bacteria such as Staphylococcus aureus and Escherichia coli. Some of the inorganic oxides that have been tested for their antimicrobial activity are TiO_2, ZnO, MgO, CaO, CuO, Al_2O_3, Ag_2O, and CeO_2 [7-10]. Among these, suspensions of TiO_2 are effective at killing bacteria and viruses under ultraviolet light. In the same way, the antibacterial activity of ZnO also has been studied with different pathogenic and nonpathogenic bacteria such as *S. aureus* and *E. coli* [10-12].

1.2 Antibacterial ZnO

1.2.1 Background of ZnO

Zinc oxide crystallizes in two main forms: hexagonal wurtzite and cubic zincblende (Fig. 1-1) in which hexagonal structure is stable at ambient conditions. With its unique physical and chemical properties such as high chemical stability, high electrochemical coupling coefficient, broad range of radiation absorption and high photostability, ZnO is a multifunctional material. In materials science, zinc oxide is categorized as a semiconductor in group II-VI, whose covalence is on the boundary between ionic and covalent semiconductors. Thanks to its broad energy band (3.37 eV), high bond energy (60 meV) [12], and high thermal and mechanical stability at room temperature, its application becomes highly potential in electronics, optoelectronics and laser technology [13-15]. The piezo- and pyroelectric properties of ZnO make it possible to be used as a sensor, converter, energy generator and photocatalyst in hydrogen production. Due to the hardness, rigidity and piezoelectric constant, it is an important

material in the ceramics industry. At the same time, its low toxicity, biocompatibility and biodegradability contribute to turn it into a desired material for biomedicine and in pro-ecological systems [12-17].
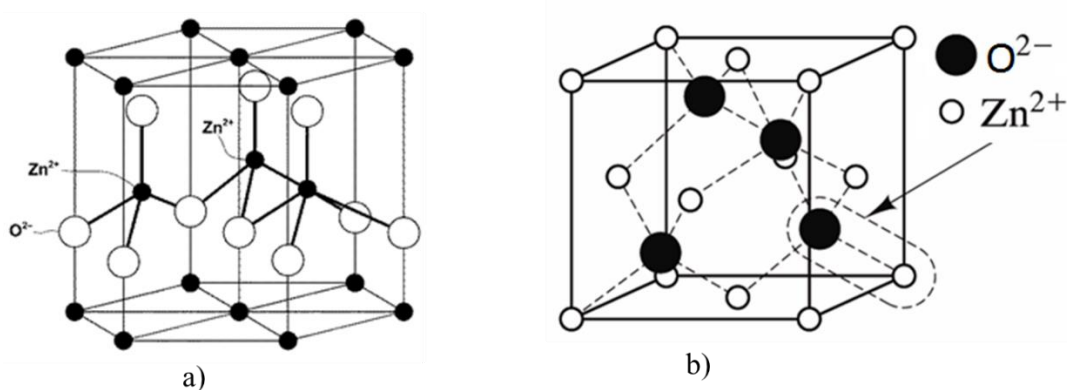
Fig. 1-1 a) Wurtzite and b) Zincblende structures.

1.2.2 Antibacterial activity of ZnO

Inorganic antimicrobial agents, such as metal oxides, are receiving more and more attention because they are not only stable under high temperatures and pressures, but also generally considered as safe for human beings and animals relative to organic substances. Zinc oxide (ZnO) is listed as "generally recognized as safe" by the United State Food and Drug Administration (21CFR182.8991) [14-16]. As a food additive, it is the most commonly used zinc source in the reinforcement of cereal-based foods. Because of its antimicrobial properties, ZnO has been integrated into the linings of food cans in packages for meat, fish, corn, and peas to preserve colors and to prevent spoilage. Nanometer-sized particles of ZnO have much more noticeable antimicrobial activities than large particles, since the small size (less than 100 nm) and high surface-to-volume ratio of nanoparticles allow them to better contact with bacteria. In

recent studies, these nanoparticles show some toxicity to bacteria but seems to have very small effects on human cells [16-20]. ZnO nanoparticles have shown to own a wide range of antibacterial activities against both Gram-positive and Gram-negative bacteria, including major foodborne pathogens like *Escherichia coli* O157:H7, *Salmonella*, *Listeria monocytogenes*, and *Staphylococcus aureus* [12, 16-20]. However, currently there is no information available on their antibacterial effect against species of *Campylobacter*. *Campylobacter jejuni* is a primary cause of microbial foodborne illness around the world. In fact, it has recently been shown that approximately 80% of poultry products are contaminated with this pathogen. Consumption of *Campylobacter*-contaminated food and water usually causes a mild to severe gastrointestinal infection in humans that can sometimes develop into a life-threatening disease called Guillain-Barré Syndrome [17-21]. Therefore, it is important to pay attention to the application of ZnO particles as a potential food safety intervention technology to effectively control Campylobacter and other microbial contaminants in foods. In order to better take advantage of ZnO nanoparticles in food products and to assist in the development of powerful, but nontoxic, antimicrobial derivatives, it is necessary to see up close the mechanism of ZnO nanoparticles against bacteria in action, but to date, the process underlying their antibacterial effect is not well understood. A few studies have suggested that the primary cause of the antibacterial function might be from the disruption of cell membrane activity.

Although there are a large number of studies regarding the antibacterial effect of ZnO, most attention has been on Escherichia coli and a relatively few reports on *S. aureus*. Little is known regarding interaction of nanoparticles with other bacteria, and importantly, less is known about the mechanism underlying the antimicrobial effects.

1.3 Antibacterial TiO$_2$

1.3.1 Mechanism of antibacterial activity

Strong oxidation and reduction power of photoexcited titanium dioxide (TiO$_2$) was concluded from the discovery of Honda-Fujishima effect. In 1972, Fujishima *et al*. reported on the photoinduced decomposition of water on TiO$_2$ electrodes [22, 23]. Since Frank and Bard first examined the possibilities of using TiO$_2$ to decompose cyanide in water, there has been an increasing interest in environmental applications [22, 23]. Photocatalytic reactions at the surface of titanium dioxide have been drawing strong attention in the view of their practical applications to environmental cleaning such as self-cleaning of tiles, glasses, and windows. Titanium dioxide TiO$_2$ represents an effective photocatalyst for water and air purification and for self-cleaning surfaces. Additionally, it can be used as antibacterial agent because of its strong oxidation activity and super hydrophilicity. This substance shows relatively high reactivity and chemical stability under ultraviolet light ($\lambda < 387$nm), whose energy exceeds the band gap of 3.3 eV in the anatase crystalline phase. The development of photocatalysts displaying high reactivity under visible light ($\lambda > 400$ nm) should allow the main part of the solar spectrum to be used, even under weak illumination of interior lighting [24-27]. Several approaches for TiO$_2$ modification have been proposed: metal-ion implanted TiO$_2$ (using transition metals: Cu, Co, Ni, Cr, Mn, Mo, Nb, V, Fe, Ru, Au, Ag, Pt), reduced TiO$_x$ photocatalysts, non-metal doped-TiO$_2$ (N, S, C, B, P, I, F), composites of TiO$_2$ with semiconductor having lower band gap energy (e.g. Cd-S particles, sensitizing of TiO$_2$ with dyes (e.g. thionine) and TiO$_2$ doped with up conversion luminescence agent [25-31].

The photocatalytic mechanism is initiated by the absorption of the photon hv_1 with

energy equal to or greater than the band gap of TiO_2 (~3.3 eV for the anatase phase) producing

an electron-hole pair on the surface of TiO_2 nanoparticle as schematized in Fig. 1-2.
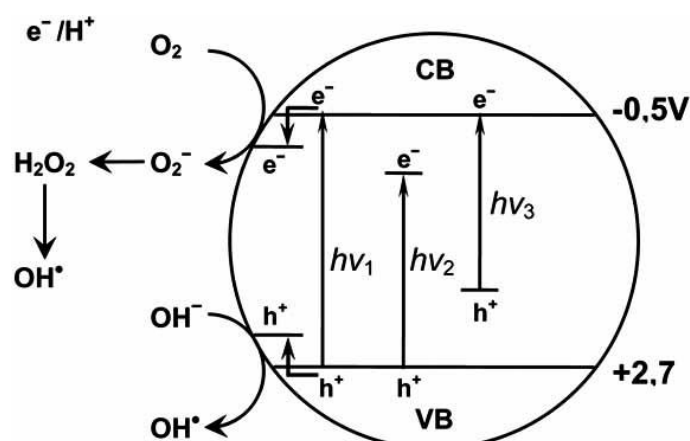
Fig. 1-2 Submission mechanism of reactive oxygen species (hydroxyl radical ·OH, super

oxide O_2^-, hydrogen peroxide H_2O_2 and singlet oxygen $^1O_2$) from the surface of TiO_2

photocatalysis: hv_1: pure TiO_2; hv_2: metal-doped TiO_2 and hv_3: nonmetal-doped TiO_2.

An electron is promoted to the conduction band (CB) while a positive hole is created in

the valence band (VB). Excited-state electrons and holes can recombine and dissipate the input

energy as heat, get trapped in metastable surface states, or react with electron donors and

electron acceptors adsorbed on the semiconductor surface or within the surrounding electrical

double layer of the charged particles. After reaction with water, these holes can produce

hydroxyl radicals with high redox oxidizing potential [32-36].

Depending upon the exact conditions, the holes, hydroxyl radical ·OH, super oxide O_2^-,

hydrogen peroxide H_2O_2 and singlet oxygen $^1O_2$ themselves can play important roles in the

microbial activity with cell as shown in Fig. 1-3.
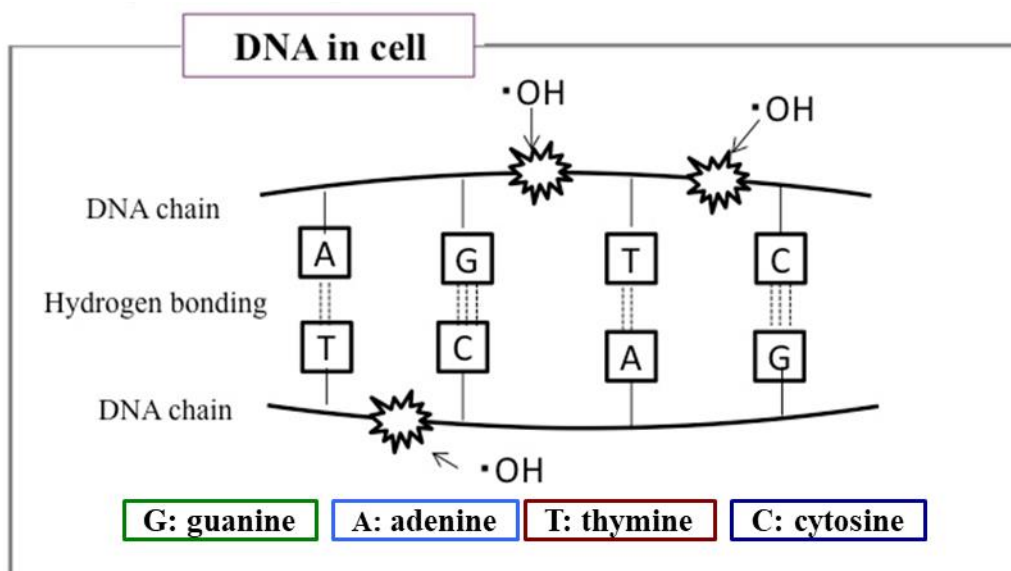
Fig. 1-3 Mechanism of microbial activity of ·OH.

1.3.2 Doped TiO$_2$ – a review

Matsunaga *et al.* first reported the bactericidal activity of a UV-responsive TiO$_2$ photocatalyst in 1985 [37]. This has since become one of the most researched aspects of TiO$_2$ photocatalysis. Foster *et al.* (2011) [38] reviewed the photocatalytic disinfection of more than 60 bacterial species, including Gram-positive and Gram-negative bacteria, using a wide range of UV-responsive TiO$_2$ materials and substrates.

Several other groups around the world have also conducted studies on the application of impurity-doped visible light-responsive TiO$_2$ photocatalysts in bacterial inactivation (Cheng *et al.* 2009 [39], 2012; Hamal *et al.* 2010 [40]; *Hu et al.* 2006 [41]; Pan *et al.* 2010 [42]; Wong *et al.* 2006 [43]; Wu *et al.* 2010a, b [44]; Yu *et al.* 2005 [45]). These studies have also

investigated possible photocatalytic bactericidal effects against the model bacteria *E. coli* using silver-modified TiO_2 (Pan *et al.* 2010 [42]; Wu *et al.* 2010b [46]), Ag/N-co-doped TiO_2 (Wu *et al.* 2010a) [44], Ag/C/S-co-doped TiO_2 (Hamal *et al.* 2010) [40], AgI/TiO_2 (Hu *et al.* 2007) [47], and Ag/AgBr/TiO_2 visible light-responsive photocatalysts (Hu *et al.* 2006) [41]. In 2006, Wong *et al.* [43] reported using an N-doped visible light-responsive TiO_2 photocatalyst to reduce the numbers of several human pathogens including *Shigella flexneri, Listeria monocytogenes, Vibrio parahaemolyticus, Staphylococcus aureus, Streptococcus pyogenes*, and *Acinetobacter baumannii* [43]. Not long after, in 2009, Cheng *et al.* [39] supported and reinforced prior studies by investigating the antibacterial activity of the visible light-irradiated C-doped TiO_2 on human pathogens, including the common *Shigella flexneri, Acinetobacter baumannii*, and *Staphylococcus aureus*; observing that photocatalysis was effective against these strains [39]. Among these microorganisms, *Shigella flexneri, Listeria monocytogenes*, and *Vibrio parahaemolyticus* usually exist in contaminated water, plants, and sewage (Chiou *et al.* 2001 [48]; Lima 2001 [49]; Martino *et al.* 2005 [50]; Wong *et al.* 2000 [51]), and frequently cause outbreaks in areas with poor public health conditions. The *Shigella pyogenes* and *Staphylococcus aureus* species are exotoxin producing pathogens which can cause soft tissue infections, foodborne disease, and toxic shock syndrome (Salyers and Whitt 1994) [52]. Multidrug-resistant *Acinetobacter baumannii* causing nosocomial infections are rapid spreading and becoming a great concern in public health (NavonVenezia *et al.* 2005) [53].

Many researches have provided evidences to strongly suggest the effectiveness of the N-doped TiO_2 photocatalysts against *Bacillus subtilis, Bacillus thuringiensis, Bacillus cereus*, and *Bacillus a*nthracis under visible light illumination (Kau *et al.* 2009) [54]. To improve the bactericidal performance of the visible light-responsive TiO_2 photocatalysts, a newer study

synthesized silver nano structure coated N- and C-doped TiO_2 photocatalysts, testing them against the human pathogens *Shigella pyogenes, Staphylococcus aureus,* and multidrug-resistant *Acinetobacter bauman*nii isolated from hospitals (Wong *et al.* 2010) [55].

In addition, the current problem with doped TiO_2 may be the loss of photoactivity during recycling and long-term storage. It was assumed that the efficiency of metal doped-TiO_2 under visible light strongly depended on the preparation method used. In the same cases, such doped photocatalysts showed no activity under visible light and/or lower activity in the UV spectral range compared to the non-doped TiO_2 because of high carrier recombination rates through the metal ion levels. The main present problem with nonmetal-doped TiO_2 photocatalyst is that the photocatalytic activity under visible light is much lower than that under ultraviolet light [56-57]. One of the major challenges for the scientific and industrial community involved in photocatalytic research is to increase the spectral sensitivity of TiO_2-based photocatalysts. A major area of future research would be the development of new dopants, new method of dopant incorporation into TiO_2 structure as well as new application for environmental technology. For that reason, future patents would deal with visible light-activated TiO_2 functioning in the presence of solar irradiation [57-59]. The most important challenge which faces titania-based catalysis is to stablize TiO_2 with predictable photoactivity in UV, visible light or even in the dark.

1.4 Purposes of the present research

Both ZnO and TiO_2 have high potential as antibacterial agents which can be applied in various fields. Although there are already many studies about these materials focusing on their antibacterial activity, they are still getting more attention from researchers due to their unclear

mechanism under dark. There have been very few reports mentioning clearly about this. Besides, the effects of the preparation methods and their physicochemical properties to the antibacterial property of ZnO, TiO$_2$ and doped TiO$_2$ in the shade also have not been well-characterized.

In the present study, synthesis and physicochemical evaluation of metal oxides which reveal antibacterial activity even under dark conditions have been performed.

1.5 Outline of the work

In Chapter 2, fine ZnO powders were prepared from plate-like ZnO particles by hydrothermal-treatment in 3 mol/L Zn(NO$_3$)$_2$ aqueous solution at 170°C for 7 h (443 K for 25.2×10^3 s), followed by the heating at 400~700°C for 1 h (673~973 K for 3.6×10^3 s) in air. They showed strong antimicrobial activity in the sunshade; those disinfect many kinds of bacteria even MRSA. The origin of antibacterial activity might be explained in terms of the generation of most powerful reactive oxygen species (ROS) of hydroxyl radical (·OH). As the intensity of chemiluminescence (CL) corresponds to the amount of ROS, the antibacterial activity was estimated by measuring the CL emitted from the surface of ZnO using luminol reaction under dark. Both electron spin resonance (ESR) spectroscopy and CL detection were used for identification of ROS. Furthermore, in order to increase the CL values, the ZnO powders were ball-milled (BM) under the various conditions. It was cleared that the suitable BM conditions, such as BM time and ball size, could improve CL values greatly in comparison with those of ZnO without BM. This effect can be caused by both increasing surface area of ZnO powder and the lattice strain from "Debye effect".

In Chapter 3, the relationship between the disinfect activity of four types of ZnO powders and their physicochemical properties was studied using XRD (X-Ray Diffraction),

SEM (Scanning Electron Microscope), BET (Brunauer-Emmett-Teller), CL (Chemiluminescence), ESR (Electron Spin Resonance), and XPS (X-ray Photoelectron Spectroscopy) and bio-test using *E. coli*. Four ZnO powders tested were as follows: No. 1 was newly developed ZnO, prepared via hydrothermal treatment in aqueous $Zn(NO_3)_2$ solution and then re-oxidized, which revealed a strong antimicrobial activity under dark conditions; No. 2 was starting material for No.1, derived from zinc acetate; No. 3 was fine ZnO prepared at low-temperature heating of basic zinc carbonate; No. 4 was conventional fine ZnO synthesized from vaporized metal Zn in air. All powders revealed antimicrobial activity in the dark; different amounts and kinds of ROS have been emitted from each ZnO powder. However, it was cleared that its sustainability depends significantly on the contents of interstitial Zn contained in ZnO particles.

In Chapter 4, Li^+, Mg^{2+}, Ga^{3+} and Al^{3+} impurities were doped into the structure of ZnO. These doped ZnO powders were eluted to water and their catalytic properties using acetaldehyde and comparing with TiO_2 powders were investigated: i) a small amount of Mg only could form solid solution, revealing around 5% increase of chemiluminescence values, ii) the addition of 0.3 mas% cellulose nano-fiber (CNF) aqueous solution could bring to fabricate the granules which showed high CL and low elution to water, and iii) it has been cleared that these anti-germ ZnO powders could play a role of catalytic properties for decomposition of acetaldehyde even under dark conditions.

In Chapter 5, anatase-type titanium dioxide (*a*-TiO_2) sub-micron powders with strong antibacterial activity under dark conditions were prepared by single addition of K or P, and combined doping of a small amount of K and P with the atomic ratio of K/P=1/3 into high purity

($\geq$99.92%) a-TiO$_2$ powder, followed by heating at 973 K for 3.6×10^3 s in air or oxygen atmosphere. The combined doping was based on the idea that to adjust both i) the average ionic radius $<r>$ of $[1\cdot K^+ + 3\cdot P^{5+}]/4 = 0.063$ nm and ii) the valence of guest metal ions $[1\times(1+) + 3\times(5+)]/4 = 4+$ corresponding to those $[r(Ti^{4+})_{VI} = 0.0605$ nm and $4+]$ of Ti^{4+}. The microstructure and physicochemical properties such as lattice parameters, particle sizes, and oxygen deficiency, of thus prepared all powders have been examined using XRD, SEM, BET, XPS, FT-IR, XAFS and chemiluminescence (CL). The amount of reactive oxygen species (ROS) of co-doped a-TiO$_2$ after heating in oxygen atmosphere in which the values were evaluated by using CL under dark conditions reached about 10 times higher than pure a-TiO$_2$. The mechanism of generation of ROS from the doped a-TiO$_2$ powder was also proposed.

In Chapter 6, the improvements in the preparation methods and physicochemical properties of antibacterial ZnO and TiO$_2$ and their effects to the antibacterial activities of those powders were summarized. Besides, the antibacterial mechanism of ZnO and doped a-TiO$_2$ powders and the prospects for their applications were discussed.

References

1. M. Hellmann, S. D. Mehta, D. M. Bishai, S. C. Mears, J. M. Zenilman, The estimated magnitude and direct hospital costs of prosthetic joint infections in the United States, 1997 to 2004, J. Arthropl., 25(2010), 766-771.

2. L. G. Harris, R. G. Richards, Staphylococci and implant surfaces: a review, Injury, 37(2006), (Suppl. 2), S3-14.

3. R. O. Darouiche, Current concepts - treatment of infections associated with surgical implants, New England J. Med., 350(2004), 1422-1429.

4. J. W. Costerton, Bacterial biofilms: a common cause of persistent infections, Science, 284(1999), 1318–1322.

5. I. Uckay, P. Hoffmeyer, D. Lew, D. Pittet, Prevention of surgical site infections in orthopaedic surgery and bone trauma: state-of-the-art update, J. Hosp. Infect., 84(2013), 5-12.

6. J. M. Yin, Z. T. Liu, S. C. Zhao, Y. J. Guo, Diagnosis, management, and prevention of prosthetic joint infections, Frontiers Biosci., 18(2013), 1349-1357.

7. C. R. Arciola, D. Campoccia, P. Speziale, L. Montanaro, J. W. Costerton, Biofilm formation in Staphylococcus implant infections. A review of molecular mechanisms and implications for biofilm resistant materials, Biomaterials, 33(2012), 5967-5982.

8. W. Lv, J. Luo, Y. Deng, Y. Sun, Biomaterials immobilized with chitosan for rechargeable antimicrobial drug delivery, J. Biomed. Mater. Res. A, 101A(2013), 447-455.

9. K. Bazaka, M. V. Jacob, R. J. Crawford, E. P. Ivanova, Efficient surface modification of biomaterial to prevent biofilm formation and the attachment of microorganisms, Appl. Microbiol. Biotechnol., 95(2012), 299-311.

10. F. Variola, J. B. Brunski, G. Orsini, P. Tambasco de Oliveira, R. Wazen, A. Nanci, Nanoscale surface modifications of medically relevant metals: state-of-the art and perspectives, Nanoscale, 3(2011), 335-353.

11. W. Xiao, Y. F. Gu, D. P. Wang, W. H. Wang, H. B. Pan, W. J. Lu, Application of borate glass in the field of biomaterials, J. Clinic. Rehabilit. Tissue Eng. Res., 13(2009), 6741-6744.

12. T. Jin, D. Sun, J. Y. Su, H. Zhang, H. J. Sue, Antimicrobial efficacy of zinc oxide quantum dots against Listeria monocytogenes, Salmonella Enteritidis, and Escherichia coli O157:H7, J. Food Sci., 74(2009), 46-52.

13. N. Jones., B. Ray, K. T. Ranjit, A. C. Manna, Antibacterial activity of ZnO nanoparticle suspensions on a broad spectrum of microorganisms, FEMS Microbiol. Lett., 279(2008), 71-76.

14. Y. Liu, Antibacterial activities of zinc oxide nanoparticles against Escherichia coli O157:H7, J. Appl. Microbiol., 107(2009), 1193-1201.

15. S. Nair, Role of size scale of ZnO nanoparticles and microparticles on toxicity toward bacteria and osteoblast cancer cells, J. Mater. Sci. Mater. Med., 20(2009) (Suppl. 1), 235-241.

16. H. K. Nogva, S. M. Dromtorp, H. Nissen, K. Rudi, Ethidium monoazide for DNA-based differentiation of viable and dead bacteria by 5-nuclease PCR, Biotechniques 34(2003), 804-813.

17. N. Padmavathy, R. Vijayaraghavan, Enhanced bioactivity of ZnO nanoparticles-an antimicrobial study, Sci. Technol. Adv. Mater., 9(2008), 1-7.

18. R. G. Petersdorf, J. C. Sherris, Methods and significance of in vitro testing of bacterial sensitivity to drugs, Am. J. Med., 39(1965), 766-779.

19. D. Purdy, S. Cawthraw, J. H. Dickinson, D. G. Newell, S. F. Park, Generation of a superoxide dismutase (SOD)-deficient mutant of Campylobacter coli: evidence for the significance of SOD in Campylobacter survival and colonization, Appl. Environ. Microbiol., 65(1999), 2540-2546.

20. K. M. Reddy, Selective toxicity of zinc oxide nanoparticles to prokaryotic and eukaryotic systems, Appl. Phys. Lett., 90(2007), 2139021-2139023.

21. J. Sawai, Quantitative evaluation of antibacterial activities of metallic oxide powders (ZnO, MgO and CaO) by conductimetric assay, J. Microbiol. Methods 54(2003), 177-182.

22. A. Fujishima, K. Honda, Electrochemical photolysis of water at a semiconductor electrode, Nature, 283(1972), 37-38.

23. S. N. Frank, A. J. Bard, Heterogeneous photocatalytic oxidation of cyanide ion in aqueous solutions at titanium dioxide powder, J Am Chem Soc., 99(1977), 303-304.

24. A. Fujishima, C. R. Zhang, Titanium dioxide photocatalysis: Present situation and future approaches, Chimie, 9(2006), 750-760.

25. M. Anpo, Use of visible light. Second-generation titanium dioxide photocatalysts prepared by the application of an advanced metal ion-implantation method, Pure Appl. Chem., 72(2000), 1787-1792.

26. M. D. H. A. Fuerte, A. J. Maira, A. Martinez-Arias, M. Fernadez-Garcia, J. C. Conesa, J. Soria, Visible light-activated nanosized doped-TiO_2 photocatalysts, Chem. Commun., 24(2001), 2718-2719.

27. H. Yamashita, M. Harada, J. Misaka, Application of ion beam techniques for preparation of metal ion-implanted TiO_2 thin film photocatalyst available under visible light irradiation: Metal ion-implantation and ionized cluster beam method, J. Synchrotron Rad., 8(2001), 569-571.

28. T. Ihara, M. Miyoshi, M. Ando, S. Sugihara, Y. Iriyama, Preparation of a visible-light-active TiO_2 photocatalyst by RF plasma treatment, J. Mater. Sci., 2001, 4201-4207.

29. K. Takeuchi, I. Nakamura, O. Matsumoto, S. Sugihara, M. Ando, T. Ihara, Preparation of visible-light-responsive titanium oxide photocatalysts by plasma treatment, Chem. Lett., 29(2000), 1354-1355.

30. T. Ohno, T. Mitsui, M. Matsumura, Photocatalytic activity of S-doped TiO_2 photocatalyst under visible light, Chem Lett., 32(2003), 364-365.

31. Y. Liu, X. Chen, J. Li, C. Burda, Photocatalytic degradation of azo dyes by nitrogen-doped TiO_2 nanocatalysts, Chemosphere, 61(2005), 11-18.

32. J. C. Yu, L. Zhang, Z. Zheng, J. Zhao, Synthesis and characterization of phosphated mesoporous titanium dioxide with high photocatalytic activity, Chem. Mater., 15(2003), 2280 -2286.

33. T. Hirai, K. Suzuki, I. Komasawa, Preparation and photocatalytic properties of composite CdS nanoparticles-titanium dioxide particles, J. Colloid Interface Sci., 244(2001), 262-265.

34. F. D. Angelis, C. D. Valentin, S. Fantacci, A. Vittadini, A. Selloni. Theoretical studies on anatase and less common TiO_2 phases: Bulk, surfaces, and nanomaterials, Chem. Rev., 19(2014), 9708-9753.

35. Z. Zheng, J. Zhao, Y. Yuan, H. Liu, D. Yang, S. Sarina, H. Zhang, E. R. Waclawika, H. Zhu., Tuning the surface structure of nitrogen‐doped TiO_2 nanofibres - An effective method to enhance photocatalytic activities of visible‐light‐driven green synthesis and degradation, Chem. Eur. J., 19(2013), 5731-5741.

36. B. Zheng, Q. Guo, D. Wang, H. Zhang, Y. Zhu, S. Zhou, Energy‑transfer modulation for enhanced photocatalytic activity of near‑infrared upconversion photocatalyst, J. Am. Ceram. Soc., 1(2015), 136-140.

37. T. Matsunaga, R. Tomoda, T. Nakajima, Photoelectro-chemical sterilization of microbial cells by semiconductor powders, FEMS Microbiol Lett, 29(1985), 211-214.

38. H. A. Foster, I. B. Ditta, S. Varghese, Photocatalytic disinfection using titanium dioxide: spectrum and mechanism of antimicrobial activity, Appl. Microbiol. Biotechnol., 90(2011), 1847-1868.

39. C. L. Cheng, D. S. Sun, W. C. Chu, The effects of the bacterial interaction with visible-light responsive titania photocatalyst on the bactericidal performance, J. Biomed. Sci., 16(2009), 7.

40. D. B. Hamal, J. A. Haggstrom, G. L. Marchin, A multifunctional biocide/sporocide and photocatalyst based on titanium dioxide (TiO_2) codoped with silver, carbon, and sulfur, Langmuir, 26(2010), 2805-2810.

41. C. Hu, Y. Lan, J. Qu, Ag/AgBr/TiO_2 visible light photocatalyst for destruction of azodyes and bacteria, J. Phys. Chem. B, 110(2006), 4066-4072.

42. X. Pan, I. Medina-Ramirez, R. Mernaugh, Nanocharacterization and bactericidal performance of silver modified titania photocatalyst, Colloids Surf. B Biointerfaces, 77(2010), 82-89.

43. M. S. Wong, W. C. Chu, D. S. Sun, Visible-light-induced bactericidal activity of a nitrogen-doped titanium photocatalyst against human pathogens, Appl. Environ. Microbiol., 72(2006), 6111-6116.

44. P. Wu, R. Xie, K. Imlay, Visible-light-induced bactericidal activity of titanium dioxide codoped with nitrogen and silver, Environ. Sci. Technol., 44(2010a), 6992-6997.

45. J. C. Yu, W. Ho, J. Yu, Efficient visible-light-induced photocatalytic disinfection on sulfur-doped nanocrystalline titania, Environ. Sci. Technol., 39(2005), 1175-1179.

46. T. S. Wu, K. X. Wang, G. D. Li, Montmorillonite-supported Ag/TiO_2 nanoparticles: an efficient visible-light bacteria photodegradation material, ACS Appl. Mater. Interfaces, 2(2010b), 544-550.

47. C. Hu, J. Guo, J. Qu, Photocatalytic degradation of pathogenic bacteria with AgI/TiO_2 under visible light irradiation, Langmuir, 23(2007), 4982-4987.

48. C. S. Chiou, W. B. Hsu, H. L. Wei, Molecular epidemiology of a Shigella flexneri outbreak in a mountainous township in Taiwan, Republic of China, J. Clin. Microbiol. 39(2001), 1048-1056.

49. A. A. Lima, Tropical diarrhoea: new developments in traveller's diarrhea, Curr. Opin. Infect. Dis., 14(2001), 547-552.

50. M. C. Martino, G. Rossi, I. Martini, Mucosal lymphoid infiltrate dominates colonic pathological changes in murine experimental shigellosis, J. Infect. Dis., 192(2005), 136-148.

51. H. C. Wong, S. H. Liu, T. K. Wang, Characteristics of Vibrio parahaemolyticus O3:K6 from Asia, Appl. Environ. Microbiol., 66(2000), 3981-3986.

52. A. A. Salyers, D. D. Whitt, In bacterial pathogenesis: a molecular approach, ASM Press, Washington, DC, (1994).

53. S. Navon-Venezia, R. Ben-Ami, Y. Carmeli, Update on Pseudomonas aeruginosa and Acinetobacter baumannii infections in the healthcare setting, Curr. Opin. Infect. Dis., 18(2005), 306-313.

54. J. H. Kau, D.S. Sun, H. H. Huang, Role of visible lightactivated photocatalyst on the reduction of anthrax sporeinduced mortality in mice, PLoS One 4(2009), e4167.

55. M. S. Wong, D. S. Sun, H. H. Chang, Bactericidal performance of visible-light responsive titania photocatalyst with silver nanostructures, PLoS One, 5(2010), e10394.

56. L. Liu, X. B. Chen, Titanium dioxide nanomaterials: Self-structural modifications, Chem. Rev., 114(2014), 9890-9918.

57. F. Zuo, K. Bozhilov, R. J. Dillon, L. Wang, P. Smith, X. Zhao, C. Bardeen, P. Y. Feng, Active facets on titanium (III)-doped TiO_2: An effective strategy to improve the visiblelight photocatalytic activity, Angew. Chem. Int. Ed., 124(2012), 6327-6330.

58. H. Yamashita, M. Harada, J. Misaka, M. Takeuchi, K. Ikeue, M. Anpo, Degradation of propanol diluted in water under visible light irradiation using metal ion-implanted titanium dioxide photocatalysts. J. Photochem. Photobiol. A, 148(2002), 257-261.

59. J. Zhu, W. Zheng, B. He, J. Zhang, M. Anpo, Characterization of $FeTiO_2$ photocatalysts synthesized by hydrothermal method and their photocatalytic reactivity for degradation of XRG dye diluted in water, J. Mol. Catal. A, 216(2004), 35-43.

CHAPTER 2

Preparation of ZnO Powders with Strong Antibacterial Activity under Dark Conditions

2.1 Introduction

In the recent decades, one of the most significant challenges faced by the world is the recurrence of infectious diseases and the bacterial contamination in all kinds of materials [1]. Therefore, several antibacterial agents are widely used in day-to-day life for the prevention of public health issues caused by the ubiquity of micro-organisms and their ability to establish themselves [2]. When antibacterial agents are used in the new packaging materials for health care and food applications, the most crucial parameters to be taken care of are low toxicity to human beings and high efficiency in controlling bacteria. The increasing use of inorganic antibacterial agents is of great interest because of their creditability towards safety and stability when compared with organic antibacterial agents. New nanostructured materials with antibacterial properties are the need of the day for preventing microbial growth because the size, structure and surface properties of nanomaterials can improve the antimicrobial efficacy [3].

Several inorganic metal oxides such as TiO_2, MgO, ZnO and CuO have gained increasing attention in recent years. Of these oxides, bio-safe antimicrobial ZnO nanomaterials have been much focused from the viewpoints of human health because they can interact with biomolecules chemically as well as physically. It has been believed that chemical interactions of ZnO with bacterial cell lead to the photo-induced production of reactive oxygen species (ROS), formation of hydroxyl radical ($\cdot$OH), or related hydrogen per oxide (H_2O_2) like TiO_2

and release of Zn^{2+} ions. In contrast, their physical interaction can reveal biocidal function through rupturing cell envelope, cellular internalization or mechanical damage. However, the mechanism of antimicrobial activity of ZnO has been still debatable.

Up to now, there have been a few comprehensive reviews [1, 2] and many papers concerning about the preparation and mechanism of antibacterial activity of ZnO nanomaterials, such as i) (aqueous) solution route [3-5], ii) precipitation method [6-10], iii) wet chemical method [11-13], iv) hydrothermal method [14-17], and v) others: microwave [18], solvothermal synthesis [19], DC-magnetron sputter [20], etc. Their antimicrobial activity has been investigated from the viewpoints of particle size and surface defect structures using various kinds of Gram-positive (*S. aureus* and *B. subtilis*) and Gram-negative (*E. coli* and *A. aerogenes*) bacteria under UV radiation or in the sunshade. The synthesis route plays an important role in controlling the particle size and the morphology. In order to control the particle size, several techniques have been used for the synthesis of ZnO nanopowders/nanoparticles such as sonochemical synthesis [14], hydrothermal method [15], combustion synthesis [16], sol–gel synthesis [17], polyol method [18] and simple soft chemical route [19, 20]. Of these methods, hydrothermal treatment offers several advantages. It is a very fascinating, facile and inexpensive method which is suitable to grow nanostructured materials in large scale [21]. However, only little information is available for preparation of ZnO powders hydrothermally treated in the aqueous solutions contained Zn^{2+} ions and followed by re-oxidation and ball-milling, except for our previous papers [21, 22]; which paper mentioned only hydrothermal treatment of ZnO at low temperatures.

Based on the idea that the antibacterial activity of ZnO is much related to reactive oxygen species (ROS), the ROS have been evaluated in terms of evaluation of luminol chemiluminescense (CL) emitted from the surface of ZnO in the dark. Thus prepared ZnO powders reveal strong antibacterial activity for *E. coli, pseudomonad aeruginosa, salmonella* bacteria and even an antibiotic-resistant MRSA (methicillin-resistant *Staphylococcus aureus*) under dark conditions at 25°C for 24 h (298 K for 86.4×10^3 s). The present paper treats their powder morphology, crystal structure and surface conditions in relation with the generation of ROS.

2.2 Experimental procedure

2.2.1 ZnO powder preparation

As shown in Fig. 2-1, fine ZnO powder (XZ-100F, Sakai Chemical Industry Co., Ltd., Sakai, Osaka, Japan) with a BET surface area S_A of 7.83 m^2/g, *i.e.*, particle size P_s of 0.137 μm, calculated from both S_A and theoretical density (D_x) of 5.606 Mg/m^3 (PDF #36-15451), was used as the starting material. Both this powder and a 100 mL $Zn(NO_3)_2$ aqueous solution with a concentration of 3 mol·L^{-1} prepared from regent grade $Zn(NO_3)_2$ were put into a 150 mL PTFE (polytetrafluoro- ethylene) vessel in a small hydrothermal equipment. They were heated at 150~170°C for 7 h (423~443 K for 25.2×10^3 s); these conditions were determined from our preliminary experiments.
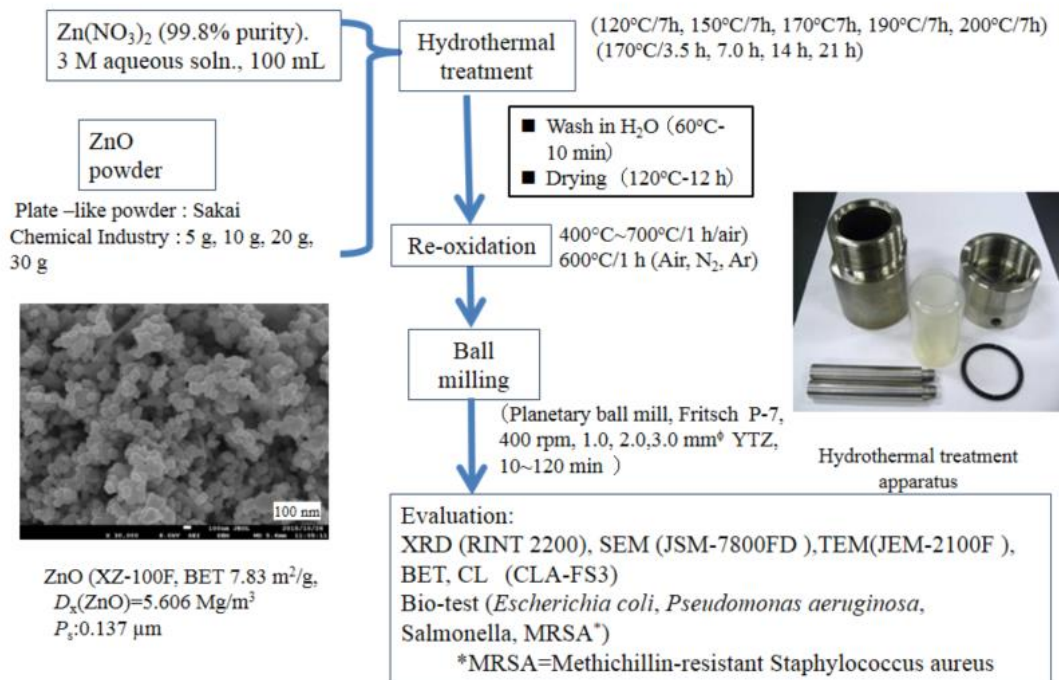
Fig. 2-1 Experimental procedure and evaluations of ZnO powders.

As will be described later, the powders after hydrothermal treatment (HT) were the mixtures of zinc nitrates, zinc oxide, and zinc hydroxides as shown in Table 2-1, differential thermal analysis and thermo gravimetry (DTA/TG), and X-ray diffraction (XRD) analysis of these compounds in air revealed that they decomposed into ZnO around 280°C (553 K), then, they were heat treated, *i.e*., re-oxidized into ZnO at 400~700°C for 1 h (673~973 K for 3.6×10^3 s) in air.

Table 2-1 Chemical products of the hydrothermally treated ZnO powders at 170°C for 7 h

in an aqueous 3 mol·L^{-1} (M) Zn(NO$_3$)$_2$ solution

Group of each ZnO filling rate	Chemical products	
Group 3 30～40 g-170°C/7h (0.368～0.491 *M*/100 mL)	Zn$_3$(NO$_3$)$_2$(OH)$_4$ Zn$_5$(OH)$_8$(NO$_3$)$_2$(H$_2$O)$_2$ ZnO	(3) (2) (1)
Group 2 20 g-170°C/7h (0.246 *M*/100 mL)	Zn(NO$_3$)$_2$(H$_2$O)$_2$ Zn$_3$(OH)$_4$(NO$_3$)$_2$ Zn$_5$(OH)$_8$(NO$_3$)$_2$(H$_2$O) ZnO	(5) (3) (2) (1)
Group 1 5～10 g-170°C/7h (0.064～0.123 *M*/100 mL)	Zn(NO$_3$)$_2$(H$_2$O)$_2$ Zn(OH)(NO$_3$) Zn$_3$(OH)$_4$(NO$_3$)$_2$ Zn$_5$(OH)$_8$(NO$_3$)$_2$(H$_2$O)$_2$ ZnO	(5) (4) (3) (2) (1)

Pulverizing of ZnO powders was performed using a planetary ball-milling apparatus (P-7, Fritsch Japan, Yokohama, Japan), zirconia 45 mL-container, and 0.3, 1.0, 2.0, 3.0 mm diameter yttria-stabilized tetragonal ZrO$_2$ (YTZ) balls of 50 g (5.0×10^{-2} kg) with a powder : ball=1:10 mass ratio in 10 mL (10×10^{-6} m^3) ethanol, at 6.67 rounds per sec (400 rpm, gravitational acceleration unit : 10.91 *g*) for 60 min (3.6×10^3 s). Furthermore, using 2.0 mm

diameter YTZ balls, pulverizing was conducted for 30~180 min (1.8×10^2 ~10.8×10^3 s) under the same conditions as above.

2.2.2 Evaluation

As shown in left side of Fig. 2-2, chemiluminescence (CL) of re-oxidized powders (100 μmol) in a 0.25 mL (2.5×10^{-7} m^3) aqueous luminol solution (5.0 μmol/L, 5.0×10^{-9} mol·m^{-3}) mixed with 3.0 mL (3.0×10^{-6} m^3) carbonic acid buffer solution (NaOH/NaHCO$_3$: pH=10.8) was observed in the dark condition using a CL detector (Tohoku Electronic Industrial Co., Ltd. CLD-100FC) [22]. After dropping the luminol solution in a 2 min's (1.2×10^2 s') warming up of the detector, the intensity of CL was integrated between 1.2-6.0×10^2 s, *i.e.*, (ΣCL) as shown in the right side of Fig. 2-2.

Reactive oxygen species generated at the surface of ZnO can bring antibacterial activity.

Measuring the integrated CL intensity of ZnO powders makes it possible to compare their antibacterial activity.

under dark

PMT

0.25 mL luminol solution

3.0 mL carbonic acid buffer solution (pH 10.8)

1.00 mL ZnO dispersion liquid

Stirrer

Integrated CL values = Σ CL =Σ *I* (*t*=120~600 s)

Fill ration of ZnO
—5 g
—10 g
—20 g
—30 g

CL intensity (count)

Measuring time (s)

Chemical luminescence (CL) curves of ZnO powders prepared by the hydrothermal treatment of 170ºC for 7 h in 3 M Zn(NO$_3$)$_2$ solution, followed by re-oxidation of 400ºC for 1 h in air.

Analytical conditions

CL reagent : 0.25 mL luminol solution

Migration buffer : 3.0 mL carbonic acid buffer solution (pH 10.8)

Oxidant : 1.00 mL ZnO dispersion liquid (0.10 M)

Fig. 2-2 CL (Chemiluminescence) measurement.

X-ray diffraction (XRD, Ultima III, Smartlab, Rigaku, Tokyo, Japan) analysis using CuKα radiation with a graphite monochromator was utilized for determination of the crystalline phases and estimation of "effective Debye parameter, B_{eff}" [23] of ZnO powders. The latter B_{eff} was calculated using the following equation as $\ln(I_{obs}/I_{calc}) = \ln k - 2 \cdot B_{eff} \cdot (\sin\theta/\lambda)^2$, here, ln is natural logalism, I_{obs} and I_{calc} are the XRD intensities from each (001), (100) and (101) lattice plane of the ZnO powders after and before ball-milling, respectively, k is constant, and θ and λ are angles of XRD peaks by the radian and the wave length of CuKα of 0.15418 nm, respectively. Microstructural observation with field emission-type scanning electron microscopes (FE-SEM, JSM-7001FD, JSM-7800, JEOL Ltd., Tokyo, Japan) was performed on the ZnO powders prepared under various conditions. BET surface areas of powders were measured using a particle characterization analyzer (Tristar II, Micromeritics Japan, Tokyo) at room temperature.

Both electron spin resonance (ESR, JES-X320, JEOL) using 5,5-dimethyl-1-pyrroline-N-oxide (DMPO) and dimethyl sulfoxide (DMSO) based on the spin- trapping method (ST-ESR) [24], and CL with scavengers [25] such as, 2-5 dimethyl furan (singlet oxygen, $^1O_2$), nitrobluetetrazolium (superoxide, $\cdot O_2^-$), 2-propanol (hydroxyl radical, $\cdot OH$), and riboflavin (hydrogen per oxide, H_2O_2) measurements were utilized at room temperature to identify the reactive oxygen species (ROS) of ZnO powders.

2.3 Results and discussion

Figure 2-3 shows the XRD patterns of products hydrothermally treated at 170°C for 7 h (443 K for 2.52×10^3 s) in a 100 mL of 3 mol·L^{-1} Zn(NO$_3$)$_2$ aqueous solution. These products were divided into 3 groups; Group 1 to Group 3 on the basis of the XRD patterns, *i.e.*, Group 1

includes the chemical products which prepared from 5 and 10 g (5 and 10×10^{-3} kg) starting ZnO powders, Group 2 is the products from 20 g (20×10^{-3} kg) ZnO powders, and Group 3 is the products prepared from 30 and 40 g (30 and 40×10^{-3} kg) ZnO powders. The chemical products in each group are summarized in Table 2-1. In Group 1 there are 5 kinds of zinc compounds. However, with increasing the amount of ZnO powder the number of zinc compounds decreased to 3. This might be explained by when the amount of ZnO is small, $Zn(NO_3)_2$ is enough to react with ZnO and produce a lot of basic zinc nitrate salts. However, with the increasing of ZnO, at first $Zn(OH)(NO_3)$ is disappeared in Group 2 and then $Zn(NO_3)_2(H_2O)_2$ is not formed in Group 3. As these zinc nitrate salts were decomposed into ZnO around 280°C (553 K) from our preliminary experimental results of DTA/TG analysis, all zinc compounds which formed after hydrothermal treatment process were heated between 400-700°C (673-973 K).
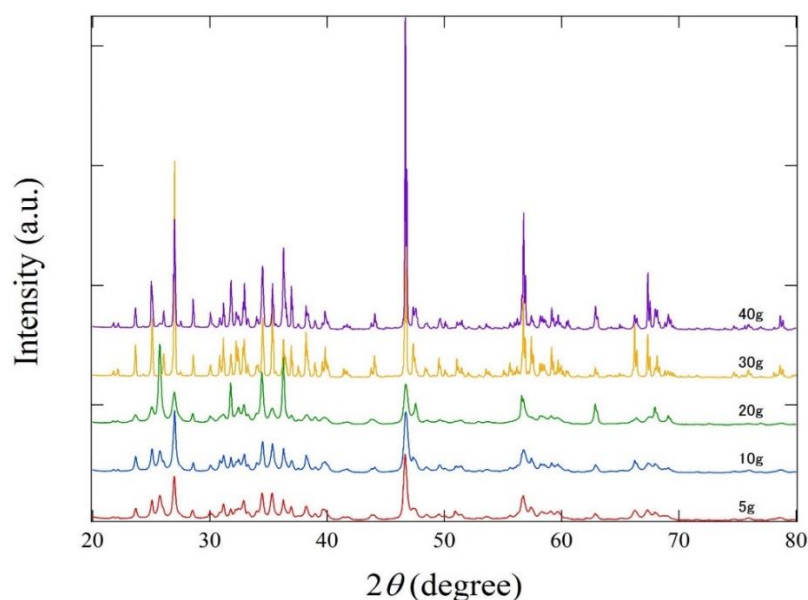
Fig. 2-3 XRD patterns of the products hydrothermal treated at 443 K for 2.52×10^3 s derived from ZnO powder as a function of powder filing rate.

Figure 2-4 displays the integrated intensity of chemicalluminesence, ΣCL, of ZnO powders heated at verious conditions, *i.e*., temperatures, atmospheres such as O_2, air, N_2 or Ar. Between 400-700°C (673-973 K), ZnO powders were heated in a little reductive atmosphere, especially, N_2/Ar at 600°C (873 K) gave the highest ΣCL value, 425×10^3 counts, suggesting that a reductive atmosphere introduces a small amount of oxygen vacancies V_O into ZnO lattice structure. However, the higher temperature heating which is more than 700°C (973 K) gave a drop of ΣCL. This can be explained in terms of the begining of sintering of ZnO powder around 700°C (973 K).
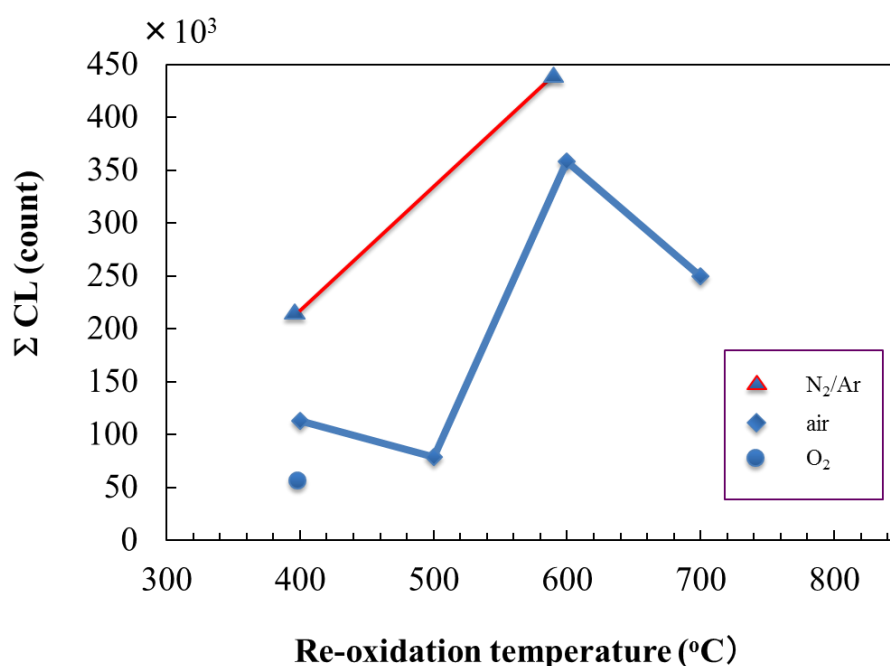
Fig. 2-4 ΣCL of ZnO powders heated at various re-oxidation temperatures after the hydrothermal treatment at 170°C for 3 h in 3 M $Zn(NO_3)_2$ aqueous solution.

SEM photographs of ZnO powders prepared at 400°C (673 K) and 600°C (873 K) for 1 h (3.6×10^3 s) in air after the hydrothermal treatment (HT) with various reaction time from 3.5

to 21 h (12.6 to 75.6×10^3 s) are shown in Fig. 2-5 (I) and (II), respectively. These microphotographs reveal the powder morphology; i) when compared with the starting ZnO powder (XZ-100F) which shown in Fig. 2-1, it is clear that ZnO particles have grown slightly from 0.137 μm (XZ-100F) to 0.1~0.2 μm (Fig. 2-5 [I]: 400°C/1h ($673K/3.6 \times 10^3$s) or 0.1~0.4 μm (Fig. 2-5 [II]: 600°C/1h: $873K/3.6 \times 10^3$s), ii) particle size has not been varied, despite the changes in both the soaking time of HT process and re-oxidation temperatura at 400°C (673 K) or 600°C (873 K). However, the powder morphology has changed from hexagonal plate-like to granular or quadrilateral particles.

(I)

(II)
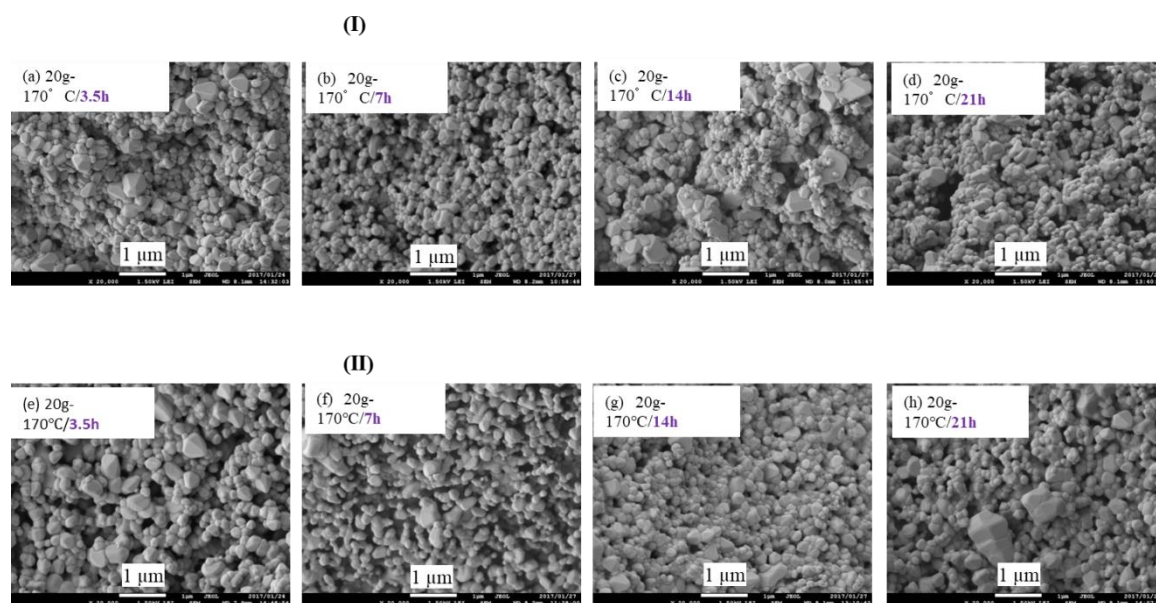
Fig. 2-5 SEM photographs of ZnO powders heated at (I) 673 K and (II) 873 K for 3.6×10^3 s in air after the hydrothermal treatment at 443 K for various soaking times in a 100 mL 3 M ($ZnNO_3$)$_2$ solution.

In order to increase ΣCL, *i.e.*, as will be described later, to improve the anctibacterial activity of ZnO powders, we considered to widen the surface areas of ZnO powder, based on

the idea that the disinfection might be occured at the surface, ZnO powder was milled with a planetary ball milling (BM) apparatus with a rotaing speed of 400 rpm (gravitational acceleration unit: 10.91 g) as mentioned before. Fig. 2-6 (i) shows the increment in BET surface area S_A as a function of milling time using 2.0 mm diameter YTZ balls (2.0 mm$^\phi$ YTZ). The values of S_A increased from 2.0 to 6.2 m^2/g up to 120 min (7.2×10^3 s) monotonously. However, more than 120 min of ball milling, the S_A value droped a little to 6.0 m^2/g. Then the morphology of ball-milled powders was observed by FE-SEM. Representative SEM photographs of ZnO powders with the BM time 0, 60, 120, 180 min (0, 3.6, 7.2, 10.8×10^3 s) are shown in Fig. 2-6 (II). At first glance, there is a little step from 0 to 60 min (3.6×10^3 s). However, no big difference in morphology among 60, 120 and 180 min (3.6, 7.2, and 10.8×10^3 s) BM powders from SEM observation was found.
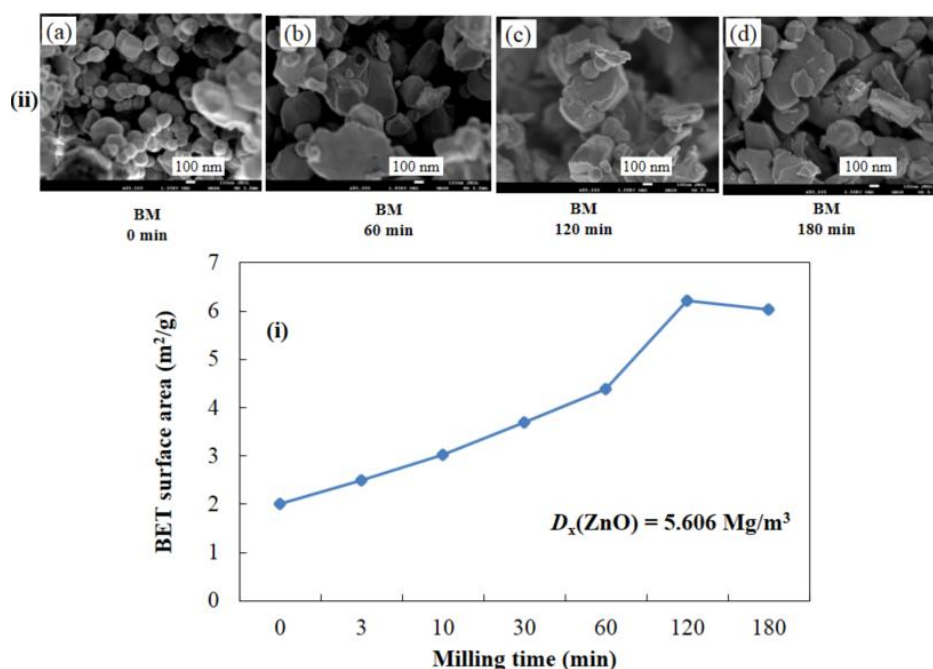
Fig. 2-6 BET surface area of ball-milled ZnO powders at various milling time.

BM time dependence of ΣCL has been drawn as log-log plots. Fig. 2-7 (i) displays ΣCL values in logalism as a function of BM time in logalism. It can be easily understood that after 10.0 min (6.0×10^2 s) BM, ΣCL value increased rapidly until 120 min (7.2×10^3 s) BM and dropped at 180 min (10.8×10^3 s). Then, to investigate the origin of ΣCL increment, the ΣCL per unit surface area (count/m^2) was calculated. If the ΣCL values depend only on the surface area, the value of ΣCL per unit area should be constant with the change of milling times. However, Fig. 2-7 (ii) data suggests that BM between 30-180 min (1.8-10.8×10^3 s) gives another effect in addition to the increase in surface area of ZnO powder.
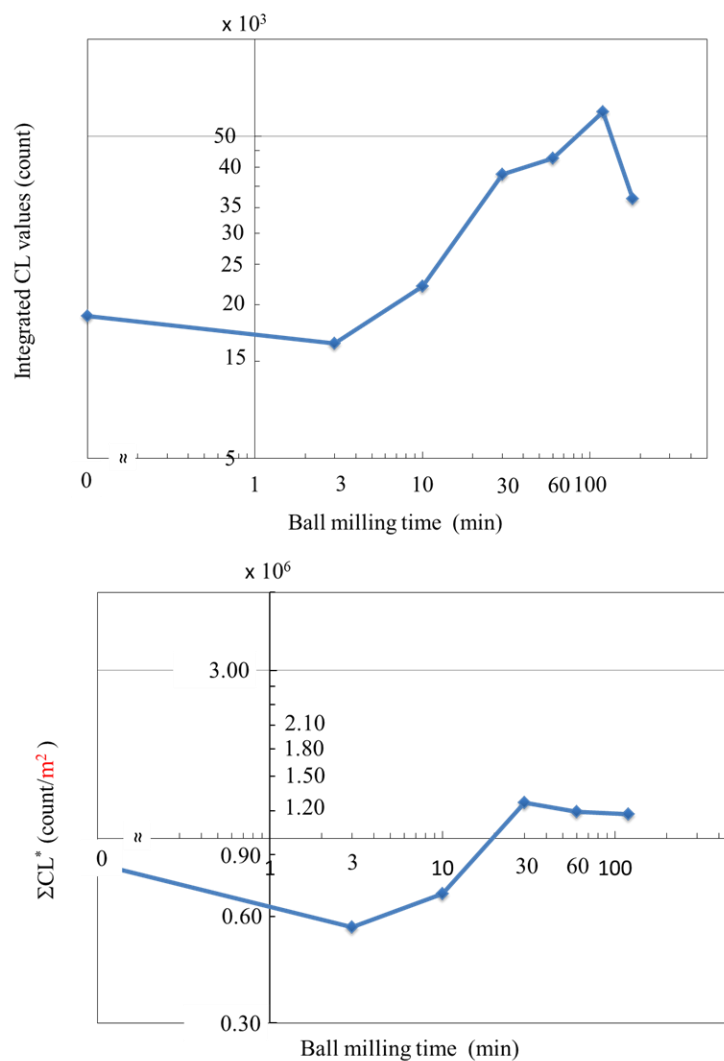
Fig. 2-7 ΣCL values (i) in logalism as a function of BM time and (ii) in logalism as a function of logalism of BM time.

Next, XRD patterns of ZnO powders before and after BM were investigated precisely. Fig. 2-8 (i) and (ii) show XRD patterns of ZnO powders before and after 60 min (3.6×10^3 s) BM, respectively. In general, XRD patterns of ball-milled powders tend to show the low diffraction peak intensity and at the same time the wider half width, those come from pulvelized fine particles. However, when XRD patterns in Fig. 2-8 (i) and (ii) are compared, only the low

36

diffraction peak intensities are recognized and the wider half width is not observed; this result indicates that only lattice strain (distortion) was introduced into ZnO powders by a planetary ball-milling using 2.0 mm$^\phi$ YTZ balls. This explanation consistents with as-mentioned SEM observation on BM powders in Fig. 2-6 (ii).
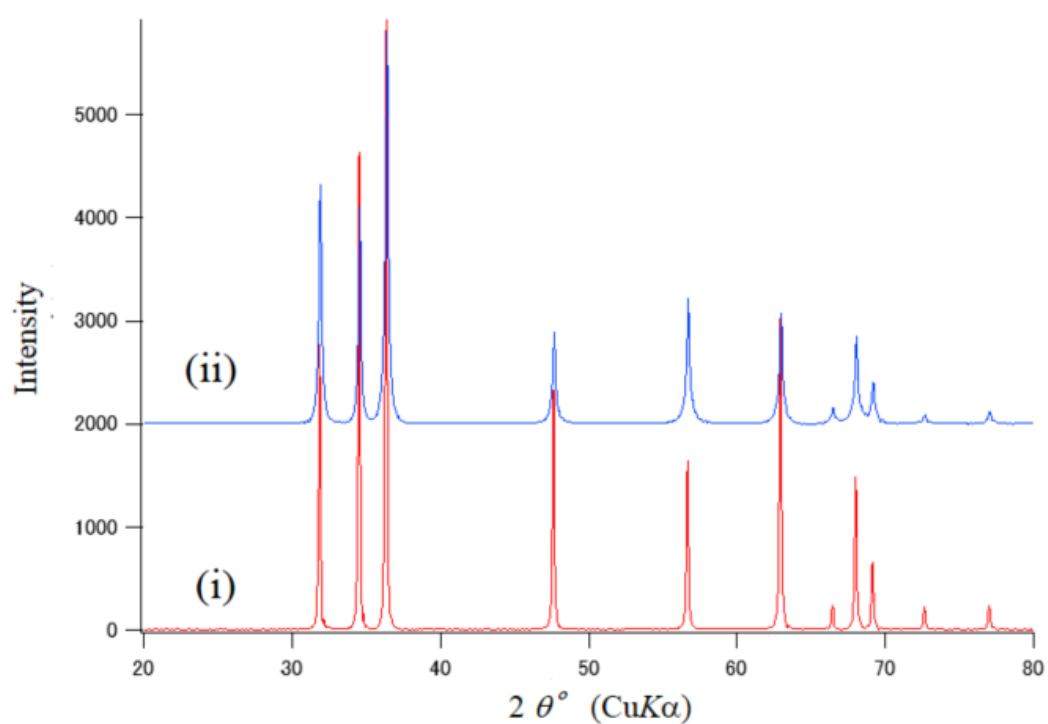
Fig. 2-8 XRD patterns of the samples (i) before and (ii) after ball milling for 3.6×10^3 s using YTZ balls with 2.0 mm in diameter.
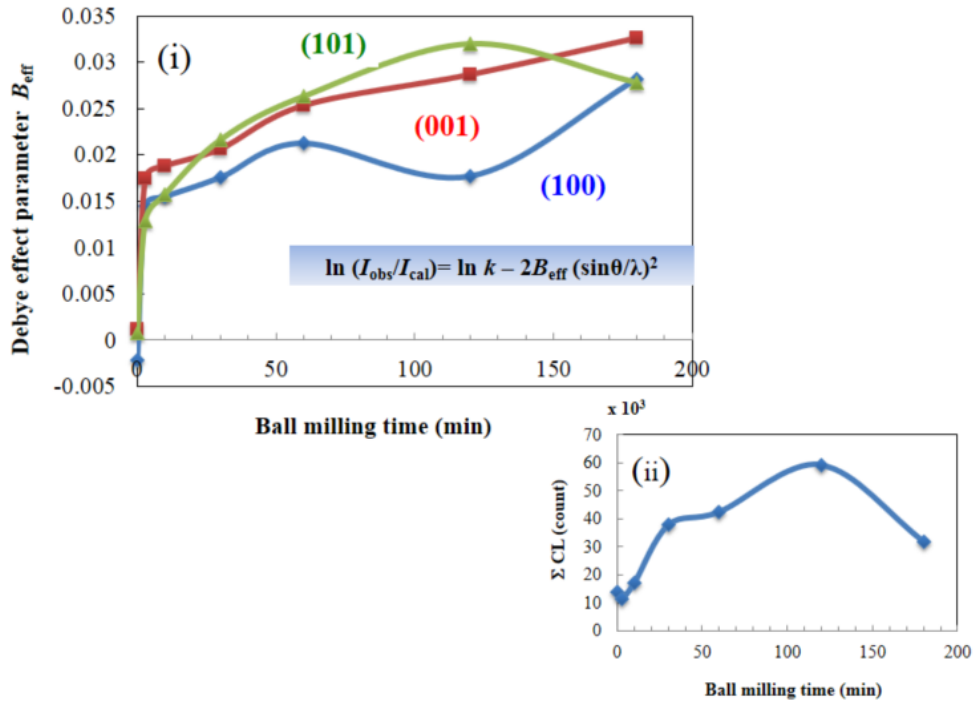
Fig. 2-9 (i) Relation of Debye parameter B_{eff} and ball milling time, and (ii) integrated CL values as a function of ball milling time.

In order to evaluate the structural strain (distortion), $i.e.$, effective Debye parameter B_{eff} was estimated for (001), (100) and (101) lattice planes of ZnO powder. Fig. 2-9 (i) indicates B_{eff} behaviors for each lattice plane as a function of ball-milling time using 2.0 mm$^{\phi}$ YTZ balls on the ZnO powder which was prepared by HT of 100mL 3 M $Zn(NO_3)_2$ aqueous solution at 170°C for 7 h (443 K for 25.2×10^3 s), followed by re-oxidation heat treatment of 600°C for 1 h (873 K for 3.6×10^3 s) in air; afterward these preparation conditions will be described as "standard method". Also in Fig. 2-9 (ii), ΣCL values of ZnO powder as a function of ball-milling time are displayed. Well agreement in the dependence of ΣCL values on ball-milling time with B_{eff} of (101) plane is recognized.

Fig. 2-10 (i) and (ii) show B_{eff} for each lattice plane and ΣCL values of the ZnO powder, respectively, as a function of YTZ ball size. The dependence of both B_{eff} for all planes and ΣCL on YTZ ball size are similar. From these, it might be clear that B_{eff} of (101) plane can reflect the dependence of ΣCL, *i.e.*, the lattice strain (distortion) at (101) plane has much effect on the ΣCL values. This can be explained as follows;

1. Ball milling (BM) introduced ZnO powder the structural strain (distortion) in addition to the pulverizing effect; the later resulted in the increase of BET surface area as mentioned in Fig. 2-6.

2. The former structural strain (distortion), *i.e.*, strain (distortion) can be evaluated in terms of B_{eff} for each plane.

3. The dependence of B_{eff} (101) on both BM time and ball size might suggest that (101) lattice plane could be easily distorted by BM process because the electron clouds of two oxygen O^{2-} ions with the fractional coordinates of (1/3, 2/3, 0.382) and (2/3, 1/3, 0.882) in ZnO crystal structure, spread over (101) plane partially. However, both (001) and (100) planes only contain one O^{2-}.

4. If it could be presumed that "z" coordinate of O^{2-} might be variable, distortion can be easily occured in (101) plane. On the other hand, one Zn^{2+} (1/3, 2/3, 1) occupies (001) plane and the electron cloud of Zn^{2+} (2/3, 1/3, 1/2) spreads over (101) plane. However, no Zn^{2+} occupies (001) plane.

5. Therfore, B_{eff} (101) can indicate the distrotion degree.

6. This distortion might enhance the possibility of the forming interstitial Zn atoms, which will be described later, will be able to happen between (101) planes of ZnO.

7. The interstitial Zn atoms, those become Zn^{2+} ions spontaneously, can produce reactive oxygen species (ROS), which brings the ball-milled ZnO powders high ΣCL values.
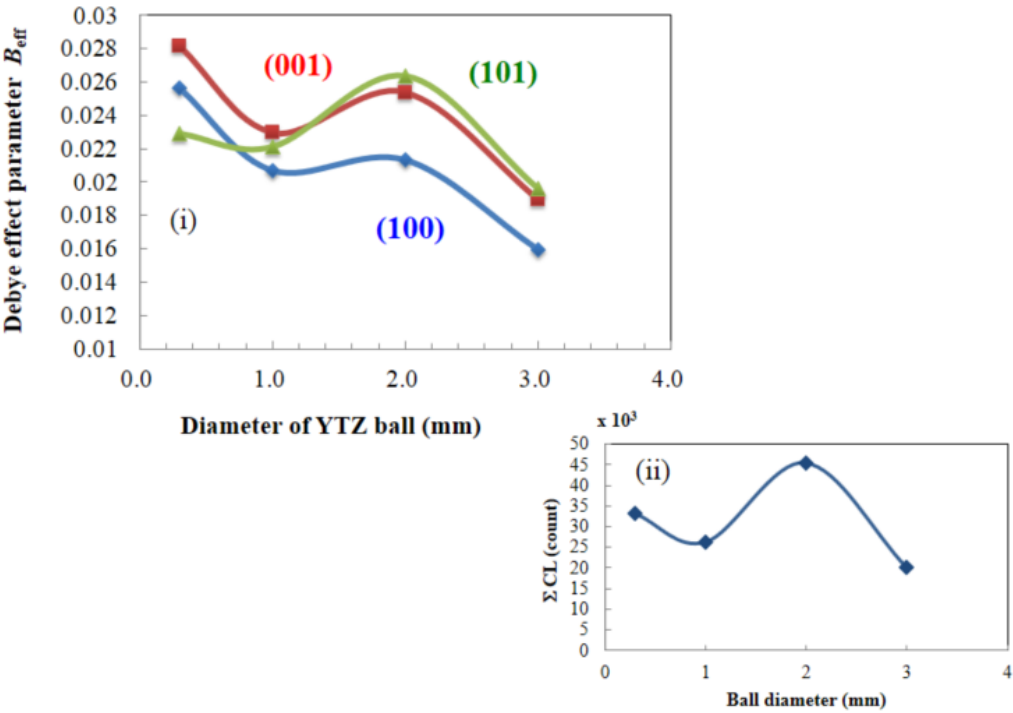
Fig. 2-10 (i) Relation of Debye parameter B_{eff} and diameter of YTZ ball, and (ii) integrated CL values as a function of diameter of YTZ ball.

To identify the ROS in thus prepared ZnO powders, electron spin resonance (ESR) using spin-trapping method (ST-ESR) [24] was applied. Fig. 2-11 reveals their results; by comparing the ESR patterns shown in (i) only DMPO added and (ii) DMPO + ZnO samples, DMPO-OH signals were observed in (ii), and when DMSO was added furthermore to (ii) as shown in (iii), DMPO-OH signals was disappeared. This suggests that ROS generated from the surface of ZnO

should be hydroxyl radical (·OH) as displayed in right side of Fig. 2-11. Another identification of ROS had been conducted.
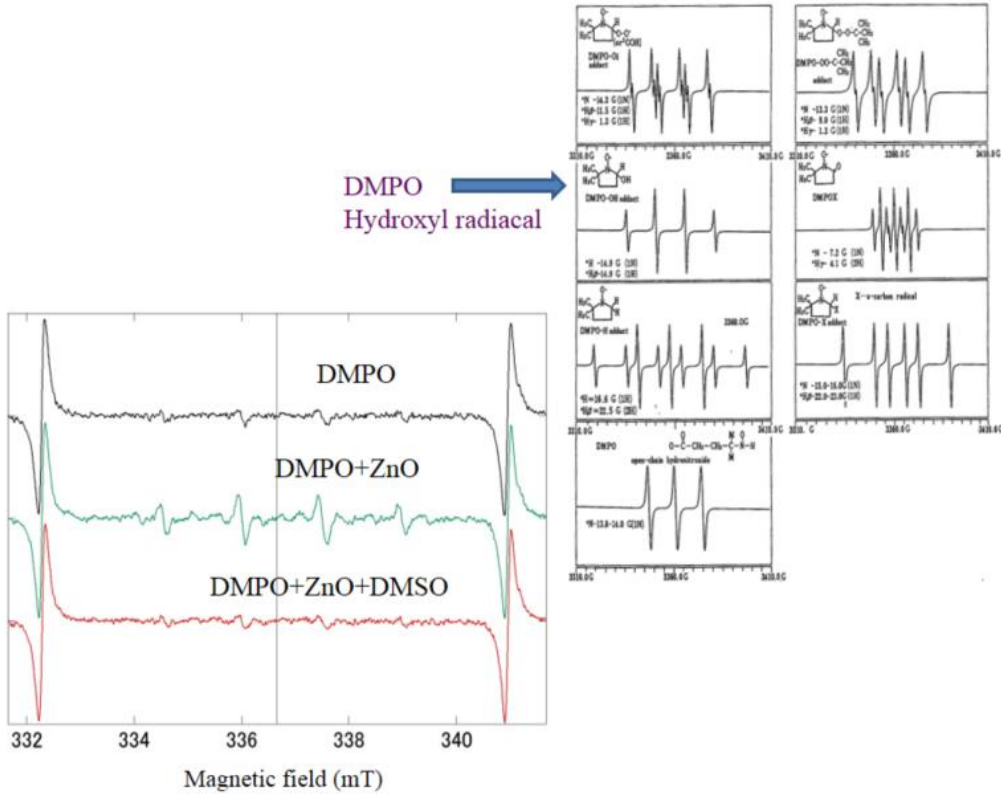
Fig. 2-11 ESR patterns of ZnO powder before and after inputting scavengers.

Fig. 2-12 shows the CL curves of ZnO powders with scavengers such as, (i) 2-5 dimethyl furan (singlet oxygen, $^{1}O_2$), (ii) nitrobluetetrazolium (super oxy anion radical, superoxide, $·O_2^-$), (iii) 2-propanol (hydroxyl radical, ·OH), and (iv) riboflavin (hydrogen per oxide, H_2O_2) [25].
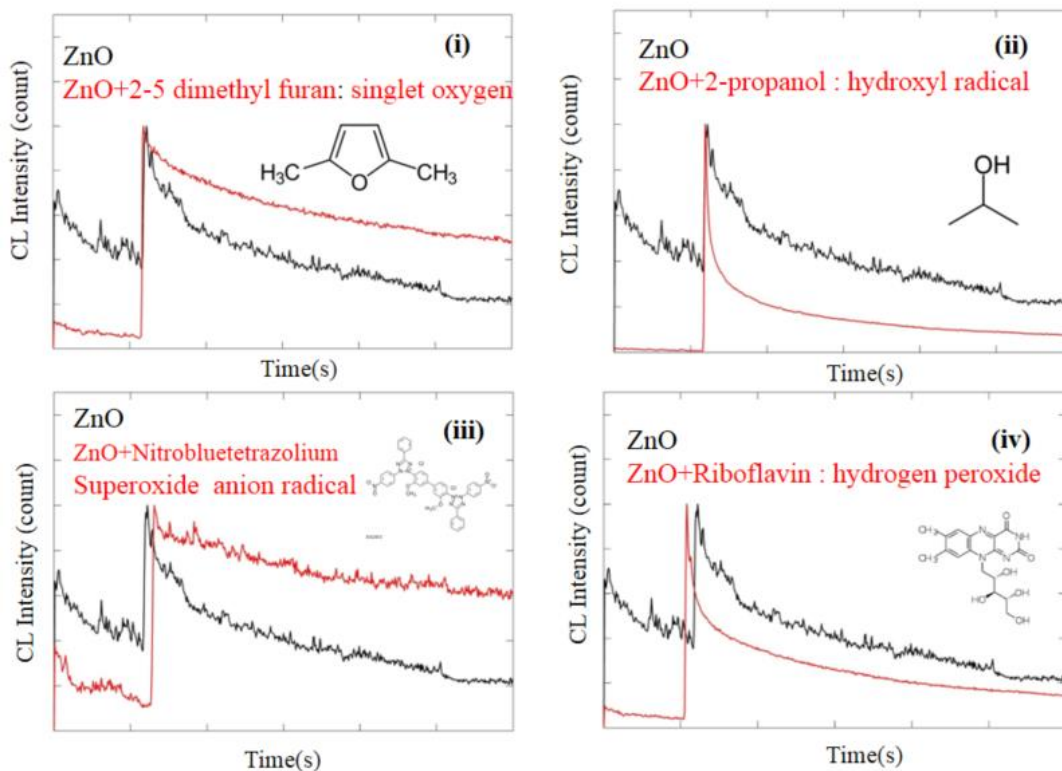
Fig. 2-12 CL curves of ZnO powder with and without various scavengers.

In Fig. 2-12, (a) black and (b) red curved lines represent CL data from ZnO and ZnO + scavengers, respectively. In Fig. 2-12 (i) and (ii), the CL values of each (b) red curved lines are higher than those of (a) black lines. However, on the contrary, the CL values of each (b) red lines are much lower than those of (a) black lines in (iii) and (iv). These suggest that scavengers of 2-propanol and riboflavin in (iii) and (iv), reacted with hydroxyl radical $\cdot$OH, and hydrogen per oxide H_2O_2, generated from the surface of ZnO, respectively. As hydroxyl radical $\cdot$OH easily transforms into H_2O_2 by following equation; $2\cdot OH \rightarrow H_2O_2$. Therefore, the result of (iv) is the same as (iii). Both ESR and CL data support the result of generation of hydroxyl radical $\cdot$OH from ZnO.

Here, antibacterial activity of thus prepared ZnO powders are considered. Fig. 2-13 displays the disinfect mechanism of the ZnO powders. As zinc oxide is a nonstoichiometric metal-rich compound $Zn_{1+\delta}O$, after the hydrothermal treatment at 170°C for 7 h (443 K for 25.2×10^3 s) in concentrated 3M $Zn(NO_3)_2$ aqueous solution, followed by re-oxidation heat treatment of 600°C for 1 h (873 K for 3.6×10^3 s) in air; the value of δ might be increased, *i.e.*, the interstitial Zn_i in ZnO also increased. As Zn_i are not stable, they at once decomposed into $Zn_i^{\cdot\cdot}$ + 2e⁻ at the ZnO surface. When water H_2O in air approaches to the surface of ZnO, H_2O will react with $Zn_i^{\cdot\cdot}$, then hydroxyl radical ·OH will be generated by the following equation;
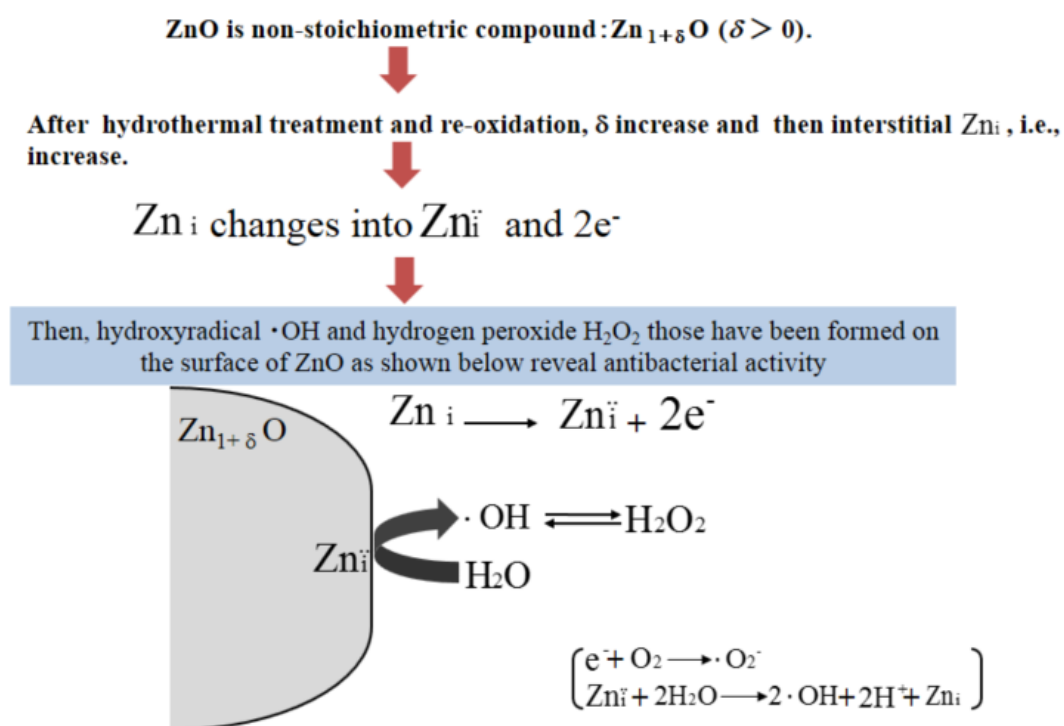
Fig. 2-13 Mechanism of antibacterial activity of hydrothermally and re-oxidized ZnO powder.

43

$$Zn_i^{\cdot\cdot} + 2\,H_2O \rightarrow 2\,\cdot OH + 2\,H^+ + Zn_i.$$
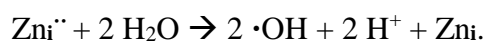
As mentioned before, thus prepared ZnO powders have been bio-tested based on the colony count method using various kinds of bacteria under the dark condition at 25°C for 24 h (298 K for 86.4×10^3 s). Table 2-2 summarizes the results; starting numbers of bacteria (N_o) were around $3\sim7\times10^5$, after the 24 h (86.4×10^3 s) culture microbe, the number of each bacteria (N_t) has been much reduced; the rate of sterilization, *i.e.*, $(N_t\text{-}N_o)/N_o\times100$, are 96.9~51.1%, 99.5~99.9%, 99.998~ 99.995%, and 100%, for *E. coli*, *pseudomonad aeruginosa*, *salmonella bacterium*, and MRSA, respectively, and for the comparison, the references without the addition of ZnO were conducted. As the rate of sterilization for *E. coli* was low, then its bio-testing had been performed at another condition of 36°C (309 K), the results are shown in the lower stand of Table 2-2; the rate of sterilization for *E. coli* reached 100%.

Table 2-2 Bio-tested based on the colony count method using various kinds of bacteria

（*Japan food research laboratory report No17003205001-010*）

	Reference	1) 170°C/7h+600°C/1h	2) 170°C/7h+600°C/1h (Ball milling 30 min)
Escherichia coil	4.9×10^5	1.5×10^3 (*96.9%)	2.4×10^4 (*51.1%)
Pseudomonad aeruginosa	7.0×10^5	3.5×10^3 (*99.5%)	40 (*99.9%)
Salmonella bacterium	3.9×10^5	10 (*99.998%)	20 (*99.995%)
MRSA	2.9×10^5	<10 (not detected）(*100%)	<10 (not detected) (*100%)

Testing conditions: 36°C under dark, phosphate buffered saline

As just described above, the present ZnO powders proved that they showed a strong antibacterial activity even in the dark conditions.

2.4 Conclusions

Being different from the antibacterial activity of TiO_2 under UV, ZnO powders prepared by hydrothermal treatment of 3 M $Zn(NO_3)_2$ at 170°C for 7 h (443 K for 25.2×10^3 s), followed by re-oxidation treatment at 600°C for 1 h (873 K for 3.6×10^3 s) in air reveal a strong disinfect even in the shade of sun. Ball-milling process has much improved this antimicrobial activity by increasing the surface area and introducing strain (distortion) of (101) lattice plane of ZnO. The present study proved the ZnO powders would be a high-power candidate for realizing the safe society far from catching disease, such as *pseudomonad aeruginosa, salmonella bacterium*, and MRSA. In future, these ZnO powders might have sterilization for influenza viruses and even bird flu virus.

References

1. R. Kumar, A. Umar, G. Kumar, H. S. Nalwa, Antimicrobial Properties of ZnO Nanomaterials: A Review, Ceramics International, 43(2017), 3940-3961.

2. A. Sirelkhatime, S. Mahmud, A. Seenim, N. H. M. Kaus, L. C. Ann, S. K. M. Bakhori, H. Hasan, D. Mohamada, Review on Zinc Oxide Nanoparticles: Antibacterial Activity and Toxicity Mechanism, Nano-Micro Lett., 7[3] (2015), 219-242.

3. M. Ramani, S. Ponnusamy, C. Muthamizhchelvan, J. Cullen, S. Krishnamurthy, E. Marsili, Morphology-directed synthesis of ZnO nanostructures and their antibacterial activity, Colloids Surf. B Biointerfaces, 105(2013), 24-30.

4. K. Elumalai, S. Velmurugan, S. Ravi, V. Kathiravan, S. Ashokkumar, Facile, Eco-friendly and template free phytosynthesis of Cauliflower like ZnO nanoparticles using leaf extract of Tamarindus indica (L.) and its biological evolution of antibacterial and antifungal activities, Spectrochim. Acta. A Mol. Biomol. Spectrosc., 136(2015), 1052-1057.

5. R. Wahab, Y. S. Kim, A. Mishra, S. Il Yun, H.S. Shin, Formation of ZnO Micro-Flowers Prepared via Solution Process and their Antibacterial Activity, Nanoscale Res. Lett., 5(2010), 1675-1681.

6. L. Palanikumar, S. N. Ramasamy, C. Balachandran, Size-dependent antimicrobial response of zinc oxide nanoparticles, IET Nanobiotechnol., 8(2014), 111-117.

7. Z. Huang, X. Zheng, D. Yan, G. Yin, X. Liao, Y. Kang, Y. Yao, D. Huang, B. Hao, Toxicological effect of ZnO nanoparticles based on bacteria, Langmuir, 24(2008), 4140-4144.

8. M.G. Nair, M. Nirmala, K. Rekha, A. Anukaliani, Structural, optical, photo catalytic and antibacterial activity of ZnO and Co doped ZnO nanoparticles, Mater. Lett., 65(2011), 1797-1800.

9. S. Siddique, Z. H. Shah, S. Shahid, F. Yasmin, Preparation, characterization and antibacterial activity of ZnO nanoparticles on broad spectrum of microorganisms, Acta Chim. Slov., 60(2013), 660-665.

10. R. K. Dutta, B. P. Nenavathu, M. K. Gangishetty, Correlation between defects in capped ZnO nanoparticles and their antibacterial activity, J. Photochem. Photobiol. B Biol., 126(2013), 105-111.

11. M. Premanathan, K. Karthikeyan, K. Jeyasubramanian, G. Manivannan, Selective toxicity of ZnO nanoparticles toward Gram-positive bacteria and cancer cells by apoptosis through lipid peroxidation, Nanomed. Nanotechnol. Biol. Med., 7(2011), 184-192.

12. S. Nair, A. Sasidharan, V. V. Divya Rani, D. Menon, S. Nair, K. Manzoor, S. Raina, Role of size scale of ZnO nanoparticles and microparticles on toxicity toward bacteria and osteoblast cancer cells, J. Mater. Sci. Mater. Med., (2009), S235-S241.

13. S. Dwivedi, R. Wahab, F. Khan, Y.K. Mishra, J. Musarrat, A. A. Al-Khedhairy, Reactive oxygen species mediated bacterial biofilm inhibition via zinc oxide nanoparticles and their statistical determination, PLoS One, 9(2014), e111289.

14. A. Jain, R. Bhargava, P. Poddar, Probing interaction of Gram-positive and Gram-negative bacterial cells with ZnO nanorods, Mater. Sci. Eng. C., 33(2013), 1247-1253.

15. N. Talebian, S. M. Amininezhad, M. Doudi, Controllable synthesis of ZnO nanoparticles and their morphology-dependent antibacterial and optical properties, J. Photochem. Photobiol. B Biol., 120(2013), 66-73.

16. A. Stankovic, S. Dimitrijevic, D. Uskokovic, Influence of size scale and morphology on antibacterial properties of ZnO powders hydrothemally synthesized using different surface stabilizing agents, Colloids Surf. B Biointerfaces, 102(2013), 21-28.

17. N. A. Aal, F. Al-Hazmi, A. A. Al-Ghamdi, A. A. Al-Ghamdi, F. El-Tantawy, F. Yakuphanoglu, Novel rapid synthesis of zinc oxide nanotubes via hydrothermal technique and antibacterial properties, Spectrochim. Acta: A Mol. Biomol. Spectrosc., 135(2015), 871-877.

18. V. V. Shinde, D. S. Dalavi, S. S. Mali, C. K. Hong, J. H. Kim, P. S. Patil, Green synthesis of ZnO nanoparticles by Aspalathus linearis: Structural & optical properties, Appl. Surf. Sci., 307(2014), 495-502.

19. K. R. Raghupathi, R. T. Koodali, A. C. Manna, Size-Dependent Bacterial Growth Inhibition and Mechanism of Antibacterial Activity of Zinc Oxide Nanoparticles, Langmuir, 27(2011), 4020-4028.

20. P. Carvalho, P. Sampaio, S. Azevedo, C. Vaz, J. P. Espinós, V. Teixeira, J. O. Carneiro, Influence of thickness and coatings morphology in the antimicrobial performance of zinc oxide coatings, Appl. Surf. Sci., 307(2014), 548-557.

21. K. Hirota, M. Sugimoto, M. Kato, K. Tsukagoshi, T. Tanigawa, H. Sugimoto, Preparation of zinc oxide ceramics with a sustainable antibacterial activity under dark conditions, Ceramics International, 36(2010), 497-506.

22. S. Matsuoka, M. Kato, K. Hirota, K. Tsukagoshi: J. Powder Powder Metall., 57 [2] (2010), 106-111. (in Japanese)

23. M. Inagaki, H. Furuhara, T. Ozeki, S. Naka: J. Mater. Sci., 8(1973), 312-316.

24. M. Kohno, Applications of Electron Spin Resonance Spectrometry for Reactive Oxygen Species and Reactive Nitrogen Species Research, J. Clin. Biochem. Nutr., 47[1] (2010), 1-11.

25. C. Lu, G. Song, J.-M. Lin, Reactive oxygen species and their chemiluminescence-detection methods, Trend in Analytical Chem., 25[10](2006), 985-995.

CHAPTER 3

Dependence of Antibacterial Activity of ZnO Powders on Their Physicochemical Properties

3.1 Introduction

In the present age of advanced technologies, scientist and engineers are still making vast research about recurrence of infectious disease and bacterial contamination in all kinds of materials [1]. Nowadays, a number of inorganic anti-bacterial agents have been attracting much attention from food- and medical-related manufacturers due to their high credibility in comparison with organic anti-bacterial agents. Currently, new nanostructured materials with bactericidal properties are being used for preventing microbial growth because of the physicochemical properties, such as size, structure and surface of materials can enhance the antimicrobial activity [2].

Metallic oxide powders, such as TiO_2, especially anatase-type of TiO_2 [3, 4], and MO [1 ,5], MO$_2$ [1, 4] (here, M: metal element) have been found to inhibit bacterial growth. On the other hand, zinc oxide ZnO has been reported by the present authors [6-8] to reveal sustainable antibacterial activity even under dark conditions by submitting reactive oxygen species (ROS). The generation of ROS such as hydrogen peroxide (H_2O_2), hydroxyl radicals ($^{.}OH$) and superoxide (O_2^-) from the surface of ZnO is the main origin of its sterilizing property; and their generation mechanism in the dark has been proposed [6, 7, 9]. Furthermore, the germ's damage

caused by bactericidal inorganic substance such as MgO, CaO and ZnO, also has been explained by the changes in sensitivities of root cells [8].

For the better use of ZnO and in order to assist the expansion of powerful but non-toxic antimicrobial derivatives, there is much need for understanding the action process of ZnO nanoparticles against bacteria.

In the recent findings, the essential process of the antibacterial effect is not coherent [10, 11]. However, a few studies have shown that the basic cause of the antibacterial function might be originated from the disruption of cell membrane activity [12, 13]. Another possibility could be the orientation of intercellular ROS, including hydrogen peroxide (H_2O_2) which is a strong oxidizing agent harmful to bacterial cells [6, 13]. It has also been stated that ZnO can be initiated by UV and visible light to generate vastly ROS such as $\cdot OH$, H_2O_2, and $\cdot O_2^-$ [13,14]. The negatively charged $\cdot OH$ and $\cdot O_2^-$ cannot penetrate into bacterial cells [15].

The purpose of this study is to find the relationship between the physicochemical properties and the antimicrobial activity of 4 kinds of ZnO powders described as follows; No.1 the antibacterial ZnO which the authors have developed and reveals sustainable microbial activity in the dark [6]; No. 2 a commercially available ZnO powder (company product's name of "XZ-100F") which is the starting material for No.1; No. 3 very fine ZnO powder ("FINEX-30") and No. 4 the conventional fine ZnO powder. These powders were prepared in much different methods and conditions. The synthesis ways might strongly affect on their physico-chemical properties. In the present study, we have concentrated on both identifications of ROS submitted from the surface of each powder and what kind of ROS has strong influence on the disinfect activity of ZnO powders. From this study the antimicrobial activities of ZnO might be

improved furthermore by understanding the nature of inhibitory and lethal effect of ZnO nanoparticles on bacteria.

3.2 Experimental procedure

3.2.1 ZnO powder preparation

In this study, 4 kinds of ZnO powders were used as listed in Table 3-1.

No.1 sample is "antibacterial ZnO" powder, which was prepared by hydrothermal treatment in $Zn(NO_3)_2$ $3M$ aqueous solution at 443 K for 2.52×10^4 s and then re-oxidized at 773 K for 3.6×10^3 s in air and ball-milling [7, 16], using commercially available fine ZnO ("XZ-100F", Sakai Chemical Industry Co., Ltd, Sakai, Osaka, Japan) with BET surface area S_A of 7.83 $m^2 \cdot g^{-1}$, particle size P_s of 0.137 μm determined using S_A and its theoretical density D_x of 5.61 $Mg.m^{-3}$, as the same manner as our previous paper [7]. No. 2 sample is "XZ-100F" ZnO powder, which is a starting material used for No. 1 mentioned above. This sample was prepared from zinc acetate. No. 3 commercially available "FINEX-30" ZnO, (Sakai Chemical Industry Co., Ltd.) was synthesized by heating zinc carbonate at high temperature (673-1073 K) which is known as mechanochemical process [17]. No. 4 sample is also conventional fine ZnO powder, which prepared by melting metallic zinc as "French method" [17] at 1173 K, then cooling down to form zinc oxide as solid powder. All three ZnO No. 2-4 are commercial products.

Table 3-1 Preparation conditions for 4 kinds of ZnO powders

Sample	Precursors	Preparation method	Synthesis conditions	Properties
No 1 Antibacterial ZnO	XZ-100F ZnO 3M $Zn(NO_3)_2$ aq.	Hydrothermal treatment Ball milling	-Reaction temp.: 443 K, 2.52×10^4 s -Drying: overnight 353K -Calcinaion 773 K, 3.6×10^3 s in air -Ball-milling: 2mm$^\phi$YTZ, 3.6×10^3 s	Hexagonal Wurtzite structure 2.69 m^2/g
No 2 XZ-100F	$Zn(CH_3COO)_2$	--	--	Wurtzite 7.83 m^2/g
No 3 FINEX-30	$ZnCO_3$	Mechanochemical process	Calcination temp.: 673-1073 K	Wurtzite 27.4 m^2/g
No 4 Conventional Fine ZnO	Metallic Zinc	French method (indirect process)	Melting temp.: 1173 K Cooling ZnO particles	Wurtzite 9.06 m^2/g

3.2.2 Evaluation

X-ray diffraction (XRD, Ultima III, Smartlab, Rigaku, Tokyo, Japan) analysis using Cu$K\alpha$ radiation (wavelength of 0.15418 nm) with a graphite monochromator was utilized for determination of the crystalline phases and lattice parameters. Microstructural observation with field emission-type scanning electron microscopes (FE-SEM, JSM-7001FD, JSM-7800, JEOL Ltd., Tokyo, Japan) was performed on the ZnO powders prepared under various conditions.

BET surface areas S_A of powders were measured using a particle characterization analyzer (Tristar II, Micromeritics Japan, Tokyo) at room temperature.

Chemiluminescence (CL) [6,7,16] of ZnO powders (100 μmol) in a 0.25 mL (2.5×10^{-7} m^3) aqueous luminol solution (5.0 μmol/L, 5.0×10^{-9} mol·m^{-3}) mixed with 3.0 mL (3.0×10^{-6} m^3) carbonic acid buffer solution (NaOH/NaHCO$_3$, pH=10.8) was observed in the dark condition using a CL detector (CLD-100FC, Tohoku Electronic Industrial Co., Ltd., Sendai, Japan) [6]. After dropping the luminol solution in a 1.2×10^2 s' warming up of the detector, the intensity of CL was integrated between $1.2 \sim 6.0 \times 10^2$ s.

In the order to determine interstitial Zn contained in crystalline structure of ZnO, *i.e.*, Zn$_{1+\delta}$O, the following procedure was performed. (I) The weight of ZnO powder M_{ZnO} after heating at 573 K for 6.0×10^2 s in air was measured using a precision electric balance (here, this temperature and time was determined in terms of complete elimination of water adsorbed on the surface of ZnO using the DTA/TG). (II) The mass of oxygen content M_O of the same ZnO powder sample was measured using an Oxygen-Nitrogen Analyzer ("EMGA620W", Horiba Scientific, Kyoto, Japan) 5 times. The average value of M_O was determined. (III) From this M_O value, the oxygen mole n_O was calculated. Then the mol of Zn, n_{Zn}, in the same sample was estimated from the following equation: $n_{Zn} = [M_{ZnO} - 16.00 \times n_O] / 65.41$; here, 16.00 and 65.41 are atomic weights of oxygen and zinc, respectively. The content of interstitial Zn, δ, was determined by an equation of $n_{Zn} / n_O = 1 + \delta$.

As photoluminescence (PL) analysis is ideally suited for compositional analysis of defect evaluation of light-emitting materials [18]. PL measurement (Fluorolog®-3, 450 W Xe short arc lamp, Xe flush lamp with double monochromator, HORIBA, Kyoto, Japan) was

applied to identify interstitial zinc in the crystalline structure of ZnO powders at room temperature. X-ray Photoelectron Spectroscopy XPS or Electron Spectroscopy for Chemical Analysis, ESCA) analysis (ESCA3057, ULVAC-PHI. Inc., Chigasaki, Kanagawa, Japan) was utilized to analyze the surface chemical state of 4 kinds ZnO. A monochromated Al$K\alpha$ X-ray source (1486.6 eV) was used and operated at 150 W in a pressure of 1.333×10^{-12} Pa. All the binding energies were referenced to the Au$_{4f7/2}$ peak located at 84.2 eV attributed to the surface sputtered-Au.

Chemiluminescence (CL) with scavengers such as, 2-5 dimethyl furan (singlet oxygen, $^1O_2$, Wako Ltd., Tokyo, Japan), nitro blue tetrazolium (superoxide, $\cdot O_2^-$, Nacalai tesque, INC., Kyoto, Japan), 2-propanol (hydroxyl radical, $\cdot OH$, Nacalai tesque, INC., Kyoto, Japan), and riboflavin (hydrogen per oxide, H_2O_2, Wako Ltd.) measurements were utilized at room temperature in the dark to identify the reactive oxygen species (ROS) of ZnO powders [6]. Antibacterial test for various kinds of ZnO powders was evaluated with a colony count method using *E*. coli bacteria on nutrient agar medium in a Na-P buffer solution. The penetrated culture of bacteria was kept at 309 K for 8.64×10^4 s in a laboratory incubator. ZnO powders were added to a small amount of bacteria and mixed with 10 mL Na-P buffer solution in the sunshade.

3.3 Results and discussion

3.3.1 Characteristics of ZnO powders

Figure 3-1 shows XRD patterns of 4 kinds of ZnO powders; all samples have hexagonal Würzite structure. There is no significant difference in their lattice parameters among them as shown in Table 3-2. As No.1 powder was prepared from No. 2 ZnO by hydrothermal treatment, the lattice parameters of No.1 are a little larger than those of No. 2. However, *a* and *c* of No. 2

ZnO are a little smaller than the rest, its unit volume is the smallest among them. Crystallite size of No. 3 is the smallest due to its preparation method in which zinc carbonate was calcined at high temperatures, suggesting the finest powder among them.
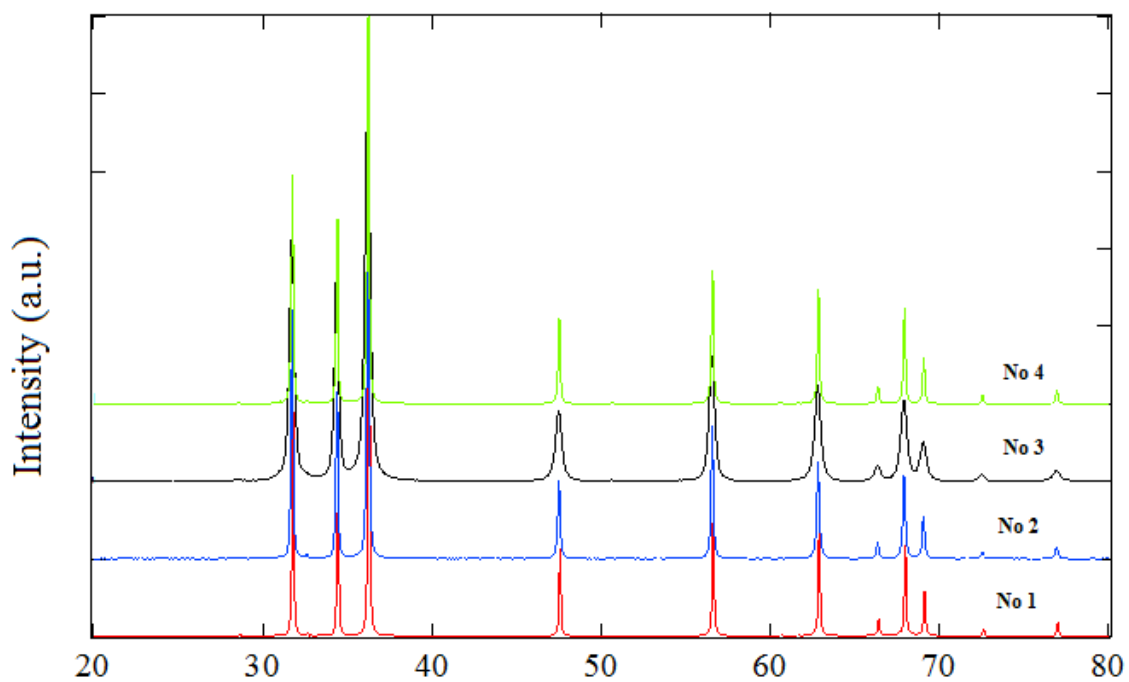
Fig. 3-1 XRD patterns of 4 kinds of ZnO.

Table 3-2 Lattice parameters and crystallite size X_s of ZnO powders

Sample	Lattice parameters			d(100) (nm)	d(001) (nm)	d(101) (nm)	Crystallite size (nm)
	a (nm)	c (nm)	v (nm^3)				
No 1	0.32490	0.52055	0.04869	0.009606	0.011853	0.007344	60.8
No 2	0.32468	0.52024	0.04860	0.0144575	0.0165865	0.013617	43.3
No 3	0.32484	0.52069	0.04868	0.01929	0.023483	0.020675	23.1
No 4	0.32489	0.52052	0.04868	0.00973	0.011161	0.00759	45

SEM photographs shown in Fig. 3-2 display the morphology and particle sizes of ZnO powders. The shapes of ZnO particles are sphere and some of them are hexagonal column. Besides, the particle size, P_s, of 4 samples that evaluated based on BET surface area values as indicated below the photographs are consistent with the SEM observation, predicting that the differences in their morphologies and particle sizes might affect to their antibacterial properties.
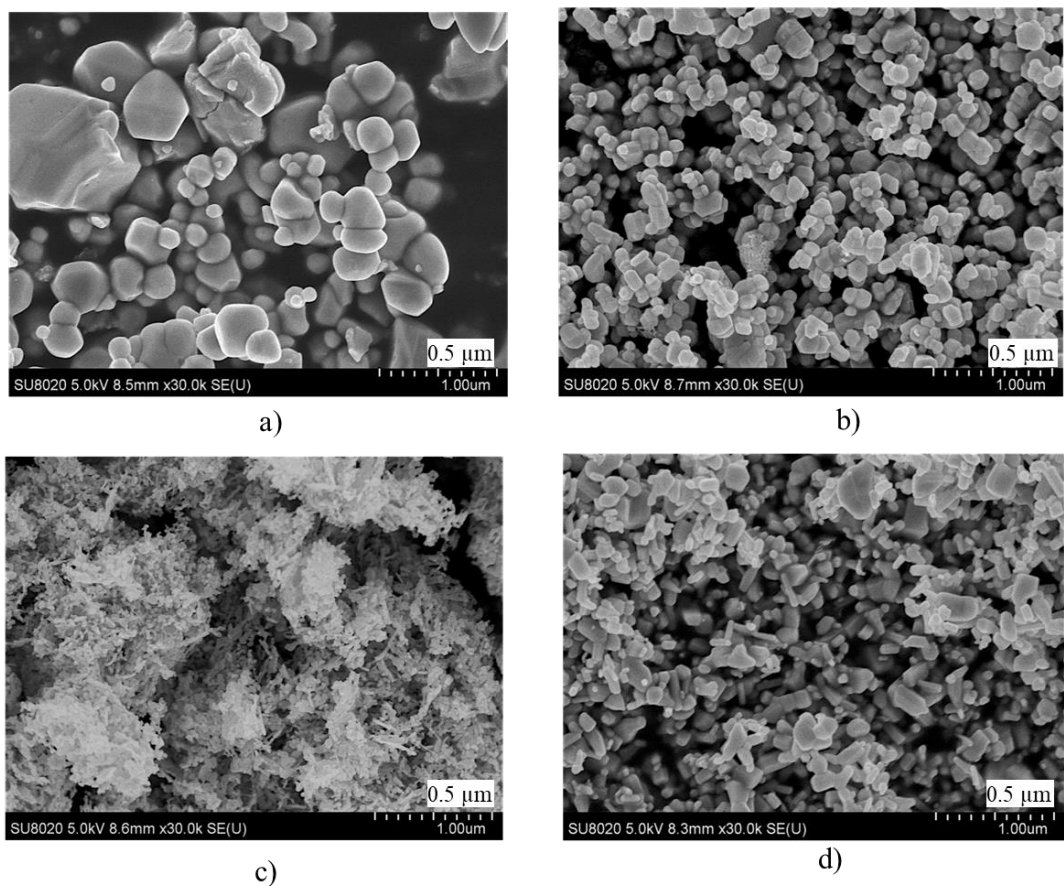
Fig. 3-2 SEM images of 4 kinds of ZnO powders: a) No. 1 antibacterial ZnO,

P_s=0.398μm; b) No. 2 XZ-100F ZnO, P_s=0.149 μm; c) No. 3 FineX-30, P_s=0.039 μm; d) No.

4 Conventional ZnO powder, P_s=0.118 μm.

Figure 3-3 shows the integrated chemiluminescence intensity, ΣCL, accumulated for

4.8×10^2 s under dark conditions as the blue bar graphs. Obviously, the CL value of No. 3

FINEX 30 fine powder is much higher than the other ZnO powders. With CL results, No. 3

ZnO powder is expected to reveal strong activity on bacteria. As it is clear that the surface area

has much effect on the value of ΣCL, the ΣCL values per unit area, ΣCL/S_A, were calculated

and shown in red bar graphs in Fig. 3-3. By comparing these $\Sigma CL/S_A$ values, there is little difference from No. 2 to No. 4; dare to say, No. 1 reveals a little smaller value.
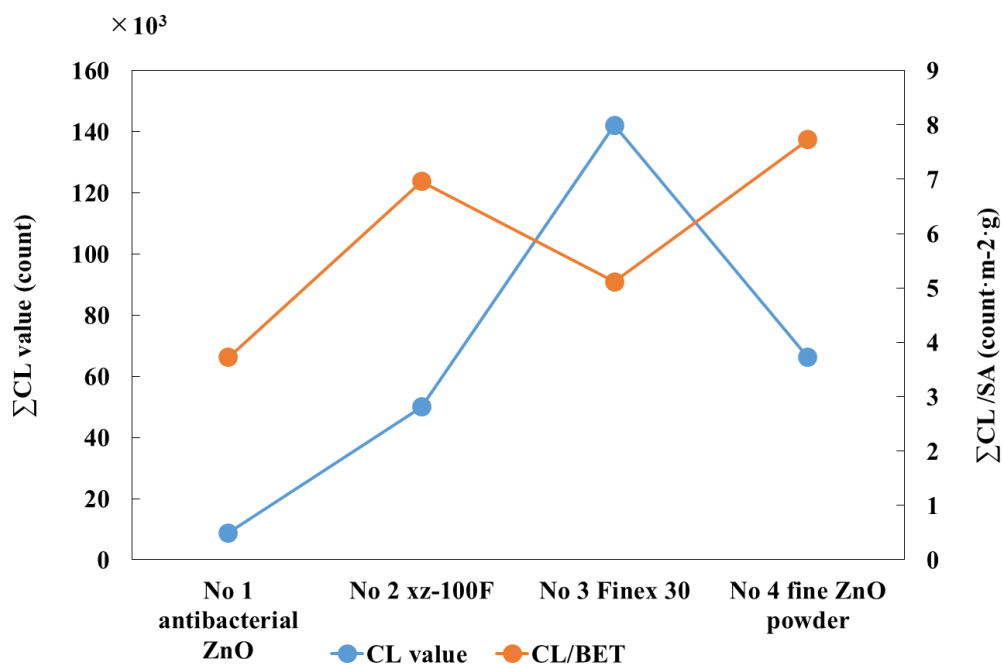
Fig. 3-3 CL and CL/S_A [S_A: BET surface area (m^2/g)] of 4 kinds of ZnO powders.

Zinc oxide is non-stoichiometric chemical compound with the chemical formula $Zn_{1+\delta}O$. After various treatments, for example, hydrothermal treatment and following re-oxidation, interstitial zinc ions in the ZnO lattice can be formed. These zinc interstitials are the main source of generation of ROS [19]. Fig. 3-4 displays the values in the formula $Zn_{1+\delta}O$ of 4 kind ZnO powders. These values were determined from the oxygen content of ZnO powders as explained above in the experimental procedure. As δ value reflects the amount of interstitial zinc, this value also affects to the amount of ROS that could be generated from the surface of ZnO powder

[6, 7]. No 1 sample gave the highest δ, on the contrary, No. 3 gave the lowest δ, even though high CL. From here, it is expected to submit high amount of ROS from the surface of No. 1 ZnO and resulted in the sustainable microbial activity under dark conditions [6].
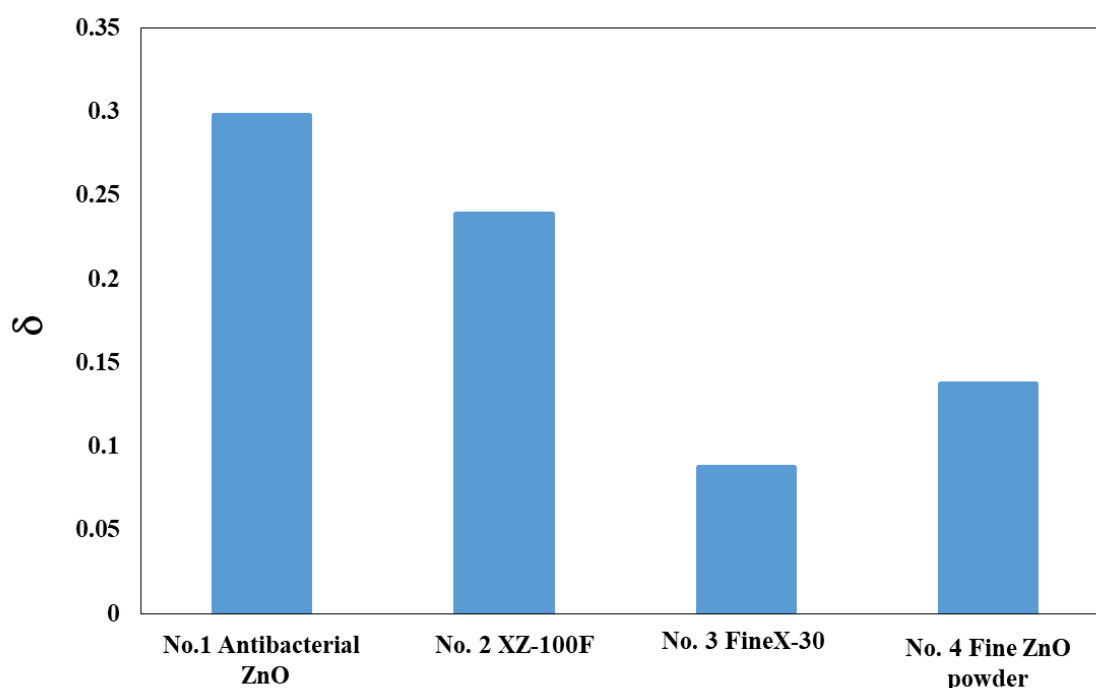
Fig. 3-4 δ values for interstitial Zn_i in ZnO powders.

Figure 3-5 shows the photoluminescence spectra (PL) of 4 samples. As all the measured data on Fluorolog3 equipped with a xenon lamp were re-calculated for optical filter transparency correction, some data have obvious intensity gap between the shorter wavelength range and longer wavelength range. These emission spectra that include the intensity gap should not be connected enforcedly using artificial normalization in order to avoid forgery, because these gaps originate from the photo-breaching, which is one of well-known fluorescence feature [20]. Basing on some previous studies [16], the peak around 600 nm wavelength corresponds to interstitial zinc and the intensity of PL peak is related to the amount of interstitial zinc. From

these spectra, it is easy to notice that the peak at 625 nm of No. 1 sample shows the highest intensity. Therefore, the PL data also support that this sample includes the high amount of interstitial zinc, consisting with high δ value of No. 1 ZnO sample.
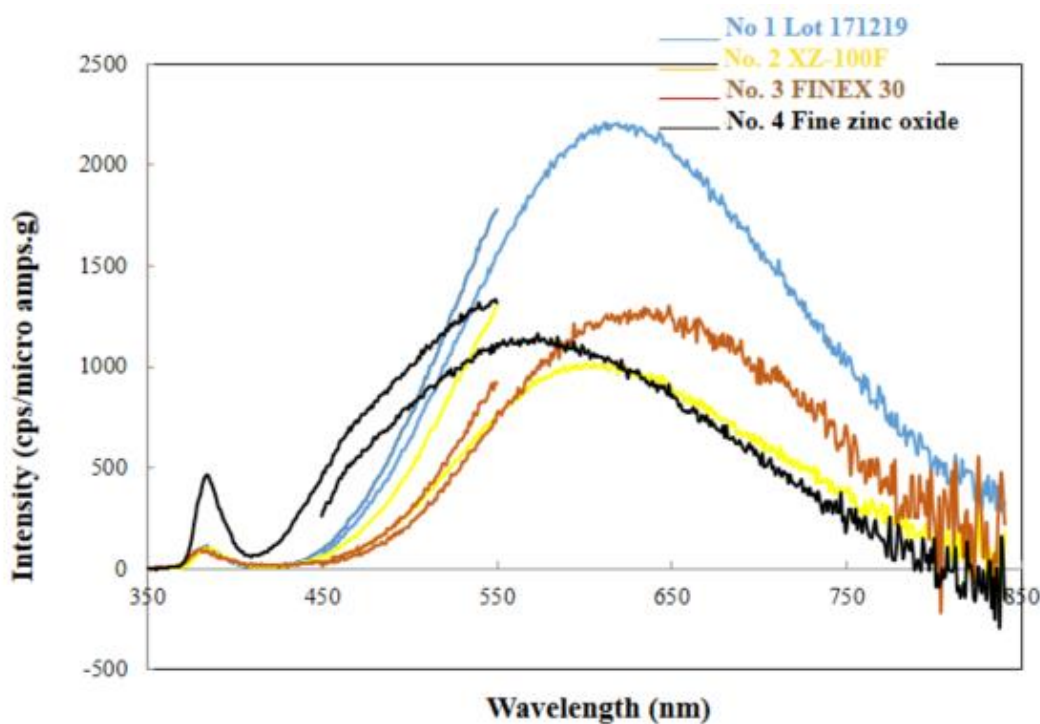
Fig. 3-5 PL spectra of 4 kinds ZnO powders.

XPS analysis as shown in Fig. 3-6 was utilized to understand the surface chemical state of 4 kinds ZnO. Oxygen vacancy Vö peak is clearly observed in No. 1 antibacterial ZnO sample. Moreover, Zn $2p_{3/2}$ peak of No. 1 sample shifted to higher binding energy of 0.2 eV. This peak shift would be caused by electron density of Zn^{2+} core level affected by Vö. Therefore, No. 1 antibacterial sample has many active site/surface areas. The surface Vö intensity of No. 3 sample is the almost same intensity as the other non-treated samples. However, the surface area of No. 3 is much higher than other samples, so the total active-site number is much more than

those of other non-treatment samples. The antibacterial effect of No. 3 might be due mainly to its high surface area.
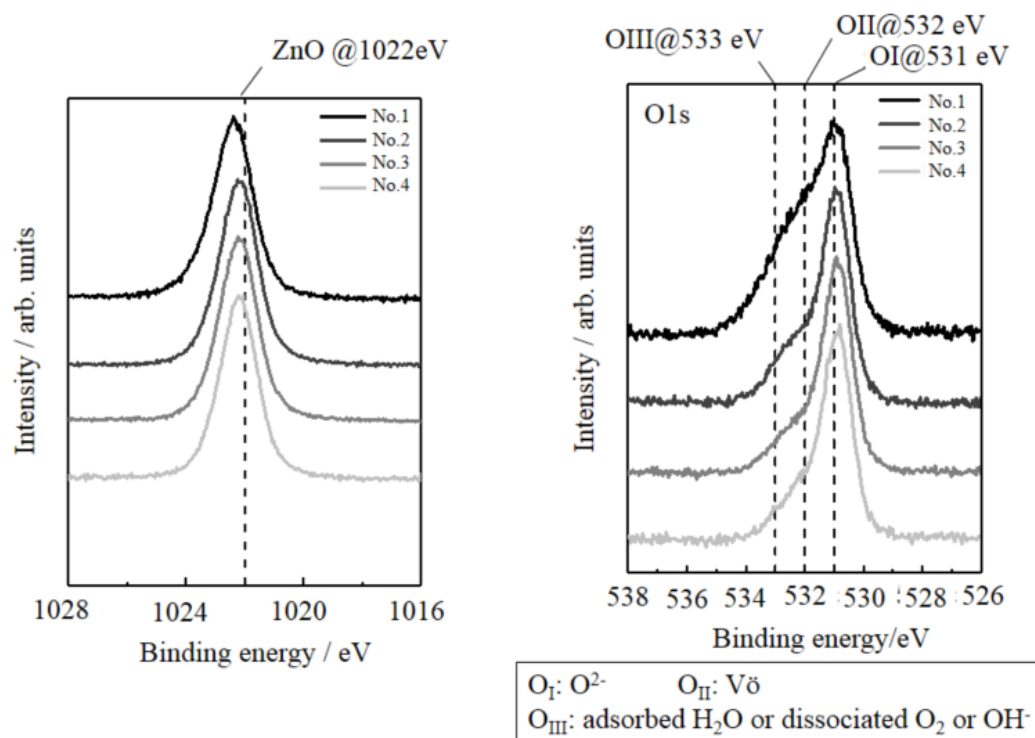
Fig. 3-6 XPS spectra of Zn $2p^{3/2}$ peak and oxygen $1s$ peak.

3.3.2 ROS from the ZnO surface

The determination of which kind of reactive oxygen species ROS generated from the ZnO surface was conducted using various methods. At first, CL-scavenger method was applied; in this method, a specific scavenger that can trap the corresponding ROS. In Fig. 3-7, the blue and red curves are CL ones before and after scavenger-addition, respectively. For example, in No. 1 as the representative sample, the CL intensity is strongly decreased after addition of scavenger such as 2-propanol, 2,5-dimethyl furan, riboflavin, and nitro blue tetrazolium; they can trap hydroxyl radical ·OH, singlet oxygen $^1O_2$, hydrogen peroxide H_2O_2, and superoxide

61

radical $\cdot O_2^-$, respectively. Therefore, it would be concluded that No. 1 sample could submit all 4 kinds of ROS such as $\cdot OH$, $^1O_2$, H_2O_2 and $\cdot O_2^-$.
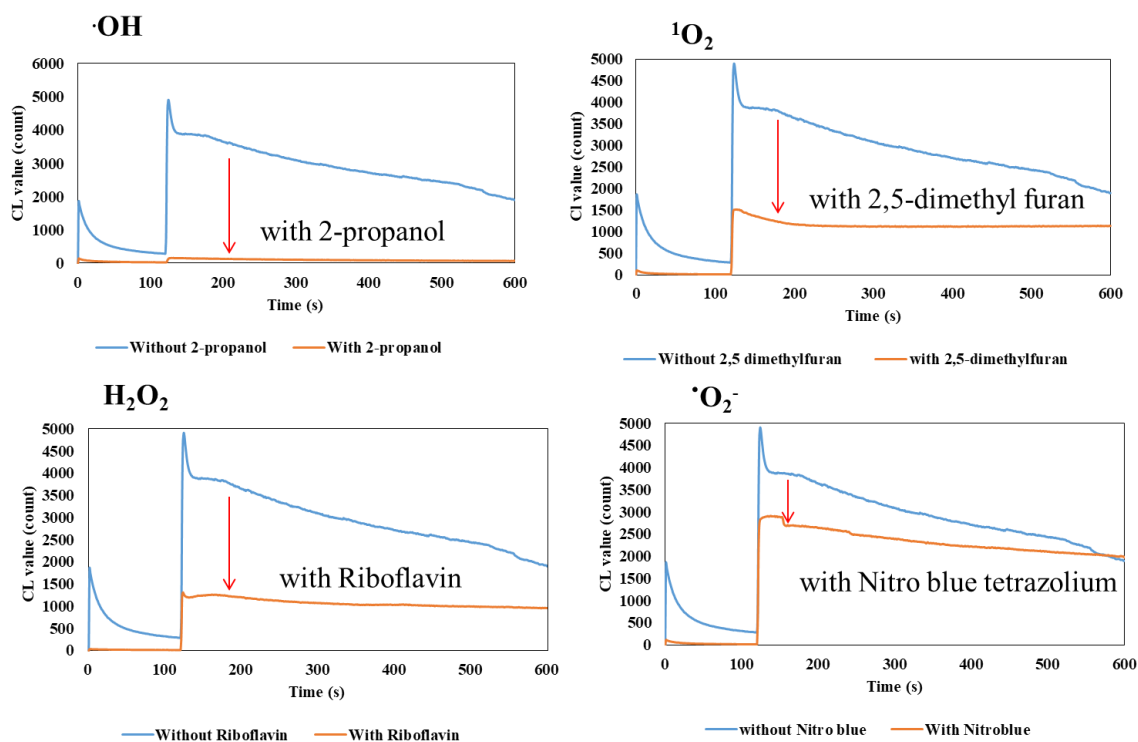
Fig. 3-7 CL-scavenger for No.1 ZnO powder.

Figure 3-8 represents that the combination of CL-scavenger curves for No. 2, 3 and 4 ZnO powders. Each powder only submits one kind of ROS; No. 2 $\cdot O_2^-$, No. 3 H_2O_2 and No. 4 $\cdot OH$. To confirm the results obtained from CL-scavenger method, another testing method, which called, bio-test with scavenger was utilized. The principle of this method is near the same as CL-scavenger method, in other words, some specific scavengers (catalase [H_2O_2], superoxide dismutase SOD [$\cdot O_2^-$], 10% DMSO [$\cdot OH$]) which can catch the corresponding ROS to ZnO powders: (1), (2), (3) and (4) correspond to No. 1, No. 2, No. 3 and No. 4, respectively, in Fig. 3-9, were adopted. At first, 10% dimethyl sulfoxide DMSO which is a scavenger for

·OH radical, was used for the first testing conditions. As shown in Fig. 3-9, after 8.64×10^4 s testing on *E*. coli under dark conditions, all samples proved that they could kill all bacteria. These results are not consistent with the CL-scavenger results, so that the number of bacteria was increased from 10^5 to 10^7 / mL and also the amount of ZnO powder was decreased from 1.0×10^{-4} to 1.0×10^{-5} kg, the results are also shown in Fig. 3-9. From this, it is easily noticed that both No. 1 and 2 ZnO powders could submit ROS under dark conditions.
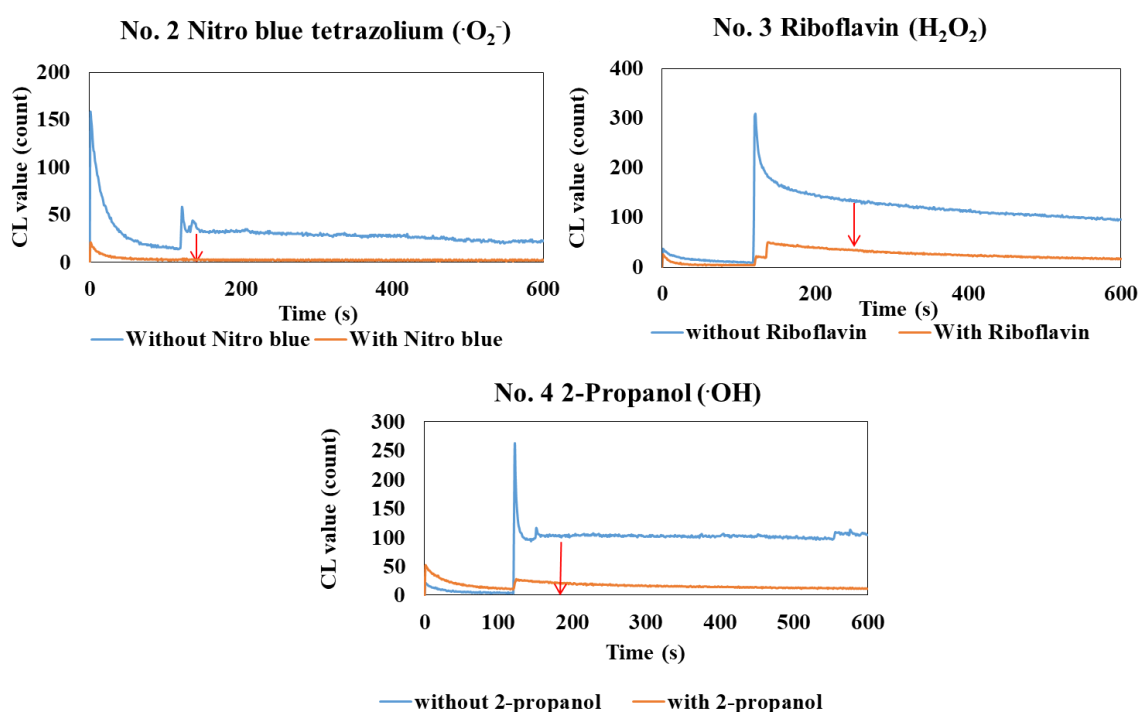
Fig. 3-8 CL-scavenger for No. 2-4 ZnO powders.
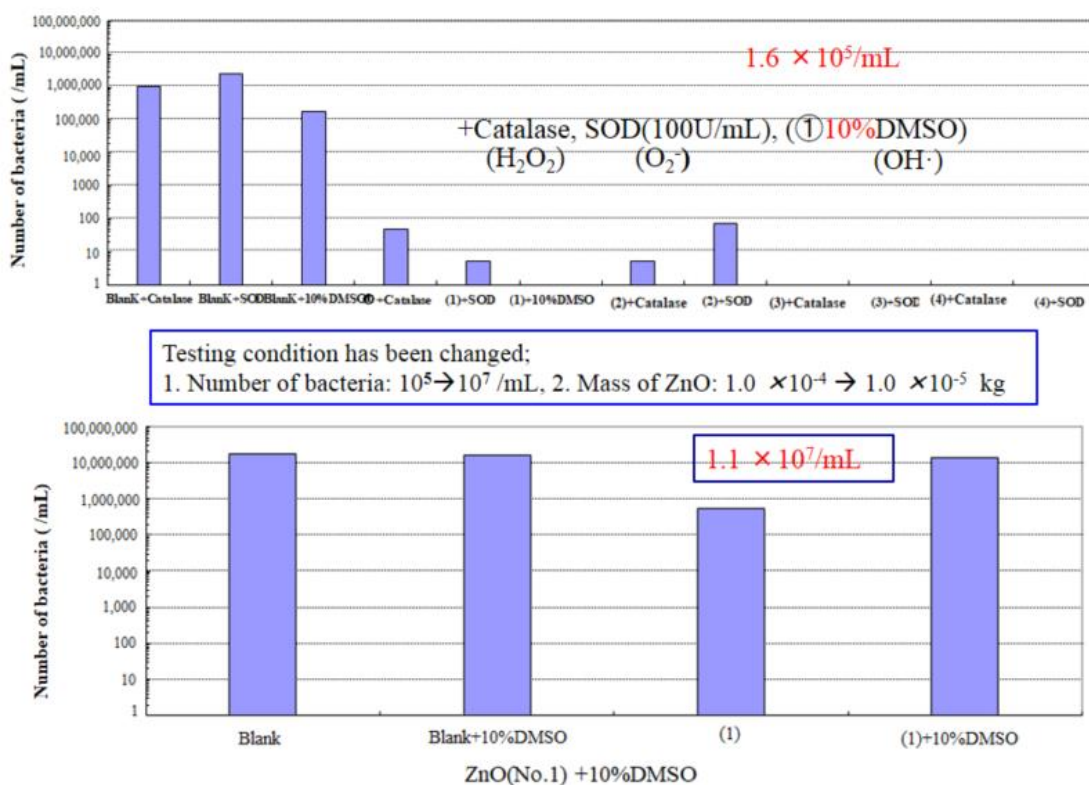
Fig. 3-9 Bio-test using scavengers under dark conditions.

From the results of CL and bio-test with scavengers, Table 3-3 summarizes what kinds of ROS are emitted from each sample ($\circ$: submission of ROS was confirmed by the above-mentioned measurement, $\times$: no submission, **-** : submission process itself was not performed); No 1, as mentioned, submitted all ROS. No. 2 XZ-100F generates hydrogen peroxide (H_2O_2) and superoxide radical ($\cdot O_2^-$). No. 3 two kinds of ROS $i.e.$, H_2O_2 and $\cdot O_2^-$, and No. 4 three kinds of hydroxyl radical ($\cdot OH$), H_2O_2 and $\cdot O_2^-$, respectively.

Table 3-3 Summary of ROS submitted from 4 kinds of ZnO powders

Sample	$\cdot OH$		H_2O_2		$^1O_2$		$\cdot O_2^-$	
	CL	Bio-test (DMSO)	CL	Bio-test (catalase)	CL	Bio-test	CL	Bio-test (SOD)
No. 1 Antibacterial ZnO	○	○	○	○	○	−	○	○
No. 2 XZ-100F	x	−	x	○	x	−	○	○
No. 3 FINEX 30	x	−	○	○	x	−	x	○
No. 4 Fine zinc oxide	○	−	x	○	x	−	x	○

○: submission of ROS was confirmed, × : no submission, - : submission process was not performed.

3.3.3 Bio-test results

Finally, MRSA which is very famous as resistant bacteria and harmful to patients in the hospitals, was bio-tested in Kobe Center of Japan Textile Products Quality and Technology Center; all 4 kinds ZnO powers revealed antibacterial activity on MRSA even under dark conditions, Table 3-4 shows the results of MRSA bio-test after 8.64×10^4 s at 309 K, all ZnO powders killed almost 100% the amount of bacteria.

Table 3-4 MRSA test

Germ (Bacteria)	Object (samples)	Concentration	Number of active germs (/mL)	
			before	after 8.64×10^4 s
MRSA	antibacterial ZnO	1 mass%	-	< 10
	XZ-100F	1 mass%	-	< 10
	FINEX-30	1 mass%	-	< 10
	Fine zinc oxide powder	1 mass%	-	< 10
	Reference		1.9×10^5	1.1×10^5

Reference: a physiological salt

Culture condition: 298 K in the shading

< 10: not detected

3.4 Conclusions

Although all ZnO powders revealed strong antibacterial activity under dark conditions, we found a new relationship between the antibacterial properties and physico-chemical properties from the results of the δ in nonstoichiometric compound $Zn_{1+\delta}O$ and photoluminescence (PL) spectra. As the δ indicates the content of Zn_i in the ZnO lattice, and these Zn_i have strong effect with submission of ROS, and high PL peak at 625 nm also reflects the content of Zn_i, therefore No. 1 antibacterial ZnO powder can produce much ROS continuously. From the application viewpoints, FINEX-30 or XZ-100F can be applicable for one and short time usage.

Acknowledgement

References

1. V. V. Kumar, S. P. Anthony, Antimicrobial studies of metal and metal oxide nanoparticles, Surface Chemistry of Nanobiomaterials, 9(2016), 265-300.

2. G. Applerot, A. Lipovsky, R. Dror, N. Perkas, Y. Nitzan, R. Lubart, A. Gedanken, Enhanced Antibacterial Activity of Nanocrystalline ZnO Due to Increased ROS‑Mediated Cell Injury, Adv. Functional Mater., 19(2009), 842-852.

3. L. K. Adams, D. Y. Lyon, P. J. J. Alvarez, Comparative eco-toxicity of nanoscale TiO_2, SiO_2, and ZnO water suspensions, Water Res., 40(2006), 3527-3532.

4. C. Karunakaran, G. Abiramasundari, P. Gomathisankar, G. Manikandan, V. Anandi, New and future developments in catalysis: solar photocatalysis, Mater. Res. Bull., 46(2011), 1586-1592.

5. J. Sawai, Quantitative evaluation of antibacterial activities of metallic oxide powders (ZnO, MgO and CaO) by conductimetric assay, J. Microbiological Methods, 54(2003), 177-182.

6. K. Hirota, M. Sugimoto, M. Kato, K. Tsukagoshi, T. Tanigawa, H. Sugimoto, Preparation of zinc oxide ceramics with a sustainable antibacterial activity under dark conditions, Ceram. Inter., 36(2010), 497-506.

7. T. M. P. Nguyen, S. Hirota, Y. Suzuki, M. Kato, K. Hirota, H. Taguchi, H. Yamada, K. Tsukagoshi, Preparation of ZnO Powders with Strong Antibacterial Activity under Dark Conditions, J. Jpn. Soc. Powder Powder Metall., 65(2018), 316-324.

8. Y. W. Wang, A. Cao, Y. Jiang, X. Zhang, J. H. Liu, Y. Liu, H. Wang, Superior antibacterial activity of zinc oxide/graphene oxide composites originating from high zinc concentration localized around bacteria, App. Mater. & Interfaces, 6(2014), 2791-2798.

9. B. T. Zhang, L. X. Zhao, J. M. Lin, Study on superoxide and hydroxyl radicals generated in indirect electrochemical oxidation by chemiluminescence and UV-Visible spectra, J. Environmental Sci., 20(2008), 1006-1011.

10. L. Zhang, Y. Ding, M. Povey, D. York, Antimicrobial potential of synthesized zinc oxide nanoparticles against gram positive and gram negative bacteria, Prog. Nat. Sci., 18(2008), 939-944.

11. E. Hoseinzadeha, M. Y. Alikhanib, M. R. Samarghandic, M. S. Sibonid, Desalination and Water Treatment, (2013), 1-8.

12. T. Jin, D. Sun, J. Y. Su, H. Zhang, H-J. Sue, Antimicrobial Efficacy of Zinc Oxide Quantum Dots against Listeria monocytogenes, Salmonella Enteritidis, and Escherichia coli O157:H7, J. Food Sci., 74(2009), 46-52.

13. A. Sirelkhatim, S. Mahmud, A. Seeni, N. H. M. Kaus, L. C. Ann, S. K. M. Bakhori, H. Hasan, D. Mohamad, Review on Zinc Oxide Nanoparticles: Antibacterial Activity and Toxicity Mechanism, Nano-Micro Lett., 7(2015), 219-242.

14. Z. Cheng, H. Zhou, J. Yin, L. Yu, Electron Spin Resonance Estimation of Hydroxyl Radical Scavenging Capacity for Lipophilic Antioxidants, Journal of Agricultural and Food Chem., 55(2007), 3325-3333.

15. L. Wang, C. Hu, L. Shao, The antimicrobial activity of nanoparticles: present situation and prospects for the future, Inter. J. Nanomedicine, 12(2017), 1227-1249.

16. L. Irimpan, V. P. N. Nampoori, P. Radhakrishnan, A. Deepthy, B. Krishnan, Size dependent fluorescence spectroscopy of nanocolloids of ZnO, J. App. Phys., 102(2007), 063524.

17. A. Kołodziejczak-Radzimska, T. Jesionowski, Zinc Oxide - From Synthesis to Application: A Review, Mater., 7(2014), 2833-2881.

18. J. Gupta, D. Bahadur, Defect-Mediated Reactive Oxygen Species Generation in Mg-Substituted ZnO Nanoparticles: Efficient Nanomaterials for Bacterial Inhibition and Cancer Therapy, ACS Omega, 3(2018), 2956-2965.

19. K. Vanheusden, W. L. Warren, C. H. Seager, D. R. Tallant, J. A. Voigt, Mechanisms behind green photoluminescence in ZnO phosphor powders, J. App. Phys., 79(1996), 7983-7990.

20. C. Eggeling, J. Widengren, R. Rigler, C. A. M. Seidel, Photobleaching of Fluorescent Dyes under Conditions Used for Single-Molecule Detection: Evidence of Two-Step Photolysis, Anal. Chem., 70(1998), 2651-2659.

CHAPTER 4

The Study of Physicochemical Properties of Antibacterial ZnO Powder - Impurity Doping, Elution and Catalytic Properties

4.1 Introduction

With the recent health-oriented and lifestyle changes, research and development of materials to remove and kill harmful bacteria for human body is energetically carried out [1-4]. The main antibacterial agents are quaternary ammonium salts and phenols. There are organic antibacterial agents, composite materials in which silver ions and silver nano particles having antibacterial properties which are supported on zeolite and activated carbon, and inorganic antibacterial agents such as TiO_2 utilizing optical activity [3-6]. Antibiotics, anticancer agents, oxidizing agents, etc. can be mentioned as organic antibacterial agents, which can be divided into 19 series of alcohol type, phenol type, ester type, epoxy type, organic metal type etc. according to the chemical structures [3,4]. These antibacterial activities are used as preservatives, pesticides, and cleaners for cosmetics because they could directly contact and absorb microorganisms and act on them. However, in recent years there are substances that have been found to have adverse effects on the human body and the environment, and it is necessary to review their use and to be noticed. Inorganic antibacterial agents are widely used in household goods such as mobile phones, touch panels, toilets, air conditioner filters, etc. In

addition, it can be said that it is characterized by its superior heat resistance and duration compared to organic antibiotics [4-6].

Reactive oxygen, a type of oxygen, contributes to physiological metabolism and plays an important role in maintaining life, such as production of physiologically active substances and removal of pathogens [7, 8]. In general, in the case of inorganic antibacterial agents that generate this active oxygen, as seen in the example of TiO_2, when light energy over the band gap is irradiated to the photocatalyst. Electrons move from the valence band to the conduction band, and electrons are generated in the conduction band, resulting in holes in the valence band [6]. As a result, electrons and holes possessed by the antibacterial material take part in the chemical reaction on the surface to generate active oxygen [7, 8]. However, in the case of ZnO, since it exhibits antibacterial activity due to active oxygen without using light energy, electron e- emitted from interstitial zinc Zn_i and interstitial zinc $Zn_i^{..}$ ionized to divalent valence plays the same role as a hole that is conceivable [9, 10].

One of the problems with inorganic antimicrobial agents is that they require light irradiation. The presence of active oxygen is required to have antibacterial properties, but conventional major inorganic antibacterial agents such as silver zeolite antibacterial agents and titanium dioxide antibacterial agents generate active oxygen species (hydroxyl radical $^.$OH). It is necessary to become ions and radicals by photoexcitation itself, and ultraviolet light energy is required in its generation process [7]. In order to excite light, they have to absorb photons with energy equivalent to the band gap, but the light in the ultraviolet region is usually less than 5% of the sunlight we receive, which will absorb sunlight sufficiently. As one improvement measure, it is possible to extend the light absorption wavelength range to lower energy with

longer wavelength side by supporting the dye having absorption wavelength range from visible region to infrared region on the surface of TiO_2 [5-7]. That is, instead of the direct absorption of light by an antimicrobial substance, the supported dye substance causes a reaction by absorbing light of a longer wavelength. However, this method has not been successfully put to practical use at present. As mentioned above, titanium dioxide antibacterial agents need a place where light energy can be used in order to have antibacterial activity. Also, the antibacterial mechanism of silver zeolite antibacterial agent has silver ion theory other than active oxygen theory [11,12], and it has been clarified that it has antibacterial activity without light energy, but it requires silver, the problem is that it costs a lot to produce.

Recently, ZnO is taking much attention as an antibacterial material that solves the above-mentioned problems. ZnO has the advantages of being relatively inexpensive compared to other heavy metals, and of being less susceptible to light energy for excitation and having antibacterial activity even in the dark, so it is one of advantages of ZnO compared to titanium dioxide antimicrobial agents [1-4]. ZnO is widely synthesized from polycrystals to single crystals, and its structure also begins in bulk or thin film, and exhibits a very diverse aspect such as nanorods and nanoballs. ZnO is noted as a material with diverse optical and electrical characteristics. It is expected to be applied to a wide range of applications such as transparent conductive films, sensors, semiconductor optical and electronic devices, optical circuits, nanodevices, and surface-treated thin films.

Our previous studies have shown that ZnO-based materials already have an antibacterial effect against *E. coli* [1, 2]. In addition, ZnO itself does not act directly on microorganisms, but it is expressed by reactive oxygen species such as superoxide anion radical ($^{\cdot}O_2^{-}$) and hydroxyl

radical ($\cdot$OH) generated near the powder surface of the crystal particle. Furthermore, it has been reported that the strength of the antimicrobial activity differs depending on the starting material, hydrothermal treatment conditions, and additives [13-15]. In this research, to obtain antibacterial ZnO powder with higher antibacterial power than before, and also to be used as a water purifier, granules of ZnO that do not dissolve in water and do not pass through the filter of the water purifier was obtained [16-18]. Moreover, for the evaluation of the tactile properties, the catalytic properties of ZnO are investigated by using acetaldehyde [19, 20].

4.2 Experimental procedure

4.2.1 Preparation of ZnO powders

4.2.1.1 Hydrothermal synthesis

As shown in Fig. 4-1 (I), fine ZnO powder (XZ-100F, Sakai Chemical Industry Co., Ltd., Sakai, Osaka, Japan) with a BET surface area S_A of 7.83 m^2/g, i.e., particle size P_s of 0.137 μm, calculated from both S_A and its theoretical density (D_x) of 5.606 Mg/m^3 (PDF: #36-15451), was used as the starting material. In addition, an aqueous solution of 3.0 M was prepared using zinc nitrate hexahydrate $Zn(NO_3)_2 \cdot 6H_2O$ (purity of 99%, Nacalai Tesque, Kyoto, Japan). 1.0×10^{-4} m^3 of this solution was put into a Teflon wide-mouthed beaker with 2.0×10^{-2} kg of the above ZnO powder. Next, the wide-mouthed beaker was sealed in a high-pressure vessel (autoclave: 48.0 mm in inner diameter and 78.0 mm in height), and hydrothermal synthesis was performed at 443 K for 2.52×10^4 s. After hydrothermal synthesis, the powder was taken out from the autoclave, ultrasonic washing of the powder suspension obtained was performed for 6.0×10^2 s, hot water (333 K) washing was performed for 1.8×10^3 s then it was dried at 383

73

K for overnight. After drying, the powder was lightly crushed in a mortar to make it homogeneous.
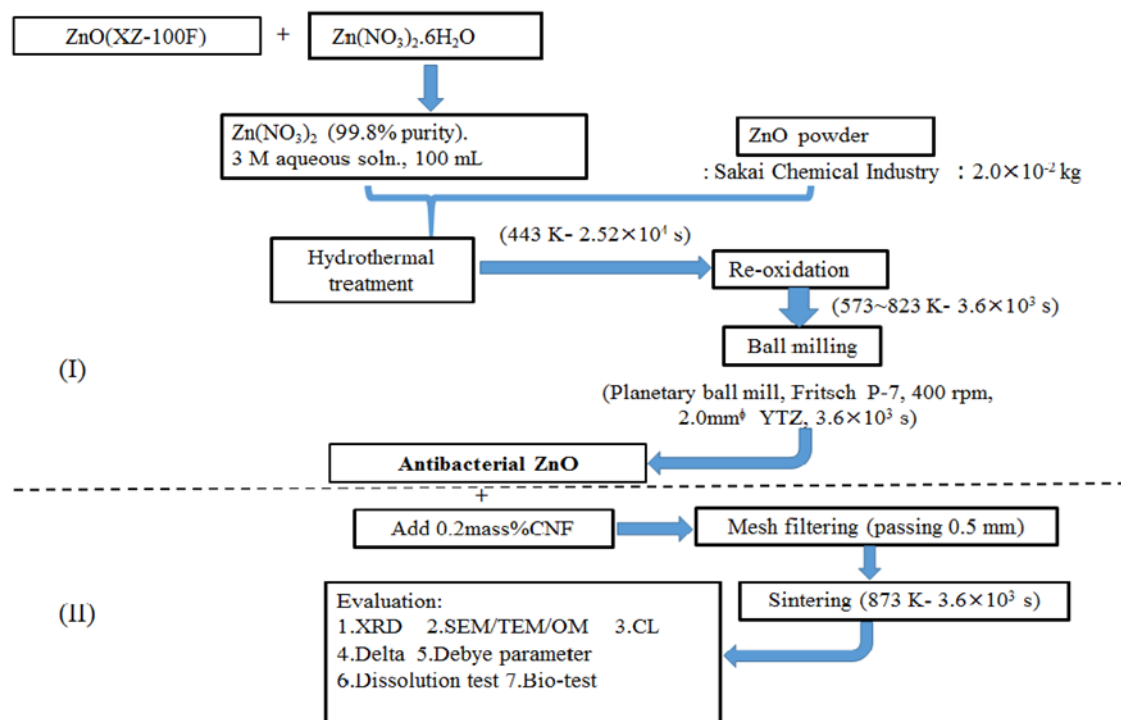
Fig. 4-1 Flowchart for preparation of antibacterial ZnO powders.

4.2.1.2 Heat treatment

Hydrothermally synthesized and dried powders were heated at various temperatures as following conditions: from 573 K to 973 K at 25 K intervals for 3.6×10^3 s to re-oxidize the products which are Zn basic chemical compounds just after hydrothermal treatment.

4.2.1.3 Ball-milling

Pulverizing of ZnO powder of 5.0×10^{-3} kg was performed using a planetary ball-milling apparatus (P-7, Fritsch Japan, Yokohama, Japan), zirconia 45 mL-container, and 2.0

mm diameter yttria-stabilized tetragonal ZrO_2 (YTZ) balls of 5.0×10^{-2} kg with powder : ball = 1 : 10 mass ratio in 1.0×10^{-5} m^3 ethanol, at 6.67 rounds per sec (400 rpm, gravitational acceleration unit : 10.91 g) for 3.6×10^3 s.

4.2.1.4 Hydrothermal synthesis with additives

ZnO powder (XZ-100F) was used as the starting material. And 1.0×10^{-4} m^3 of 3.0 M $Zn(NO_3)_2 \cdot 6H_2O$ aqueous solution and nitrate Lithium $LiNO_3$ (purity 97%, Nacalai Tesque), gallium (III) nitrate pentahydrate $Ga(NO_3)_3 \cdot 5H_2O$ (purity 99.9%, High Purity Chemical Laboratory, Saitama, Japan), aluminum nitrate (III) nonanhydrate $Al(NO_3)_3 \cdot 9H_2O$ (99.9%, High Purity Chemical Laboratory) and magnesium (II) nitrate hexahydrate $Mg(NO_3)_2 \cdot 6H_2O$ (purity 99%, High Purity Chemical Laboratory) together with 2.0×10^{-2} kg of the starting ZnO powder were performed hydrothermal treatment at 443 K for 2.52×10^4 s. After hydrothermal synthesis, obtained powder was ultrasonically washed in hot water for 1.8×10^3 s, and dried at 383 K in air, and lightly crushed to obtain an antimicrobial agent sample.

4.2.1.5 Preparation of granules using cellulose nanofiber (CNF)

Fig. 4-1 (II) shows the procedure of preparing ZnO granules. First, the heat treatment temperature performed which described in 4.2.1.2 was applied to prepare granules, and 0.2 mass% CNF (Dai-ichi Kogyo Seiyaku, Kyoto, Japan, RHEOCRYSTA I-2SX) was added into ZnO powder and passed through #10 mesh filter. Then, thus obtained granules were heated at various temperatures from 373 K to 973 K at 25 K intervals in air. Next, the granules which were added with 0.1, 0.2, 0.3 and 0.4 mass% CNF were prepared by heating at 673 K for 3.6×10^3 s in air.

4.2.1.6 Addition of ZnO to porous material

1.0% CNF aqueous solution, pure water and antibacterial ZnO powder were added into a 5.0×10^{-4} m^3 three-necked flask and stirred. While stirring the solution, Si/SiC porous filter and apatite-based porous material (BA9-800) was soaked for 60 s and then dried. Furthermore, after repeating this step three times, heat treatment was performed at 873 K for 3.6×10^3 s in air.

4.2.2 Evaluation

4.2.2.1 X-ray diffraction

Crystalline phase and crystallite size were investigated by performing X-ray diffraction (XRD, SmartLab, Rigaku, Osaka, Japan) with a monochromator on all samples. The lattice constants were determined by XRD using high-purity Si as an internal standard under the condition of $30° < 2\theta < 90°$.

4.2.2.2 Chemiluminescence (CL) measurement

Chemiluminescence (CL) [1, 2] of ZnO powders (100 μmol) in a 2.5×10^{-7} m^3 aqueous luminol solution (5.0×10^{-9} mol·m^{-3}) mixed with 3.0×10^{-6} m^3 carbonic acid buffer solution (NaOH/NaHCO$_3$, pH=10.8) was observed under dark conditions using a CL detector (CLD-100FC, Tohoku Electronic Industrial Co., Ltd., Sendai, Japan) [6]. After dropping the luminol solution in a 1.2×10^2 s' warming up of the detector, the intensity of CL was integrated between $1.2 \sim 6.0 \times 10^2$ s.

4.2.2.3 Dissolution test

Dissolution test for Zn was performed under JIS S 3200-7: equipment of water supply - test method of effect to water quality, 4th edition, October 1, 2008 (Japanese Standard Association). At first we prepared an exudate fluid with the conditions of pH=7.0±0.1, hardness of water, 45±5 mg/L, alkaline level, 35.5±5 × 10^{-3} kg·m^{-3} and residual chlorine concentration, 0.3±0.1 × 10^{-3} kg·m^{-3}.

Four ZnO test pieces were prepared; 1) antibacterial ZnO powder as a reference, 2) ZnO granules prepared as follows; after hydrothermal treatment, washed and dried powder, namely HT material, heated at 573 K for 3.6×10^3 s in air, then pulverized and was added with a small amount of 0.3% cellulose nano fiber (CNF) added and passed through #10 filter, and then heated at 873 K for 3.6×10^3 s in air as shown in Fig. 4-1 (II). 3) as the same as 2) except for 573 K-heating, changed into 673 K, and 4) as the same as 2) except for 573 K-heating, changed into 773 K.

Secondly, test pieces were put into testing vessel such as water cleaner contained the exudate fluid and hold inside it for 5.76×10^4 s at 296 K. And then the content of Zn was measured using Inductively Coupled Plasma (ICP, AA-6800, Shimazdu, Kyoto, Japan).

4.3 Results and discussion

4.3.1 Examination of additives

Figure 4-2 shows XRD patterns of ZnO powders doped with various Mg contents from 0.1 to 5mol%. It can be seen that all samples have hexagonal Würzite structure (PDF: #36-1451). There is no second phase beside ZnO and also no significant differences among them.
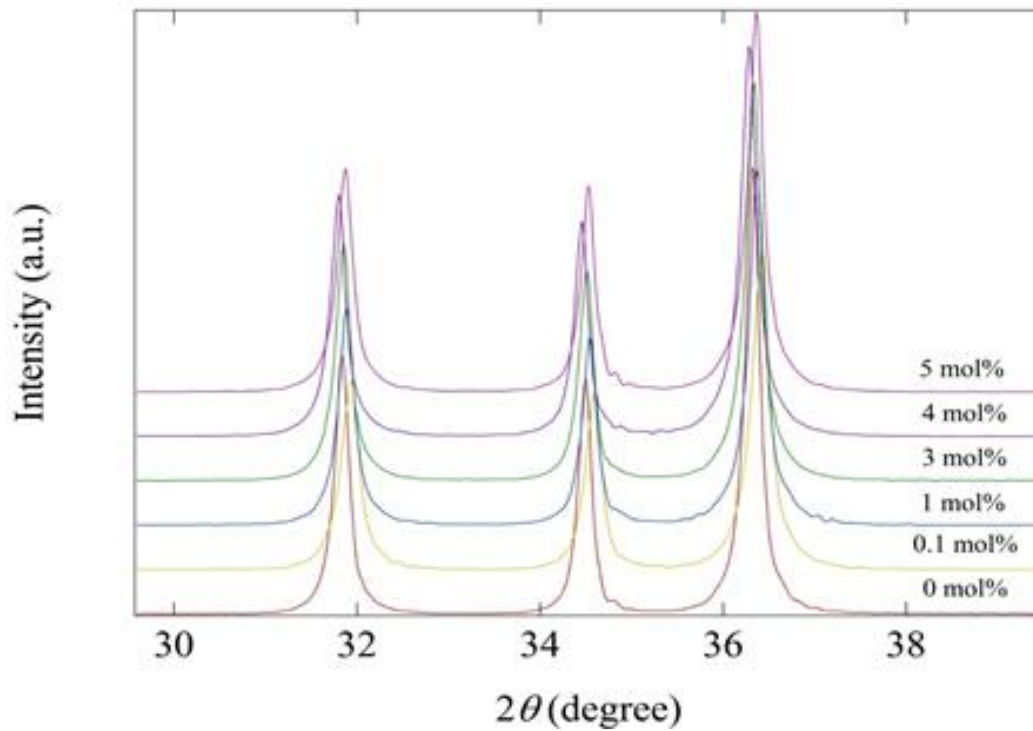
Fig. 4-2 XRD patterns of ZnO powders doped with various amount of Mg.

However, there is a little change in lattice parameters when the contents of input Mg changed as shown in Fig. 4-3, suggesting that ion Mg^{2+} could be inserted into the crystalline structure of $Zn^{2+}O$; here, ionic radii of Mg^{2+} have been reported as 0.057 nm (CN:IV) [20] and 0.0720 nm (CN:VI) [21] and on the other hand, those of Zn^{2+} are 0.060 nm (CN:IV) [20] and 0.0740 nm (CN:VI) [21].
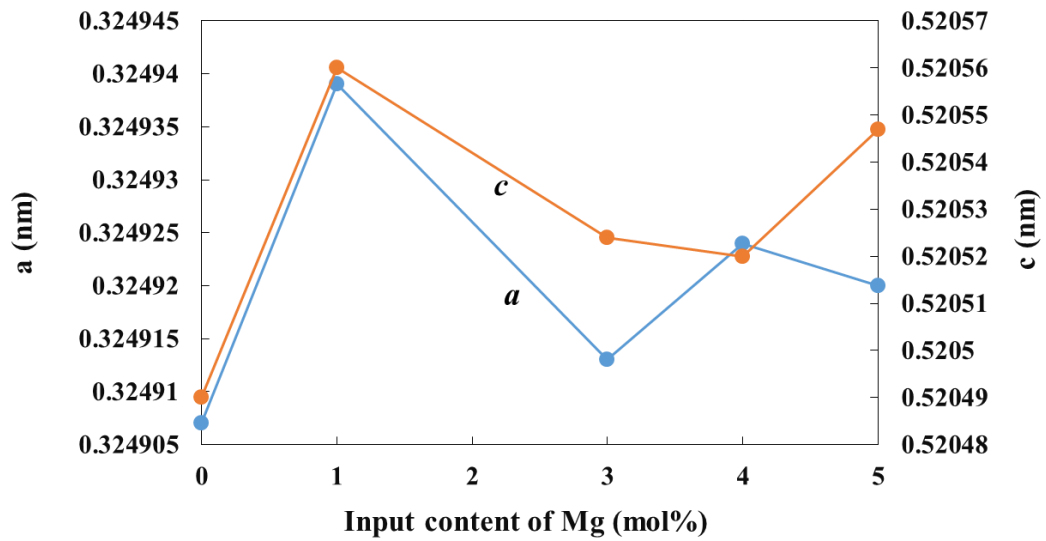
Fig. 4-3 Lattice parameters *a* and *c* of hexagonal ZnO doped with Mg.

Fig. 4-4 reveals the actual amount of additives (Li, Mg) that were obtained by ICP measurement. From these graphs, it can be seen that the contents of both Li^+ and Mg^{2+} that actual adopted into ZnO are very low. It is considered that they were structurally unsuitable, even though their ionic radii are nearly the same; i.e., ionic radii of Li^+ are 0.059 nm (CN:IV) and 0.0760 nm (CN:VI) [20], however, crystal structure of ZnO is hexagonal, on the other hand, those of MgO and Li_2O are cubic.
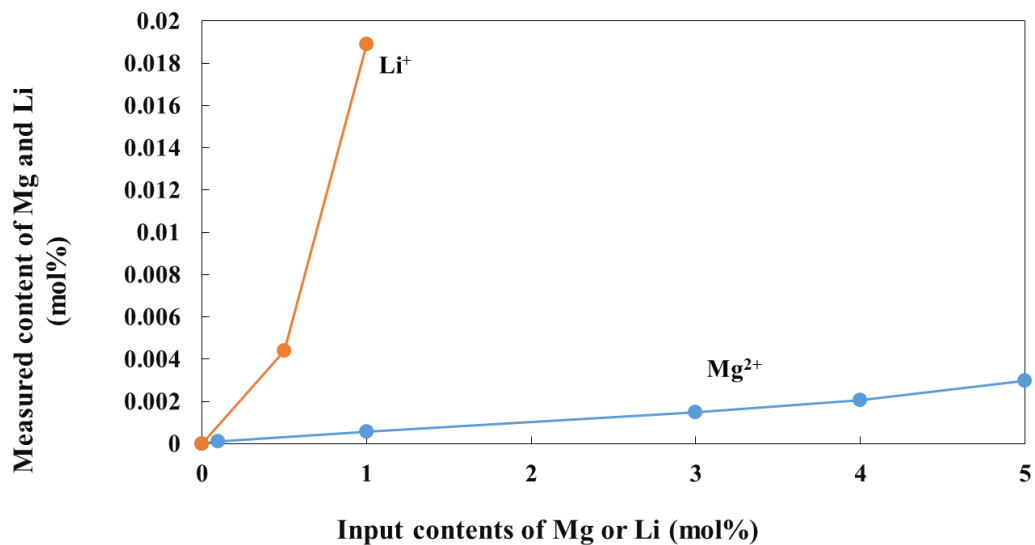
Fig. 4-4 Relationship between input and ICP-measured contents of Mg or Li in ZnO.

Also, the CL measurement results of each sample with Li and Mg as dopants are shown in Fig. 4-5, input additional amounts (mol%) are on the horizontal axis. CL values were decreased with the increasing amount of dopants (Li, Mg). In other words, the antibacterial activity of those samples was decreased since CL value and antibacterial property has strong relationship.
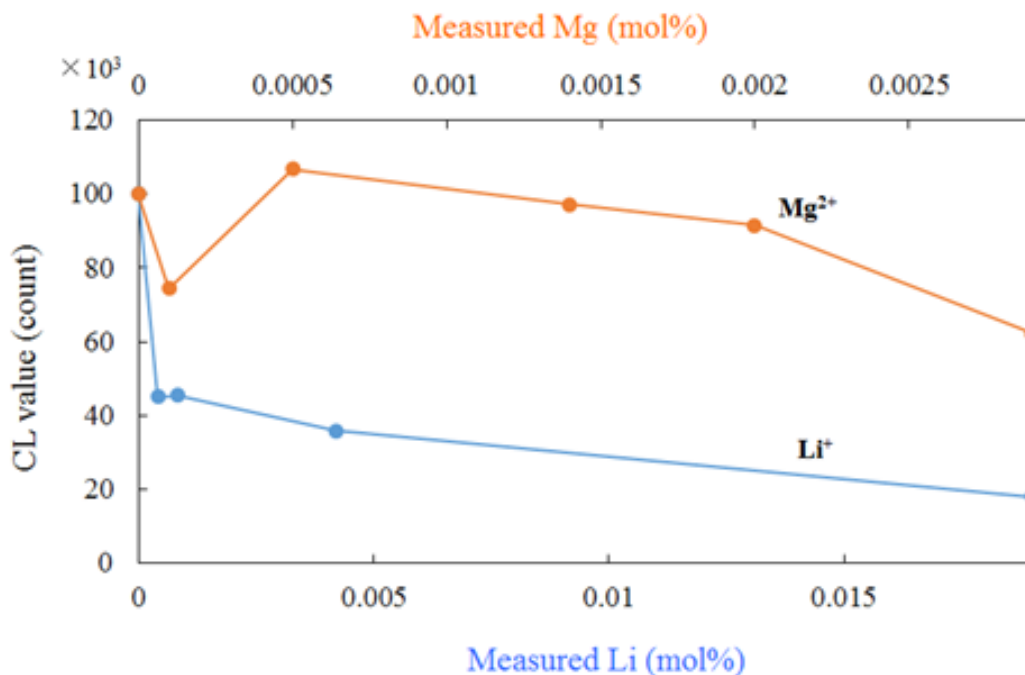
Fig. 4-5 CL values of ZnO powders doped with various contents of Li or Mg.

The same behavior happened with Ga and Al additions as displayed in Fig. 4-6, the integrated CL values were lightly decreased with the increasing the content of additions. This result could be explained basing on the differences in the ionic radii and positive charges of Ga^{3+}, Al^{3+} and Zn^{2+}; radii of Ga^{3+} are 0.047 nm (CN:IV) [20] and 0.0620 nm (CN:VI), those of Al^{3+} are 0.039 nm (CN:IV) [21] and 0.0535 nm (CN:VI), much far away from those of Zn^{2+}. Those differences might affect to the formation of solid solutions. From these results, it could be noted that a small amount of Mg, about 0.0005 mol%, could be inserted into ZnO lattice and improve the CL value about 5%.
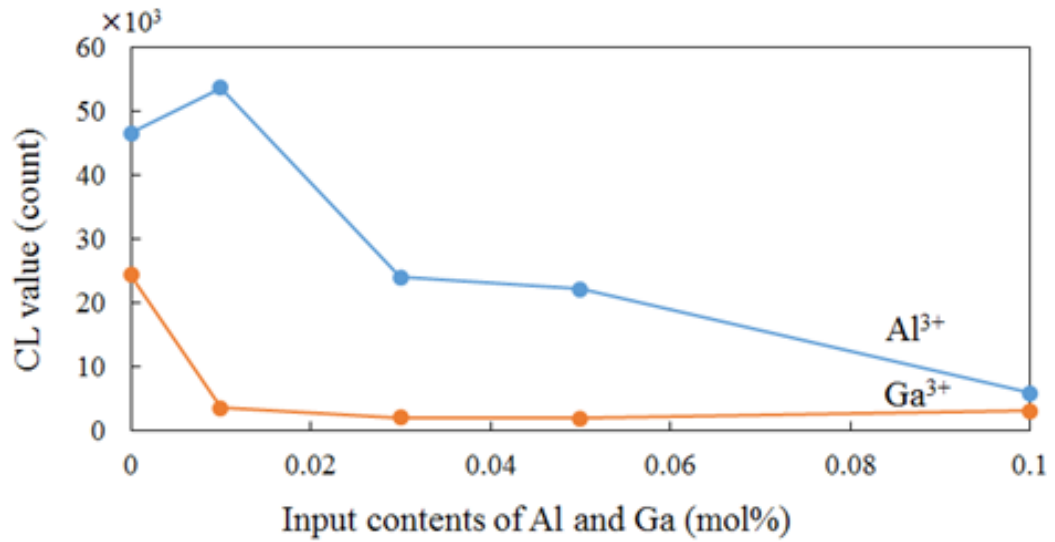
Fig. 4-6 CL value of ZnO powder with various contents of Al or Ga.

4.3.2 Examination of granule ZnO

SEM images of granule ZnO samples with various amounts of CNF are shown in Fig. 4-7. There are a few small differences in their morphologies and granule/particle sizes which might affect to their properties. About 0.3 and 0.4 mass% addition could produce the ZnO granules.
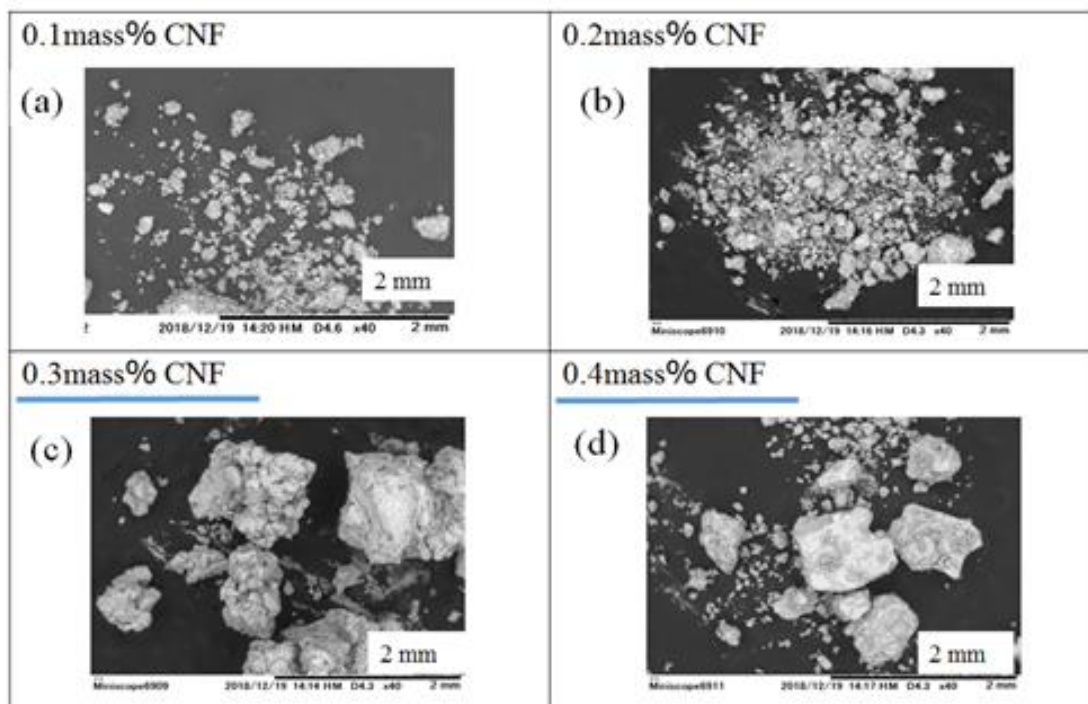
Fig. 4-7 SEM images of ZnO granules prepared using aqueous CNF solutions: (a), (b): 0.2%mass CNF and (c), (d): 0.5%mass CNF.

Figure 4-8 displays the integrated CL value of ZnO granules prepared at various heat treatment temperatures (a) without addition and (b) with the addition of 0.2 mass% CNF. It is clear that granule ZnO (0.2 mass% CNF) heated at 773 K gave the highest CL value compared to non-added CNF samples and the other heating conditions, and it should be noted that the highest CL temperature of CNF added sample is 100 K lower than that of no addition, suggesting that a small amount of CNF might enhance to sinter or form oxygen vacancies in ZnO lattice due to its carbon component.
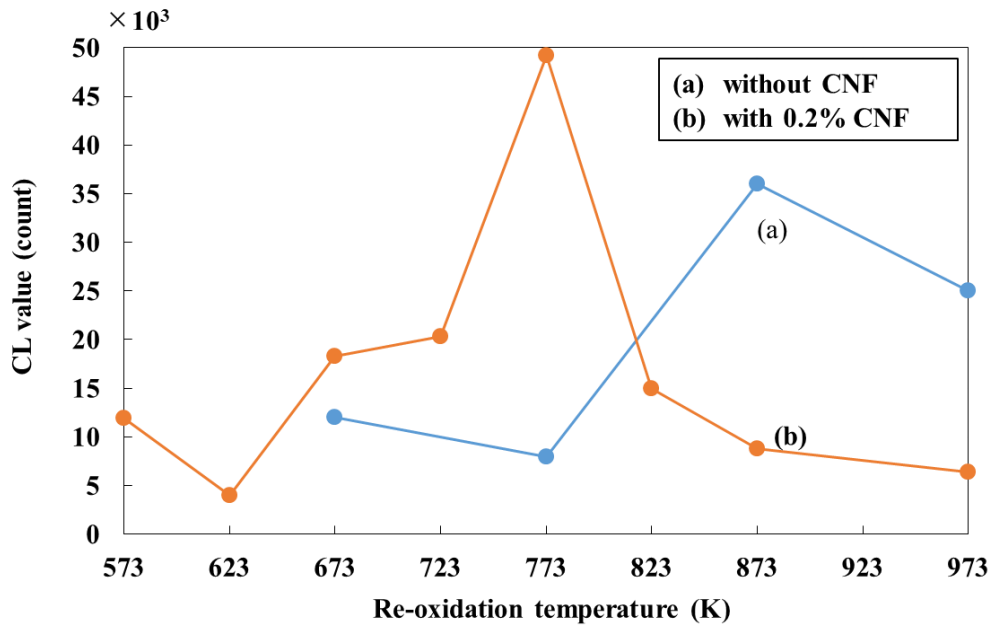
Fig. 4-8 CL values of ZnO powders prepared at various re-oxidized temperatures without and with 0.2% CNF.

Fig. 4-9 (a) shows the change in the integrated CL value of granules as a function of the amount of CNF addition under the condition that the heat treatment temperature was fixed at 773 K. From these results, it can be assumed that the addition of CNF has much effect on the CL value; 0.4 mass% CNF addition gave the highest value. It can be considered that the addition of CNF increased the amount of interstitial Zn [2] during heating at 773 K and resulted in increasing reactive oxygen species (ROS) [1-4]. Therefore, this result can suggest an increase of the antibacterial activity of ZnO granules. Besides, no significant change was observed in the lattice constant, but as shown in Fig. 4-9 (b) and (c) crystallite sizes X_s of the granules with and without mess filter pass increased slightly from 41~42 nm to around 45 nm at 0.4% CNF addition.
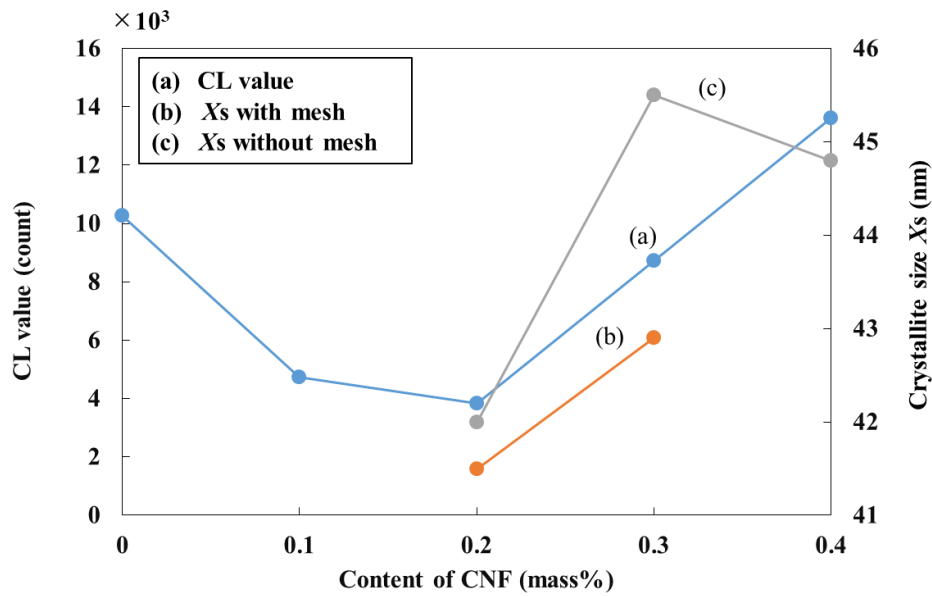
Fig. 4-9 CL value and crystallite size X_s of ZnO granules as a function of contents of CNF.

Table 4-1 shows the eluded Zn content from the 4 test pieces: No. 1 shows 0.16 mg/L (1.6×10^{-4} kg·m^{-3}), here, the content of elution is presented as mg/L unit because of JIS document uses this unit, No. 2; 0.09 mg/L (9.0×10^{-5} kg·m^{-3}), No. 3; 0.05 mg/L (5.0×10^{-5} kg·m^{-3}) and No.4; 0.08 mg/L (8.0×10^{-5} kg·m^{-3}). These values except for 0.16 mg/L for No. 1 sample satisfied the requirement level of 0.1mg/L of JIS S 3200-7. This effect might be explained as follows:

i) The products obtained just after hydrothermal treatment (0.246 M/100 mL, 3 M $Zn(NO_3)_2$ aqueous solution at 443 K for 2.52×10^4 s) washing and drying, are fine reactive powder composed of basic Zn compounds, such as, $Zn(NO_3)_2(H_2O)$, $Zn_3(OH)_4(NO_3)_2$, $Zn_5(OH)_8(NO_3)_2(H_2O)$, and ZnO.

ii) After heating at relatively low temperature above re-oxidation temperature around 553 K, such as 573, 673 and 773 K, the products turned into fine ZnO powders.

iii) A small amount of 0.3% CNF aqueous solutions were added to fine ZnO powders and then mixed powders became massed together, or agglomerated by passing through #10 mesh filter, open grid of 2.0 mm.

iv) These agglomerated powders turned into porous granules after heating at 873 K for 3.6×10^3 s in air, consisting of marginally sintered grains.

v) These granules might show a small amount of Zn elution comparing with that of normally prepared, i.e, after hydrothermal treatment, 873 K oxidizing heating.

Table 4-1 Elution of ZnO granules

Sample	Elution (mg/L)*
Antibacterial ZnO ; 873 K /3.6×10^3 s	0.16
Hydrothermal product-573 K+0.3%CNF+ 873 K /3.6×10^3 s	0.09
Hydrothermal product-673 K+0.3%CNF+ 873 K /3.6×10^3 s	0.05
Hydrothermal product-773 K+0.3%CNF+ 873 K /3.6×10^3 s	0.08

*: the elution of Zn has been evaluated under JIS S 3200-7.

4.3.3 Evaluation of catalyst characteristics

Low magnification SEM images of ZnO added porous materials, such as Si/SiC filter and apatite-based ceramics (BA9-800) are shown in Fig. 4-10, here black round circles and squares are voids.
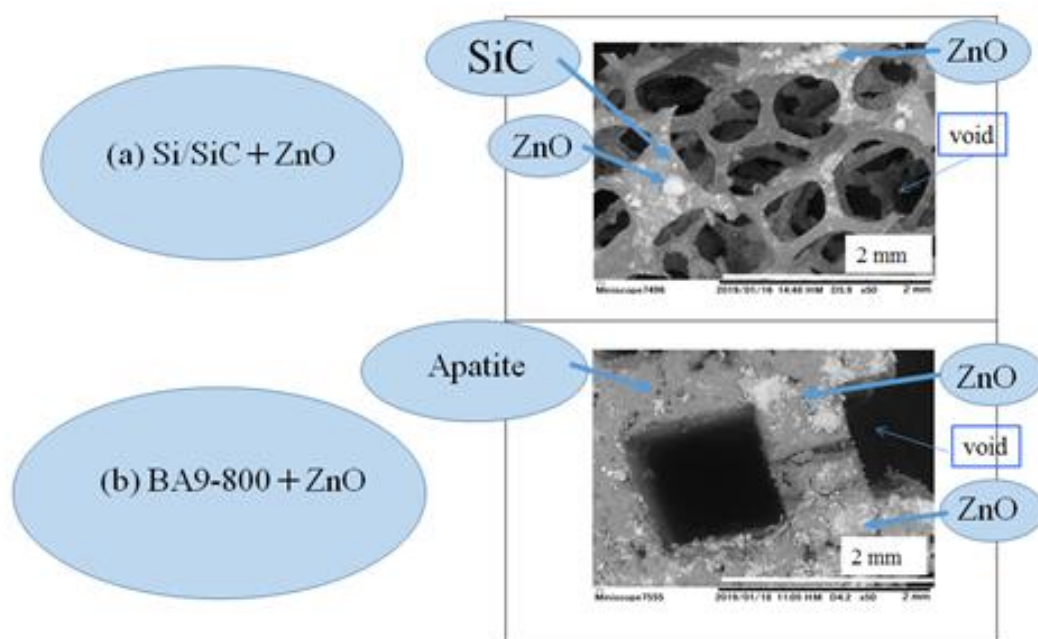
Fig. 4-10   Low magnification SEM photographs for (a) Si/SiC + ZnO and (b) BA9-800+ZnO.

Figures 4-11 and 4-12 show XRD patterns of these Si/SiC+ZnO and BA9-800+ZnO, respectively. In Fig. 4-11, a few small diffraction peaks attributed from ZnO are recognized. However, in Fig. 4-12 no XRD peaks of ZnO are observed, this might be due to strong diffraction generated from relatively denser ceramics with 48% porosity than Si/SiC filter.
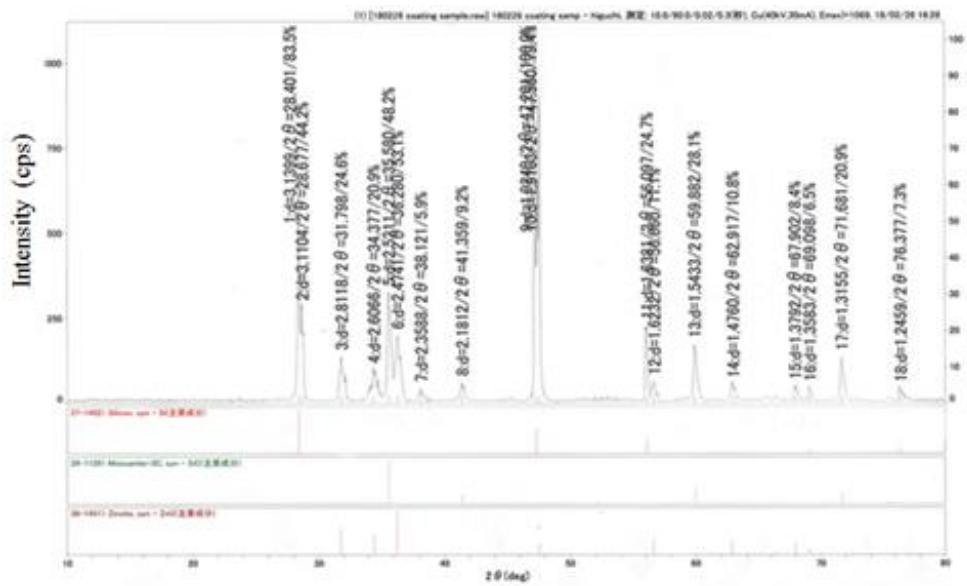
Fig. 4-11 XRD pattern of Si/SiC+ZnO.

Fig. 4-12 XRD pattern of BA9-800+ZnO, red line shows the difference between I_{obs} and I_{calc}

(I_{calc} is refered to PDF#21-1486).
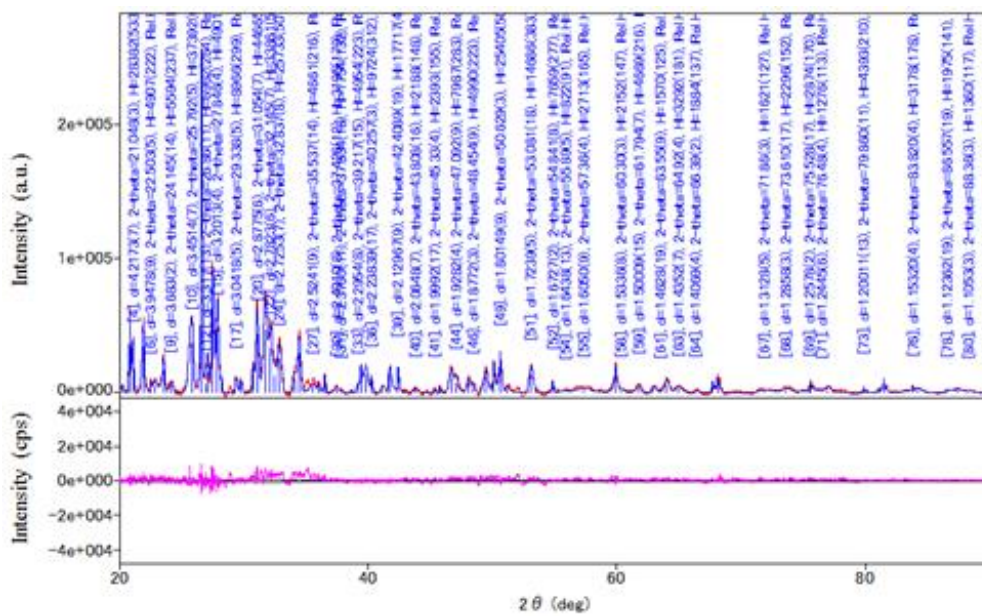
Their microstructures observed by relatively high magnification, such as (a) Si/SiC filter, (b) Si/SiC filter + ZnO powder added, (c) Si/SiC filter + TiO$_2$ powder added, this test piece are used as a reference and (d) BA9-800 + ZnO powder added are shown in Fig. 4-13. By comparison among these former tree samples, Si/SiC filter related, the latter BA9-800 + ZnO consisted of relatively small homogeneous grains and high relative density.
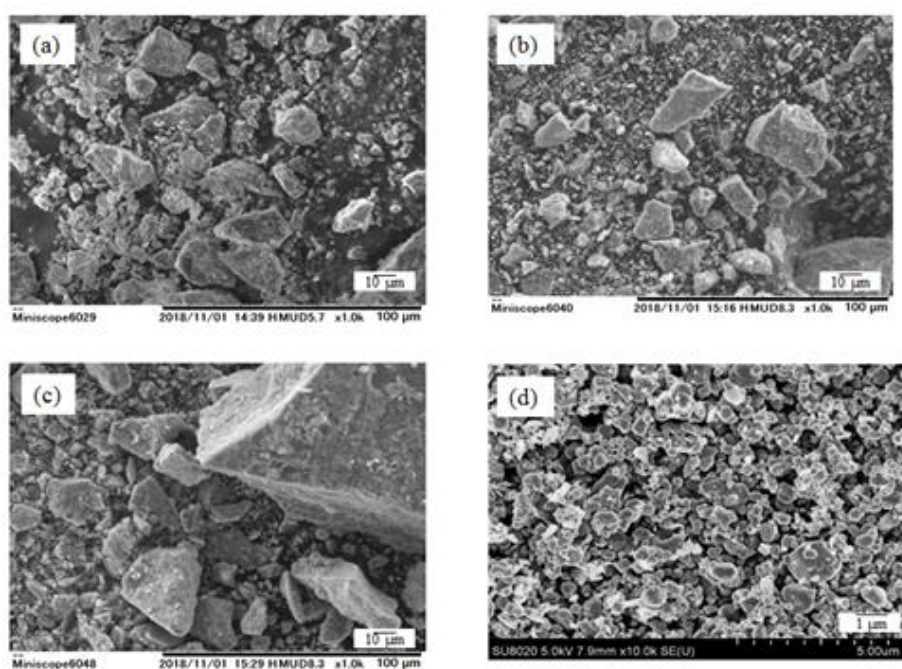
Fig. 4-13 SEM images of (a) Si/SiC porous material, (b) Si/SiC+ZnO, (c) Si/SiC+TiO2 and (d) BA9-800+ZnO.

The changes in concentration of acetaldehyde (CH$_3$CHO, C$_2$H$_4$O), which measured by a gas detector tube (92M, GASTEC Corporation, Ayase, Kanagawa, Japan) using a plastic globe-back with $4.3 \times 4.3 \times 2.5 \times 10^{-6}$ m^3 size and 1.8×10^{-2} m^{-3} volume are shown in Fig. 4-14 and 4-15. In Fig. 4-14 (a) and (b), ZnO added Si/SiC filters reveal rapid a concentration-decrease even under dark conditions, indicating playing a role of catalytic properties for acetaldehyde;

this might be the first report on the catalytic properties of ZnO under dark conditions. Fig. 4-14 (c) and (d) also show catalytic properties of TiO$_2$ powders for acetaldehyde in both daylight and in the dark, this effect has been reported only in sunshine. When the results are compared between Si/SiC filter + ZnO and +TiO$_2$ powders, it seems that ZnO has strong catalytic properties. However, relatively dense BA9-800 + ZnO powder added samples did not show the catalytic properties as shown in Fig. 4-14 (e).
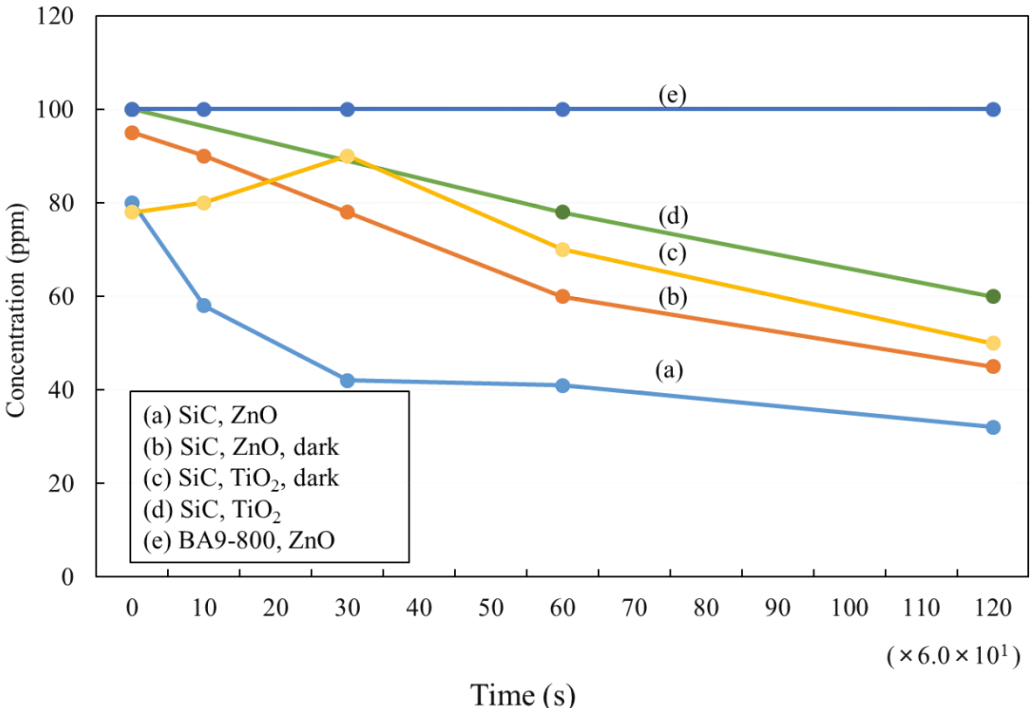
Fig. 4-14 Concentration of acetaldehyde changed in each sample.

Next, Fig. 4-15 shows the time-dependent changes in catalytic capacity F in each sample, here $F=(C_o-C)/(C_o \times W_0)$, C and C_o are the concentration of acetaldehyde at time t and starting at 0, W_0 mass of ZnO and TiO$_2$. From these results, it could be confirmed that the

catalytic properties of ZnO is activated even under light shielding, even though relatively low by comparing the same mass of TiO_2.
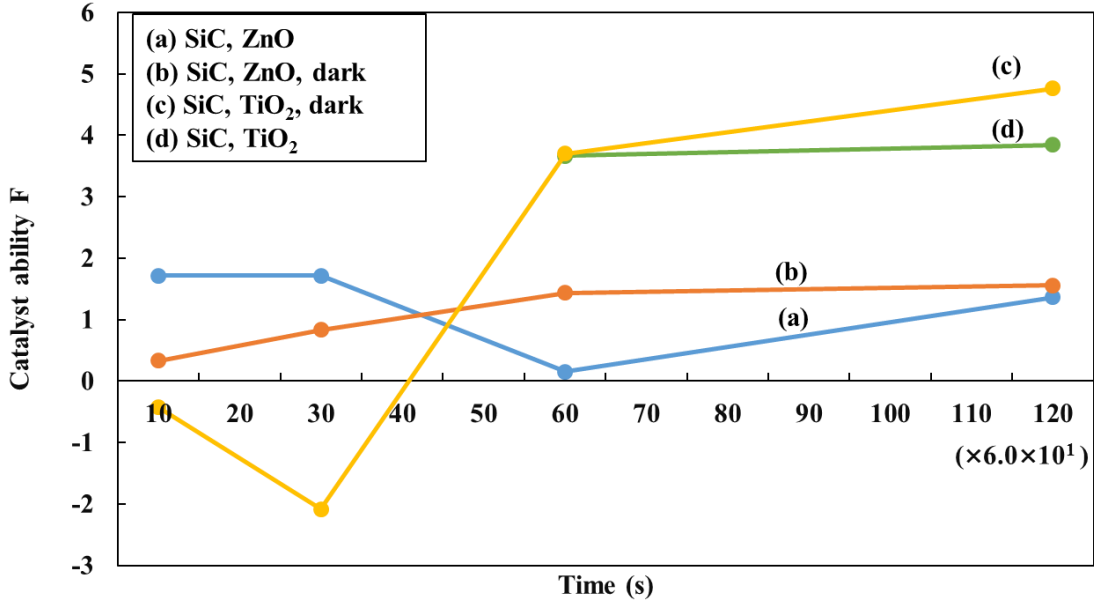
Fig. 4-15 Time-dependent change in catalytic capacity F in each sample: $F=(C_o-C)/(C_o \times W_0)$.

4.4 Conclusion

From this study, it was found from the results of CL measurement that the antibacterial activity was increased by the addition of CNF, and from the results of SEM images that powder close to granules was obtained. Furthermore, from the experiments using acetaldehyde, it could be confirmed that zinc oxide exhibits catalytic properties even in the dark conditions.

References

1. K. Hirota, M. Sugimoto, M. Kato, K. Tsukagoshi, T. Tanigawa, H. Sugimoto, "Preparation of Zinc Oxide Ceramics with a Sustainable Antibacterial Activity under Dark Conditions", Ceram. Inter., 36(2010), 497-506.

2. T. M. P. Nguyen, S. Hirota, Y. Suzuki, M. Kato, K. Hirota, H. Taguchi, H. Yamada, K. Tsukagoshi, "Preparation of ZnO Powders with Strong Antibacterial Activity under Dark Conditions", J. Jpn. Soc. Powder Powder Metall., 65(2018), 316-324.

3. V. V. Kumar, S. P. Anthony, "Antimicrobial Studies of Metal and Metal Oxides Nanoparticles", Surface Chemistry of Nanobiomaterials, 9(2016), 265-300.

4. G. Applerot, A. Lipovsky, R. Dror, N. Perkas, Y. Nitzan, R. Lubart, A. Gedanken, "Enhanced Antibacterial Activity of Nanocrystalline ZnO Due to Increased ROS-Mediated Cell Injury", Adv. Funct. Mater., 19(2009), 842-852.

5. L. K. Adams, D. Y. Lyon, P. J. J. Alvarez, "Comparative Eco-Toxicity of Nanoscale TiO_2, SiO_2, and ZnO water suspensions", Water Res., 40(2006), 3527-3532.

6. C. Karunakaran, G. Abiramasundari, P. Gomathisankar, G. Manikandan, V. Anandi, "Preparation and Characterization of ZnO-TiO_2 Nanocomposite for Photocatalytic Disinfection of Bacteria and Detoxification of Cyanide under Visible Light", Mater. Res. Bull., 46(2011), 1586-1592.

7. S. Ranjan, C. Ramalingam, "Titanium Dioxide Nanoparticles Induce Bacterial Membrane Rupture by Reactive Oxygen Species Generation", Environ Chem. Lett, 14 (2016), 487-494.

8. M. Ohira, H. Liu, D. He, Y. Hirata, M. Sano, T. Suzuki, T. Miyake, Catalytic Performance and Reaction Pathways of Cu/SiO_2 and ZnO/SiO_2 for Dehydrogenation of Ethanol to Acetaldehyde, J. Jpn. Petroleum Institute, 61(2018), 205-212.

9. A. R. Petosa, S. J. Brennan, F. Rajput, N. Tufenki, Transport of Two Metal Oxide Nanoparticles in Saturated Granular Porous Media: Role of Water Chemistry and Particle Coating, Water Res., 46(2012), 1273-1285.

10. H. J. Fan, P. R. Anderson, Copper and Cadmium Removal by Mn Oxide-Coated Granular Activated Carbon, Separation and Purification Technology, 45(2005), 61-67.

11. O. Yamamoto, M. Komatsu, J. Sawai, Zenbe-E. Nakagawa, Effect of Lattice of Zinc oxide on Antibacterial Characteristics, Journal of Materials Science, 15(2004), 847-851.

12. B. T. Zhang, L. X. Zhao, J. M. Lin, Study on Superoxide and Hydroxyl Radicals Generated in Indirect Electrochemical Oxidation by Chemiluminescence and UV-Visible Spectra, Journal of Environmental Sciences, 20(2008), 1006-1011.

13. M. Ohtaki, K. Araki, K. Yamamoto, High Thermoelectric Performance of Dually Doped ZnO Ceramics, J. Electronic Materials, 38(2009), 1234-1238.

14. J. Sawai, Quantitative Evaluation of Antibacterial Activities of Metallic Oxide Powders (ZnO, MgO and CaO) by Conductimetric Assay, Journal of Microbiological Methods, 54(2003), 177-182.

15. E. Hoseinzadeha, M-Y. Alikhanib, M-R. Samarghandic, M. Shirzad-Sibonid, Antimicrobial Potential of Synthesized Zinc Oxide Nanoparticles Against Gram Positive and Gram Negative Bacteria, Desalination and Water Treatment, (2013), 1-8.

16. S. H. Lin, C. L. Lai, Catalytic Oxidation of Dye Wastewater by Metal Oxide Catalyst and Granular Activated Carbon, Environment International, 25(1999), 497-504.

17. G. Singh, E. M. Joyce, J. Beddow, T. J. Mason, Evaluation of Antibacterial Activity of Zn Nanoparticles Coated Sonochemically onto Textile Fabrics, Journal of Microbiology, Biotechnology and Food Sciences, 2(2012), 106-120.

18. J. Fan, R. Freer, The Roles Played by Ag and Al Dopants in Controlling the Electrical Properties of ZnO Varistors, J. Appl. Phys., 77(1995), 4795-4800.

19. Y.W. Wang, L.D. Zhang, G.Z. Wang, X.S. Peng, Z.Q. Chu, C.H. Liang, Catalytic Growth of Semiconducting Zinc Oxide Nanowires and Their Photoluminescence Properties, J. Crystal Growth, 234(2002), 171-175.

20. R. D. Shanon, Revised Effective Ionic Radii and Systematic Studies of Interatomic Distances in Hlides and Chalcogenides, Act. Crystallogr., Set A, 32(1976), 751-767.

CHAPTER 5

Preparation of Anatase Titanium Dioxide Powder Having Strong Antibacterial Activity under Dark Conditions by Co-doping of K and P

5.1 Introduction

Mainly three crystal structures are reported in titanium dioxide; low-temperature form tetragonal anatase (α-TiO_2), high-temperature stable tetragonal rutile (r-TiO_2) and middle temperature form orthorhombic brookite (b-TiO_2) [1]. The first α-TiO_2 and third b-TiO_2 easily transform into r-TiO_2 more than 1188 K and 923 K, respectively [2]; these temperatures depend much on their particle and crystallite sizes, purity and synthetic protocol [3]. Titanium dioxides have been widely used in the industry, that is textiles, electronics, wastewater treatment, and catalysis [4-6]. Recently, TiO_2 nanoparticles (TiO_2 NPS), have been attracting much attention due to their functional and physicochemical properties, such as, a white pigment and a personal skin care product (due to its brightness and high refractive index with high safety margin), and bactericidal agents (photocatalytic properties and its induced antimicrobial activity under UV radiation or visible light) [7-9]. Up to now, many papers and reviews concerning about toxicity mechanism have been published from the viewpoints of reactive oxygen species (ROS) [10-17], that is hydroxyl radical $\cdot$OH and superoxide anion O_2^- which are generated by hole-electron pairs in the valence and conduction bands of TiO_2, respectively. Their toxicity mechanism has

been explained by bio-cell wall damage and lipid peroxidation of membrane, and TiO_2 NP adherence to intercellular organelles and biological macro molecules [17- 21]. However, there have been no reports on anatase TiO_2 having microbial activity under dark conditions.

The authors have been investigating metal oxide powders which show strong antimicrobial activity in the shade. Biocompatible zinc oxide also has been interested due to its microbial toxicity. However, its activity is much lower than TiO_2 NP. Recently, it has been conducted that ZnO powders have been prepared by hydrothermal treatment in zinc nitrate aqueous solution with a concentration of 3 $mol \cdot L^{-1}$ at 443 K for 2.52×10^4 s, followed by re-oxidation heating at 873 K for 3.6×10^3 s in air. And then it has been cleared that thus obtained ZnO powders reveal strong antibacterial activity even under dark conditions [22-24]. During investigation of antibacterial ZnO study, the authors found that i) among commercially available TiO_2 powders, high-purity (≥99.0%) anatase (α-TiO_2) can submit much ROS in the dark, but rutile (r-TiO_2) does not, ii) among them, ROS has been submitted from α-TiO_2 doped with a small amount of K or P.

Then, we started to investigate the relationship between the amount of ROS and the contents of K, P, and combined doped (co-doped) K and P, from the view point of their microstructure and physicochemical properties. Finally, we have found that anatase (α-TiO_2) powders which can submit a lot of ROS in the dark have been prepared; the amounts of ROS are much higher than our previous antibacterial ZnO powders, and their preparation process is much more simple than antibacterial ZnO.

The present paper treats the physicochemical properties in relation with the microbial toxicity of thus prepared anatase (α-TiO$_2$) as a function of impurity contents and its doping method.

5.2 Experimental procedure

5.2.1 Doped TiO$_2$ powder preparation

As shown in Fig. 5-1, fine anatase-type TiO$_2$ powder (W-4038, 99.92% of purity, Sakai Chemical Industry Co., Ltd., Osaka, Japan) with a BET surface area S_A of 55.1 m^2/g, $i.e.$, particle size P_s of 0.0280 µm, calculated from both S_A and theoretical density (D_x) of 3.895 Mg/m^3 (PDF: #21-1272), was used as the starting material. 0.1 mol of this powder and a certain amount of KHCO$_3$ (Sigma Aldrich, Japanese agency of Nacalai Tesque Chemicals, Kyoto, Japan, 99.7%) and (NH$_4$)$_2$HPO$_4$ (Sigma Aldrich, ≥98%) with various inner atomic ratios of (0.01~10.0 at%) K or (0.01~10.0 at%) P as dopants shown in Table 1 were added and mixed together in 1.5×10^{-5} m^3 (15 mL) ethanol for 9.0×10^2 s at room temperature. The mixtures were dried at 393 K for 4.32×10^4 s, and then heated at 973 K for 3.6×10^3 s in air.

<O$_2$ heating> In order to reduce the oxygen deficiency, which will be described later, some various amount of K and P single and co-doped TiO$_2$ powders were heated in O$_2$ at 973 K for 3.6×10^3 s.

The flowchart contains:

- 0.1 mol of **α-TiO₂** (≥99.93% purity)
- +
- KHCO₃ and (NH₄)₂HPO₄ with certain inner atomic fraction of **(K:P)**
- Wet mixing in 15 mL Et-OH
- 9.0×10^2 s, room temperature
- Drying (393 K - 4.32×10^4 s)
- Re-oxidation 973 K/3.6×10^3 s in air, O₂
- Doped TiO₂
- **Evaluation:**
  - XRD (Smartlab), SEM (JSM-7001FD), BET (Tristar II), CL(CLD-100FC), Oxygen-nitrogen analyzer (EMGA-620W/C), XPS (ESCA3057, ULVAC-PHI), XFS (ZSX Primus IV), XAFS (Aichi SR)
  - Bio-test (*Escherichia coli*)

Fig. 1 α-TiO₂ W-4037
$S_A = 55.1$ m²/g
$D_s = 3.895$ Mg/m³
$P_s = 0.0280$ μm

Fig. 5-1 Preparation procedure and evaluation.

5.2.2 Evaluation

5.2.2.1 Physicochemical property

X-ray diffraction (XRD; Smartlab, Rigaku, Tokyo, Japan) analysis using Cu$K\alpha$ radiation (wavelength of 0.15418 nm) with a graphite monochromator was utilized for determining of the crystalline phases and lattice parameters. Microstructural observation with field emission-type scanning electron microscopes (FE-SEM; SU8020, Hitachi High-Technologies Corporation, Tokyo, Japan) was performed on the various TiO₂ powders. BET surface areas S_A of powders were measured using an automatic surface area and porosimetry analyzer (Tristar II, Micromeritics, Japanese agency Shimadzu, Kyoto, Japan) at room

temperature. X-ray fluorescence spectroscopy (XFS; ZSX Primus IV, Rigaku, Japan) analysis was applied to determine the contents of K_2O and P_2O_5 in mass% of the TiO_2 powders using cellulose (Aldrich Chemistry, particle size P_s of 20 μm) as an internal standard. X-ray photoelectron spectroscopy (XPS) or electron spectroscopy for chemical analysis (ESCA) (ESCA3057, ULVAC-PHI. Inc., Chigasaki, Kanagawa, Japan) was utilized to analyze the surface chemical state of TiO_2 powders with K and P as dopants. A monochromatic AlKα X-ray source (1486.6 eV) was used and operated at 150 W in a pressure of 1.333×10^{-12} Pa. All the binding energies were referenced to the $Au_{4f7/2}$ peak located at 84.2 eV attributed to the sputtered-Au on surface. Fourier transform infrared spectroscopy (FR-IR, Shimadzu IRAffinity, Shimadzu, Kyoto, Japan) was performed under the following conditions; measuring method is attenuated total reflection (ATR, Shimadzu MIRacle 10, Shimadzu) with the resolution capacity of 4.0 cm^{-1}, cumulated number is 20, measuring wavenumber domain is 600~4000 cm^{-1} at room temperature.

The local chemical structure around metal ions in anatase TiO_2 crystalline structure has also been investigated by extended X-ray absorption fine structure (EXAFS) studies and X-ray absorption near edge structure (XANES) studies both of which were performed at Aichi synchrotron radiation research center. The storage ring was operated at the ring-energy of 1.2 GeV and a stored current of 300 mA. Data were collected in transmission mode with two flat Si (311) crystals as a monochromator with a RH-coated double mirror (0.8 mrad) to reject the higher harmonics. The EXAFS data were processed using the computer program "Athena". The EXAFS functions were Fourier-transformed (FT) in the region 0.4-0.9 nm^{-1} to obtain the radial structure function (RSF). These are powerful tools for studying interatomic bonding- and electronic-states, and can provide information on the structure of a metal and an oxide ion,

and/or a reactant. However, the local structure around K and P ions in TiO_2 crystal are not well known. Instrument and attachment used for the band gap measurement. Integrating sphere: ISR-2200, UV-Vis spectroscopy: UV-2400PC.

In the order to determine oxygen deficiencies contained in TiO_2, *i.e.*, $TiO_{2-\delta}$, the following procedure was performed. (I) The weight of TiO_2 powder M_{TiO2} after heating at 573 K for 6.0×10^2 s in air was measured using a precision electric balance (here, this temperature and time was determined in terms of complete elimination of water adsorbed on the surface of TiO_2 using the DTA/TG). (II) The mass of oxygen content M_O of the same ZnO powder sample was measured using an Oxygen-Nitrogen Analyzer ("EMGA620W", Horiba Scientific, Kyoto, Japan). The average value of M_O was determined. (III) From this M_O value, the oxygen mole n_O was calculated. Then the mol of Ti, n_{Ti}, in the same sample was estimated from the following equation: $n_{Ti} = [M_{TiO2} - 16.00\times n_O - M_K - M_P] / 47.87$; here, 16.00 and 47.87 are atomic weights of oxygen and titanium, respectively and the contents of K and P (M_K and M_P) in the samples were determined by XFS measurement. The content of oxygen deficiency, δ, was determined by an equation of $n_O / n_{Ti} = 2 - \delta$.

5.2.2.2 Antibacterial property

Chemiluminescence (CL) [22-24] of TiO_2 powders (10 μmol) in a 0.25 mL (2.5×10^{-7} m^3) aqueous luminol solution (5.0 μmol·L^{-1}, 5.0×10^{-9} mol·m^{-3}) mixed with 3.0 mL (3.0×10^{-6} m^3) carbonic acid buffer solution (NaOH/NaHCO$_3$, pH=10.8) was observed under dark conditions using a CL detector (CLD-100FC, Tohoku Electronic Industrial Co., Ltd., Sendai, Japan). After dropping the luminol solution in a 1.2×10^2 s' warming up of the detector, the intensity of CL was integrated between $1.2\sim6.0\times10^2$ s. Chemiluminescence (CL) with

scavengers such as, 2-5 dimethyl furan (singlet oxygen, $^1O_2$, Fujifilm Wako Pure Chemical Co., Ltd., Osaka, Japan), nitro blue tetrazolium (superoxide, $\cdot O_2^-$, Nacalai tesque INC., Kyoto, Japan), 2-propanol (hydroxyl radical, $\cdot OH$, Nacalai tesque INC.), and riboflavin (hydrogen per oxide, H_2O_2, Fujifilm Wako Pure Chemical Co., Ltd.) measurements were performed at room temperature in the dark to identify the reactive oxygen species (ROS) of TiO_2 powders.

Antibacterial bio-test for representative TiO_2 powders was evaluated with a colony count method using *E. coli* bacteria on nutrient agar medium in a Na-P buffer solution. The penetrated culture of bacteria was kept at 309 K for 8.64×10^4 s in a laboratory incubator (following JIS Z 2801 test method). TiO_2 powders were added to a small amount of *E. coli* bacteria and mixed with 10 mL (1.0×10^{-5} m^3) Na-P buffer solution in the sunshade.

5.3 Results and discussion

5.3.1 Powder morphology

As expected, XRD analysis proved that after heating at 973 K for 3.6×10^3 s in air, TiO_2 powder of W-4038 was anatase and its BET surface area S_A was 15.0 m^2/g which value was much decreased from S_A=55.1 m^2/g of raw material. Fig. 5-2 shows SEM photographs of a) No. 18 TiO_2 doped with 5.0 at% P heated at 973 K for 3.6×10^3 s in air with S_A=35.6 m^2/g, here No.18 is the sample number in Table 5-1 (as will be shown later), afterward the same manner, b) No. 23 TiO_2 with 5.0 at% K with S_A=29.0 m^2/g, c) No. 35 TiO_2 with K:P=0.75:2.25 at% (K/P=1/3 atomic ratio) with S_A=28.3.0 m^2/g, and d) No. 38 TiO_2 with K:P=1.5:4.5 at% (K/P=1/3 atomic ratio) with S_A=21.0 m^2/g. From these S_A values, as described later, they showed also anatase crystal structure, the particle size P_s of TiO_2 doped with small amount of K or/and P were calculated to be P_s (No. 2)=0.103 μm, P_s (No. 18)=0.0433 μm, P_s (No.

23)=0.0531 μm, P_s (No. 35)=0.0544 μm and P_s (No. 35)=0.0734 μm using the same theoretical

density of anatase D_x=3.895 Mg/m^3 (PDF#21-1272). They are all submicron powders. It is

interesting that after heating, a small amount of P doped sample gives high S_A value (35.6), and

decreased gradually with the increase in the content of K or/and P, from 35.6 to 21.0 m^2/g. It is

easily noticed that P addition has high effect to suppress the particle growth at 973 K.
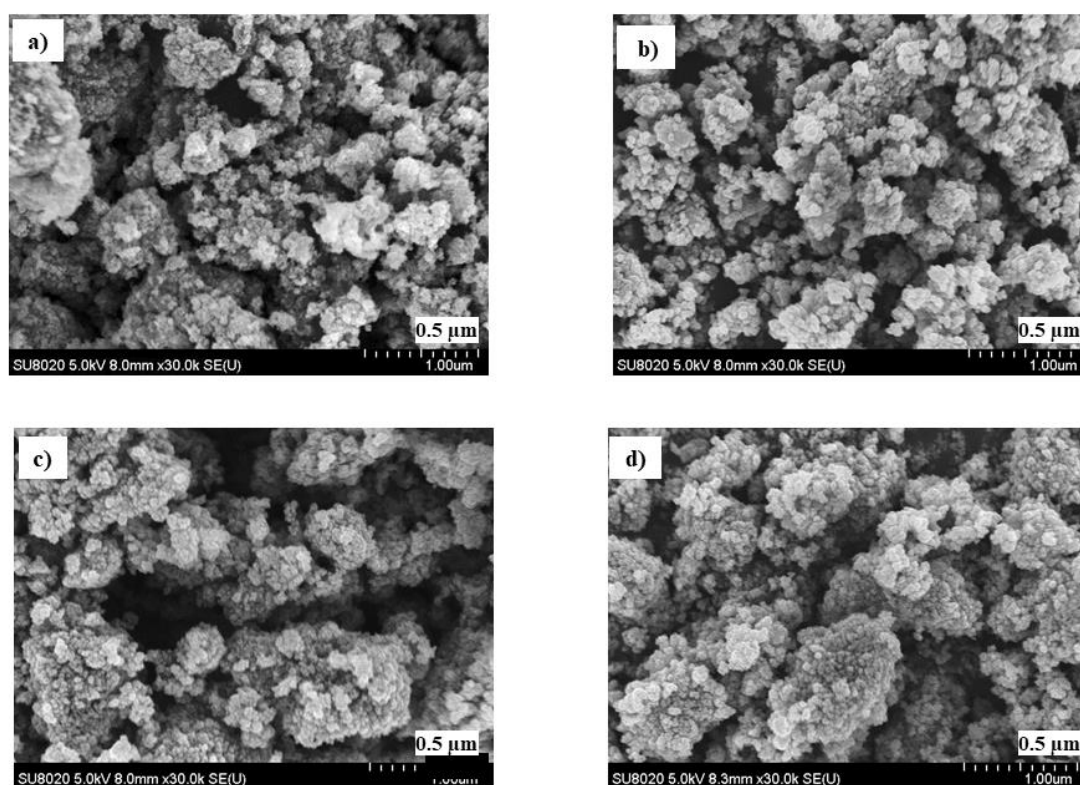
Fig. 5-2 SEM images of a) No. 18- K:P = 0:5 - S_A = 35.6 m^2/g – P_s = 0.0433 μm, b) No. 23-

K:P = 5:0 - S_A = 29.0 m^2/g – P_s = 0.0531 μm, c) No. 35- K : P = 0.75:2.25 - S_A = 28.3 m^2/g –

P_s = 0.0544 μm and d) No. 38- K : P = 1.5:4.5 - S_A = 21.0 m^2/g– P_s = 0.0734 μm.

Fig. 5-3 shows XRD patterns of the representative TiO$_2$ powders doped without and with a

small amount of K or/and P; a) No. 18 (5.0 at% P, b) No. 23 (5.0 at% K), c) No. 35

(K:P=0.75:2.25 at%), and d) No. 38 (K:P=1.5:4.5 at%). There are no other phases except anatase, even though the diffraction intensity of anatase is much scattered. Then lattice parameters *a* and *c* of anatase phase were estimated by the method of least squares using Si as internal standard.
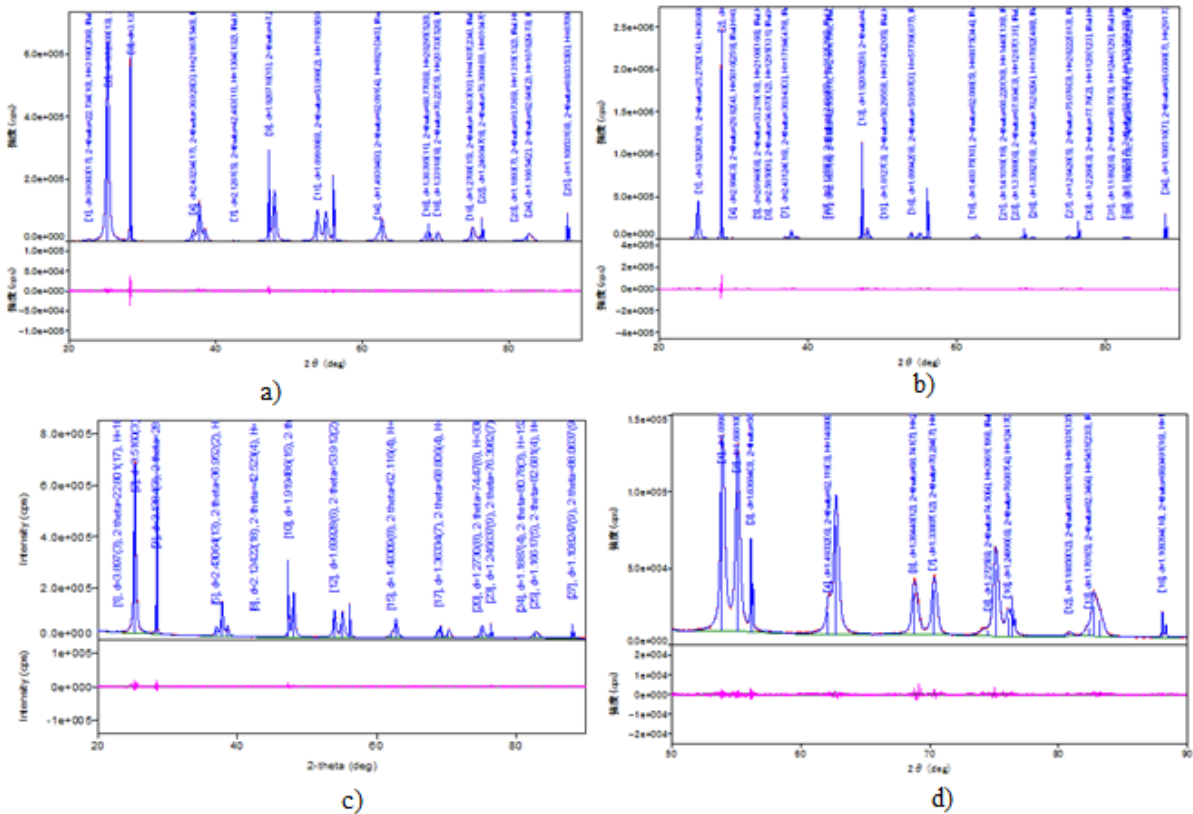
Fig. 5-3 XRD patterns of a) No. 18 (K : P = 0 : 5), b) No. 23 (K : P = 5 : 0), c) No. 35 (K : P = 0.75 : 2.25) and d) No. 38 (K : P = 1.5 : 4.5), red lines show the difference between I_{obs} and I_{calc} (I_{calc} is refered to PDF#21-1486).

Figures 5-4 and 5-5 show the changes of *a* and *c* values in anatase phase as function of input K and P, respectively. Here an "input" word has been newly introduced, the reason will be described later; (i) *a* of the combination of (1K+3P; K/P=1/3 atomic ratio), (ii) *a* of the single

addition of K, (iii) c of the single addition of K, and (iv) c of the combination of (1K+3P). It is clear that the single addition gives the decrease of both a and c values, especially, for examples, (ii) a and (iii) c of the single addition of K in Fig. 5-4. However, (i) a and (iv) c of the combination of (1K+3P) are almost constant in Figs. 5-4 and 5-5. They give relatively flat, or a small change in a and c for both K and P with increasing contents. On the other hand, the single additions of K and P, ii) and iii) in Figs. 5-4 and 5-5, assign the gradual decrease in a and c values, respectively, with increasing contents. This difference can be explained by that in the combined doping both 1) the average ionic radius $<r>$ [1·K$^+$+3·P^{5+}]/4=[1·r(K$^+$)$_{VI}$ =0.138 nm [25] + 3·r(P^{5+})$_{VI}$=0.038 nm]/4=0.063 nm [25], and 2) the average valence of guest metal ions of K and P [1·(1+)+3·(5+)]/4=4+] are adjusted to those of Ti^{4+} [r(Ti^{4+})$_{VI}$=0.0605 nm [25] and 4+]. On the contrary, the single addition of K or P to anatase TiO$_2$, both ionic radii and valence are much different, r(K$^+$)$_{VI}$=0.138 nm and r(P^{5+})$_{VI}$=0.038 nm are much larger or smaller than the ionic radii [r(Ti^{4+})$_{VI}$=0.0605 nm] of Ti^{4+}; the former is 228% and the later 62.8% and also the valence; 1+ and 5+, less or much more than 4+. In single addition of K$^+$, a decrease in a and c might come from the formation of oxygen deficiency: (Ti$_{1-x}$)$^{4+}$K$_x$$^{1+}$(O$_{2-\delta}$)$^{2-}$. On the other hand, in single addition of P^{5+}, (Ti$_{1-x}$)$^{4+}$P$_x$$^{5+}$(O$_{2-\delta}$)$^{2-}$, oxygen excess, a decrease in a and c might be mainly due to small ionic radius of P^{5+}.
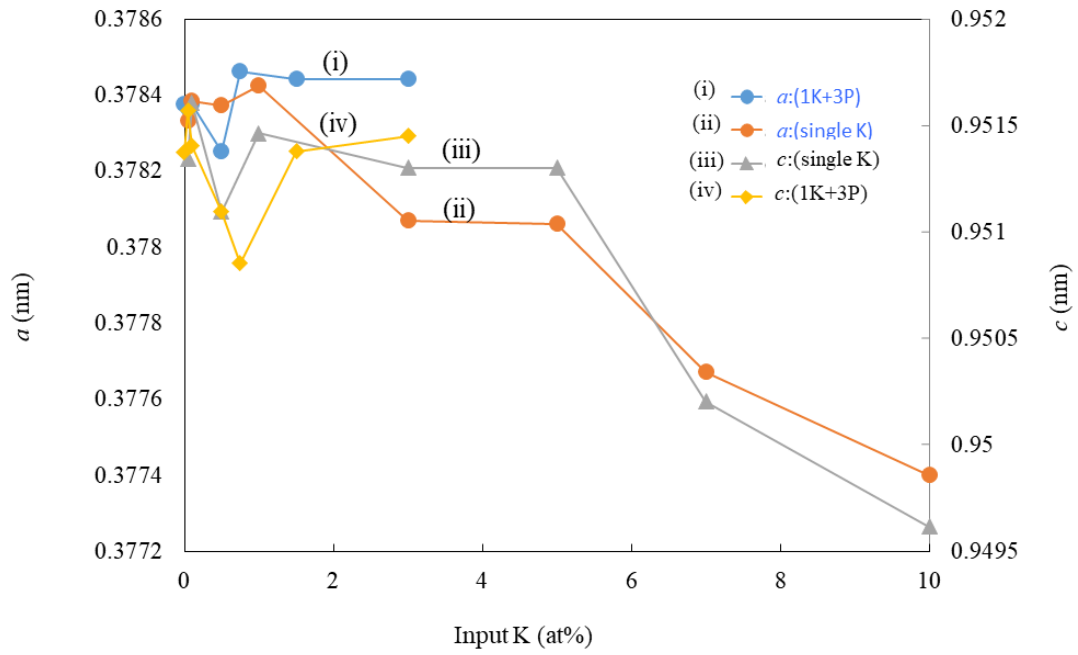
Fig. 5-4 Lattice parameters *a* and *c* of anataseTiO$_2$ doped with various contents of K (at%).
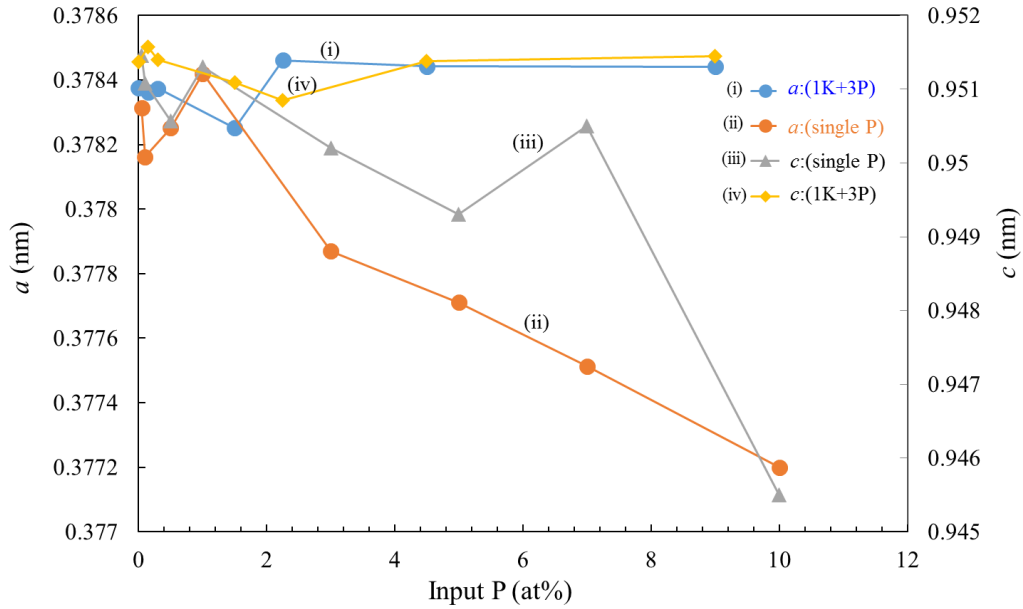
Fig. 5-5 Lattice parameters *a* and *c* of anataseTiO$_2$ doped with various contents of P (at%).

XFS measurement was conducted to identify the amount of dopants (K or/and P) in anatase samples after heat treatment at 973 K in air. It can be seen in Fig. 5-6 that there is no significant change in doped anatase powders with K as single addition ((a) in Fig. 5-6 (i)) and co-addtion:1K +3P ((b) in Fig. 5-6 (i)). However, in single P added samples ((a) in Fig. 5-6 (ii)), the content of P after heating is about 55% of input amount of P. This could be explained due to the evaporating of $(NH_4)_2HPO_4$ by heating. Otherwise, the contents of single K addition samples are nearly remained after heating. In (1K+3P) co-doped samples ((b) in Fig. 5-6 (ii)), about 90 at% of dopants remained. The reason could be explained because the positive charge of ion Ti^{4+} could be replaced by the same average charge of $(1K^+ + 3P^{5+})$ as already explained above.
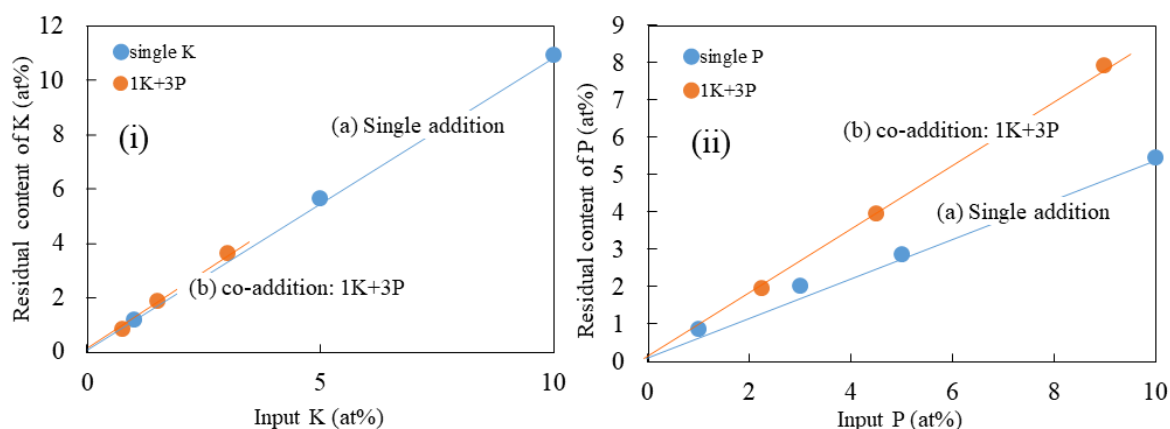
Fig. 5-6 Contents of doped (i) K and (ii) P of anatase as a function of input contents;

a) single addition and b) co-addition with the K/P=1/3 atomic ratio, 1·K+3·P.

b) In order to investigate the inner structure of doped TiO_2, XPS measurement has been performed (Fig. 5-7 (i)~(iv)). From these XPS spectra, there is not so much different among all doped samples (i) ~ (iii), except for O_{1s} spectra (iv). There are weak shoulder peaks of P

doped samples (No. 18, 35, 38, 41 in Table 5-1) around 532 eV which could be attributed to O in O-H or P-O. Then, we measured FT-IR spectra of doped anatase samples to check the presence or absence of O-H and P-O as shown in Fig. 5-8, it is clearly detected phosphate group (PO_4^{3-}) around 1000 cm^{-1}. However, OH group (OH$^-$) is not found.
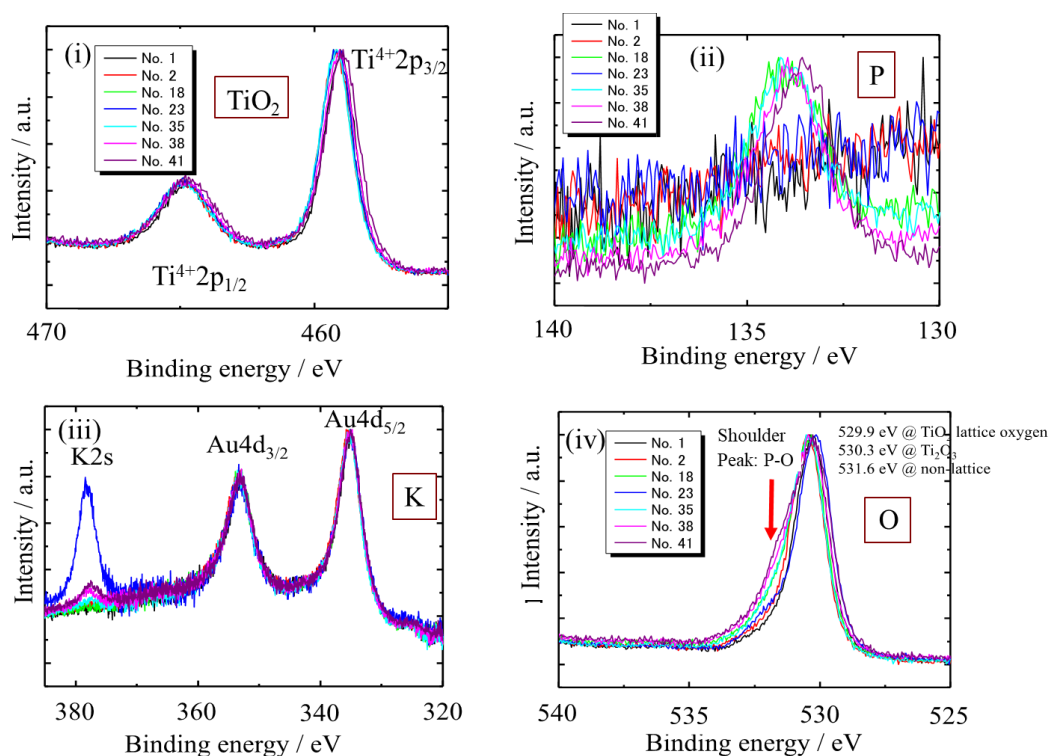
Fig. 5-7 XPS spectra of anatase powders doped with various K and P prepared by heating in air, corresponding to (i) TiO_2, (ii) P, (iii) K and (iv) O.
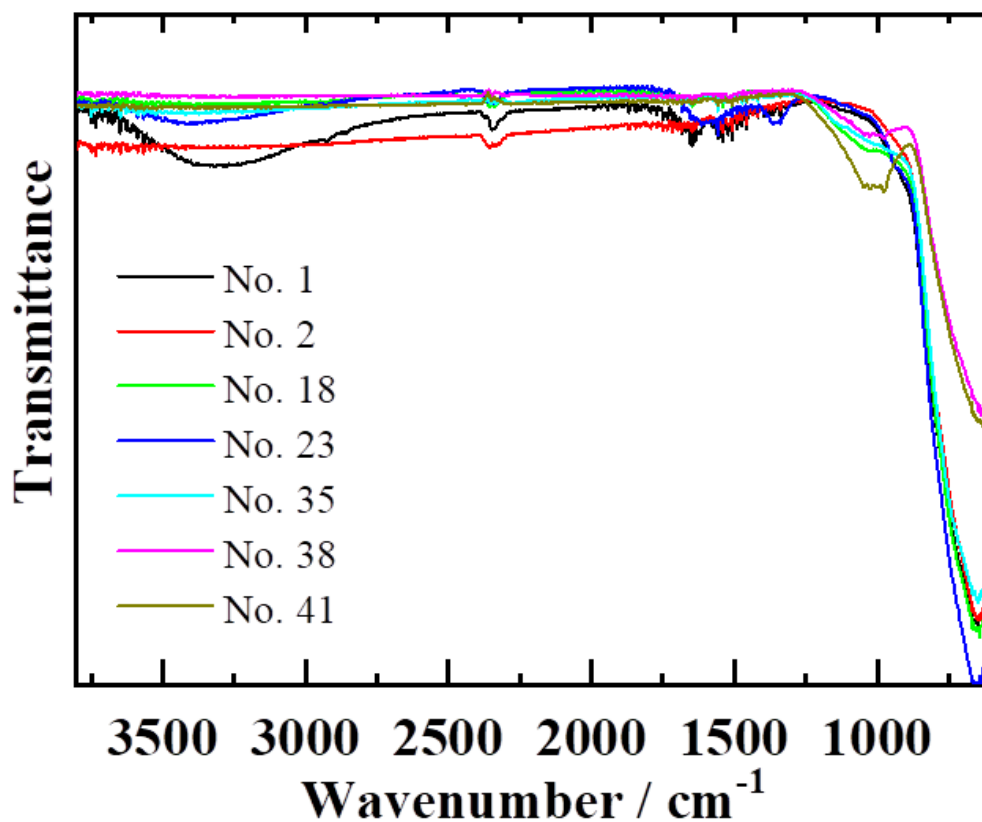
Fig. 5-8 FT-IR spectra of anatase doped with various K and P prepared by heating in air.

Furthermore, the inner structure of doped TiO_2 was studied by XAFS; the results are shown in Fig. 5-9; (i) local chemical environment around K^+ (XANES), all the spectra except for K_2SO_4 were measured by partial fluorescence yield (PFY) mode. From upper the 2nd to 5th curves, 5 at% K, 1K+2P, 1K+3P, 1K+4P (here K=0.75 at%), doped samples; small differences can be seen for the peak at ~3614 eV and the shoulder structure in the higher energy side of the peak. And (ii) shows local chemical environment around P^{5+} (XANES), as the same as (i) all the spectra except for $Ca_3(PO_4)_2$ were measured by PFY mode. K-edge XANES spectrum of P elements in α-TiO_2 doped with P is very similar to single addition of 5 at% P and compound

addition (1K+2P, 1K+3P, 1K+4P, K=0.75 at%). Therefore, the local chemical environment around P^{5+} is almost the same.
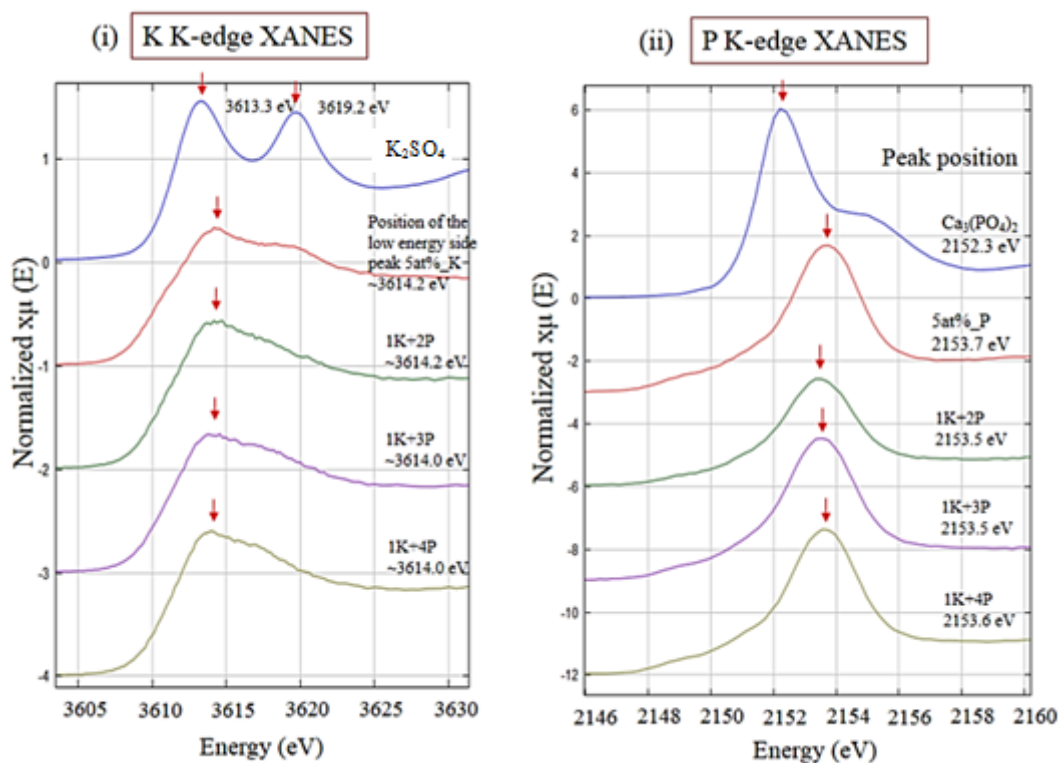
Fig. 5-9 K and P of K-edged XANES of anatase doped with various additives.

EXAFS results of P K-edge spectrum of (1K+3P, K=0.75 at%)-doped α-TiO₂ are shown in Fig. 5-10, Fourier transformation has been done k-range from 0.3 to1.25 nm (3.0-12.5 Å) (upper right side), then radial structural function (lower right side) was obtained. The distance between P-O ions was considered to be shorter than the distance of P-O in PO_4^{3-} from 0.145 to 0.15nm (1.45 to 1.50 Å). However, the coupling distance calculated based on the radial structure function obtained through the Fourier transform of EXAFS oscillation depends on a factor which called as phase factor. The details are unknown because it is several orders of

magnitude shorter than the actual coupling distance. Therefore, it is probably that O is present in the nearest neighbor of P and there is almost no ordering beyond that.
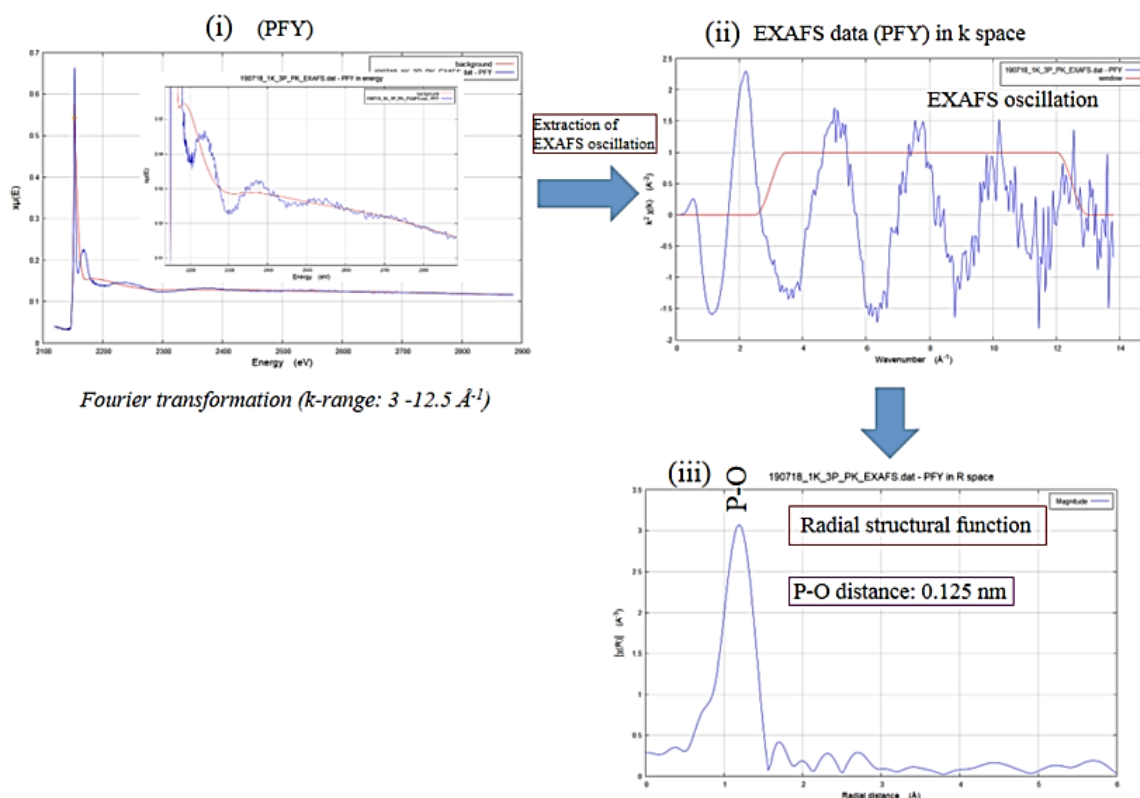
Fig. 5-10 P K-edge EXAFS of 1·K+3·P co-doped anantase.

Then, the band structure of undoped and doped anatase were evaluated using home-made measurement system. Band-gap energy E_g of doped α-TiO$_2$ powders are displayed in Fig. 5-11. These figures contain the function expressed （F (R)*hv^2 as a function of hv (eV) (h: Planck constant, v: wave number) to clarify their band-gap. Band gap of No. 38 (K: P = 1.5: 4.5 at%) and 41 (K: P = 3: 9 at%) are almost the same (3.44, 3.46 eV for the former and 3.43, 3.46 eV for the latter). However, their energy levels are smaller than those (3.61 and 3.64 eV) of No. 1 or 2, respectively, due to the co-doping (K and P) effect (this phenomenon is usually

called as red shift [26, 27]. The values of E_g of pure anatase (No.1 and No. 2) are much higher than those (3.2 ~ 3.3 eV) reported for the previous papers on anatase; this could be originated from the high-purity more than 99.92% and fine particle size P_s of 0.028 μm (around 30 nm). As it is very difficult to synthesize high-purity/single-phase/fine anatase powder, for example, very popular nano titanium dioxide powder (P_s ~ 20 nm), "P25" AEROXIDE®, consists 80% anatase and 20% rutile phases. Therefore, the smaller band gap ~3.2 to ~3.3 eV for the anatase powder could be explained due to small amount of impurities or single phase; because there are a few descriptions about their purity in the previous papers. The decrease in the band gap energy E_g of doped samples could be interpretable by the doping of K and P which increase their photoactivity. In the present study, pure anatase (No. 1 and heated 2) whose band gap value is only one. However, in the doped anatase, there could be more than one but a few energy gaps. Based on the viewpoints of E_g, it is difficult to explain the reason why these anatase can produce ROS even under dark conditions, as will be described, because these E_g values need much higher-frequency electromagnetic wave emission than UV.
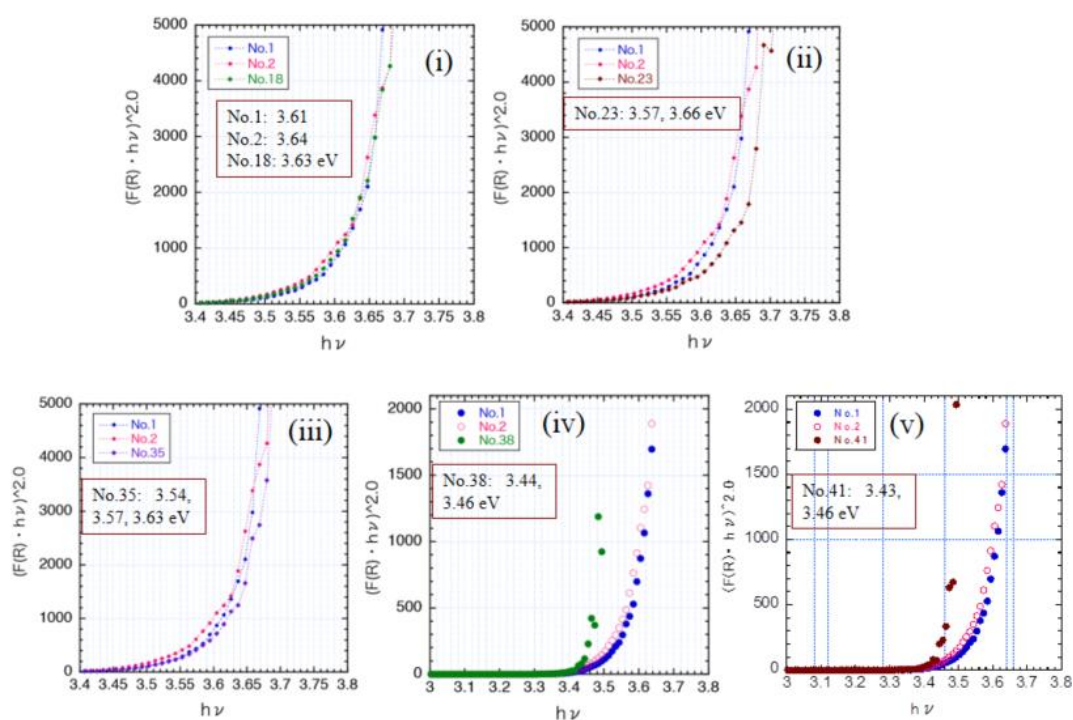
Fig. 5-11 Band gap energy spectra of anatase powders.

5.3.2 Bio-test results

The CL values of doped anatase powders heated at 973 K in air are shown in Table 5-1 and Fig. 5-12 as a function of the input amounts of K and P. It can be seen clearly that the high CL values around 150~250 kc (10^3 count) of K-doped anatase are achieved between 0.5 and 5.0 at%, however, those of P-doped anatase significantly increase from 102 to 834 kc (k:10^3 count) with increasing the amount of P from 0 to 12 at%. Based on ionic radius of P^{5+} (0.0380 nm) and Ti^{4+} (0.0605 nm) with the coordination number 6 [25], this could be accountable for the small P^{5+} could be able to replace Ti^{4+} in the crystal lattice. The replacement of Ti^{4+} by P^{5+} induces charge imbalance by the formation of Ti–O–P bonds [28, 29] that can help to reduce the recombination of the photogenerated e^-/h^+ pairs. Therefore, it might increase the possibility to form ROS from the surface of the powders. With single K addition, the CL value also

increased with increasing the amount of K up to 7 at%, then significantly decrease. As shown later, co-doped samples showed high antibacterial activity under dark conditions, which is consistent with their high and stable CL values.

Table 5-1 CL value (left) and sample number (right) of anatase powder doped with K and P

$\times 10^3$

Residual K (at%)

Input P (at%)	0	0.05	0.085	0.1	0.5	0.75	1.0	1.5	3.0	5.0	7.0	10.0	Residual P (at%)
12.0									429.7 42				(10.8)
10.0	838.6 14		691.586 15				366.860 16						5.5(9.0)
9.0									211.66 41				(8.1)
7.0	796.8 19												3.85
6.0							149.304 39	100.7 40					(5.4)
5.0	455.5 18												2.75
4.5								315.7 38					(4.05)
3.0	292.5 17					285.8 36		92.792 37					1.65(2.7)
2.25						169.4 35							(2.03)
1.5					261.5 29	233.3 34							(1.35)
1.0	140.2 10	25.58 33			167.5 11		349.4 12						0.55(0.9)
0.5	89.41 21	90.42 32									175.9 13		0.28(0.45)
0.3				176.7 28									(0.27)
0.15		109.83 27											0.0825
0.1	85.88 6	48.15 31	SA-120 151.1	66.35 7			85.41 8						0.06(0.09)
0.05	58.42 20	56.98 30									134.6 9		0.028(0.045)
0.045	SSP-M 156.4												0.025(0.041)
0	101.9 2	91.14 25		104.9 3	152.3 26		247.57 4		254.8 22	254.5 23	50.03 24	52.57 5	0
	0	0.05	0.085	0.1	0.5	0.75	1.0	1.5	3.0	5.0	7.0	10.0	

Input K (at%)
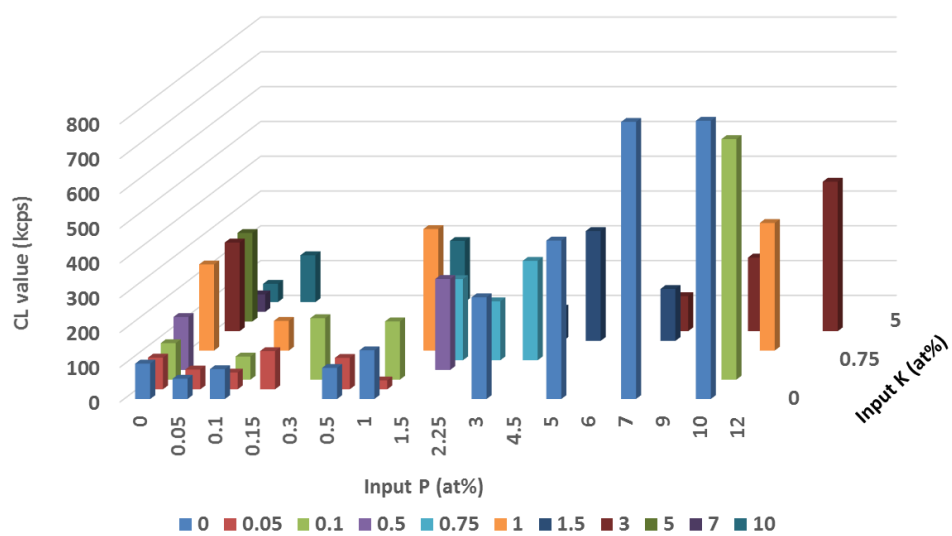
Fig. 5-12 CL values of anatase powders doped with K and P.

Besides, oxygen deficiencies of doped anatase powders heated in air were measured as shown in Fig. 5-13. After doping with various contents of K or/and P, those values were changed. This might also cause the change in the CL values of anatase powders.
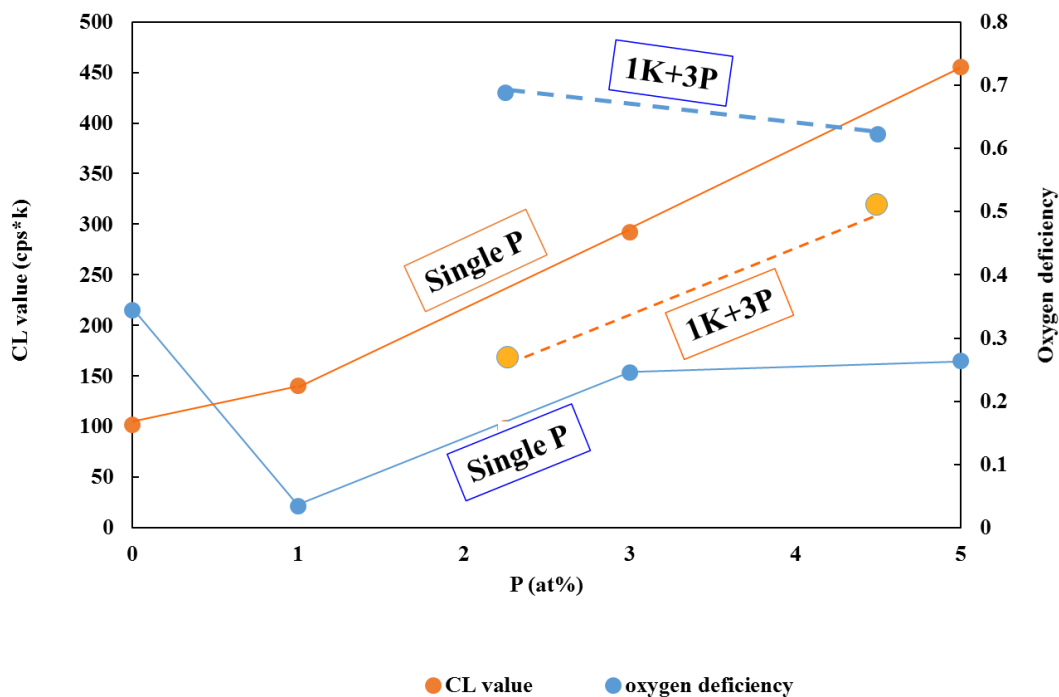
Fig. 5-13 Relation of oxygen deficiency and CL value on input P (at%).

CL-scavenger measurement in the sunshade was performed to determine which ROS generated from doped powders. Fig. 5-14 shows some representative examples of the CL curves of doped samples without/with scavenger. Based on the decrease in CL intensity of doped samples after injecting scavenger solution, it can be concluded that specific ROS was trapped by specific scavenger. In other words, doped anatase submitted specific ROS under dark conditions.
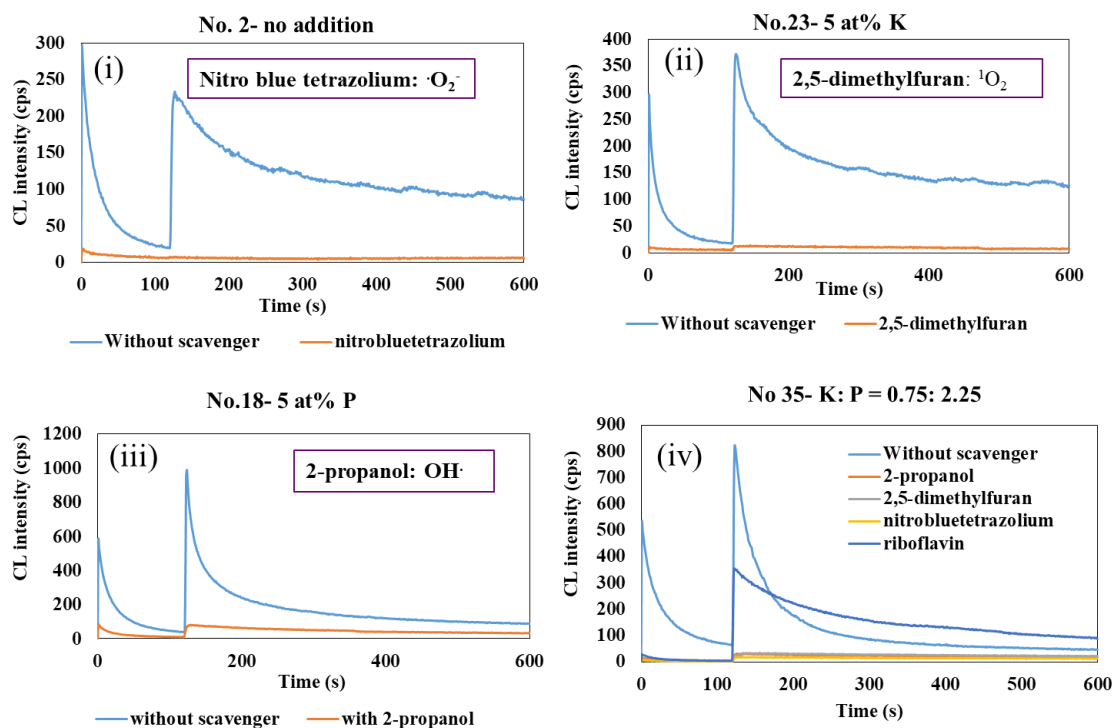
Fig. 5-14 CL curves of anatase powders heated in air with and without various scavengers.

Table 5-2 summarized which ROS is eliminated from each anatase powders, the ROS were detected by using the CL scavenger measurement. The differences in the type of ROS might determine the effect on their antibacterial properties. Besides, bio-test was conducted on *E. coli* bacteria at 309 K for for 8.64×10^4 s under dark conditions. Both single K and P addition gave the higher CL value with the higher amounts of dopants.

Table 5-2 Summary of ROS submitted from single doped and co-doped anatase powders

which heated in air and their bio-test results

K-line (at%)	0	0.05	0.5	1	3	5	10
ROS	$^\cdot O_2^-$	$^\cdot OH, ^\cdot O_2^-$	$^\cdot OH, ^\cdot O_2^-, ^1O_2$	$^\cdot O_2^-$	$^\cdot OH, ^\cdot O_2^-, ^1O_2$	$H_2O_2, ^\cdot O_2^-, ^1O_2$	$^\cdot O_2^-, ^1O_2$
Bio-test (%)*	0			46		95	

P-line (at%)	0	0.05	0.5	1	3	5	10
ROS	$^\cdot O_2^-$	$^\cdot O_2^-$	$^\cdot OH, ^\cdot O_2^-, H_2O_2$	$^\cdot O_2^-, ^1O_2$	$^\cdot OH, H_2O_2, ^\cdot O_2^-, ^1O_2$	$^\cdot OH, ^\cdot O_2^-, ^1O_2$	$^\cdot O_2^-, ^1O_2$
Bio-test (%)*	0			54		98	

K (at%)	P (at%)	ROS	Bio-test (%)*
0.75 **(1)**	1.5 **(2)**	$^\cdot OH, ^\cdot O_2^-$	
0.75 **(1)**	2.25 **(3)**	$^\cdot OH, H_2O_2, ^\cdot O_2^-, ^1O_2$	**97**
0.75 **(1)**	3.0 **(4)**	$^\cdot OH, ^\cdot O_2^-, ^1O_2$	

*: 2.3×10³ /mL E.Coli were tested with 0.1 g TiO₂ at 36°C for 24 h under dark conditions

The mechanism of the generation of ROS in doped anatase powders could be explained based on their non-stoichiometric as shown in Fig. 5-15, metal-rich structure [30] $Ti_{1+x}O_2$ ($x >$ 0) [31], x in the formula represents the amount of interstitial Ti_i which is the main source to produce ROS [23, 24]. After doping of K or/and P and heating at high temperatures, Ti_i in anatase will be created and increase. These Ti_i will react with oxygen as following reaction: Ti_i + 2O $\Leftrightarrow$ $Ti_i^{4\cdot}$ + 4e$^-$ + O$_2$. Then, ROS has been formed on the surface of TiO_2 as shown by the equations below which reveal antibacterial activity even under dark conditions.

$$Ti_i \rightarrow Ti_i^{4\cdot} + 4\ e^- \qquad\qquad ---------- (1)$$

$$Ti_i^{4\cdot} + 4\ H_2O \leftrightarrow 4\ {}^\cdot OH + Ti_i + 4\ H^+ \qquad ----------(2)$$

$$4\ H^+ + 4\ e^- + 2\ O_2 \rightarrow 2\ H_2O_2 \qquad ----------(3)$$
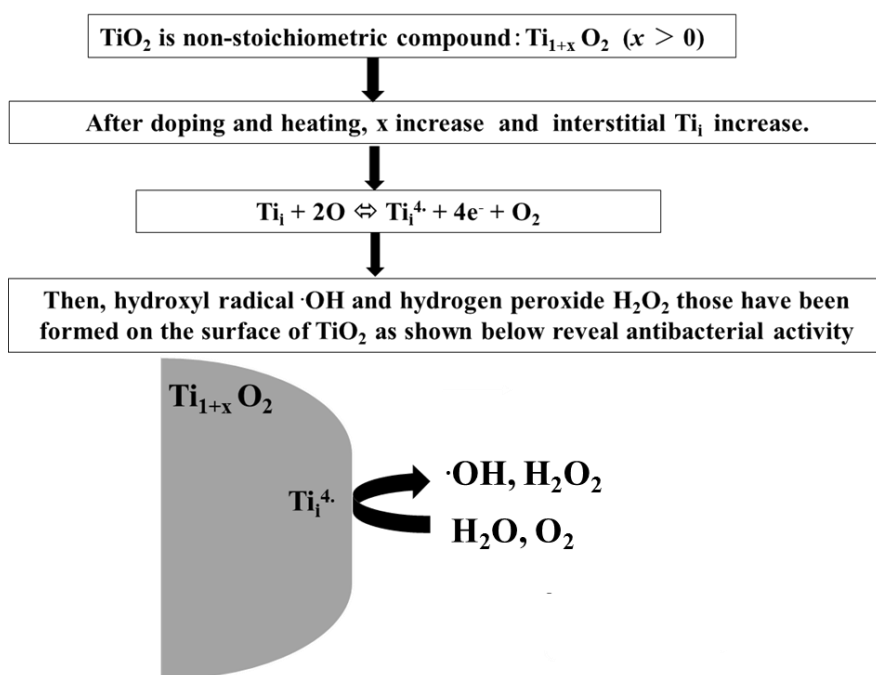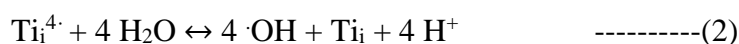
Fig. 5-15 Mechanism of antibacterial activity of TiO_2 powder.

These ROS can damage DNA chains of bio-cell due to the localizing interactions and meanwhile enhancing the membrane permeability of the cells.

After heating at 973K for 3.6×10^3 s in oxygen as shown in Fig. 5-16, co-doped (1K + 3P) anatase shows significantly high CL values comparing with those of other K or P single addition samples which heated in air at same conditions. This could be explained due to the change of oxygen deficiencies which are the main source of ROS generation [32].
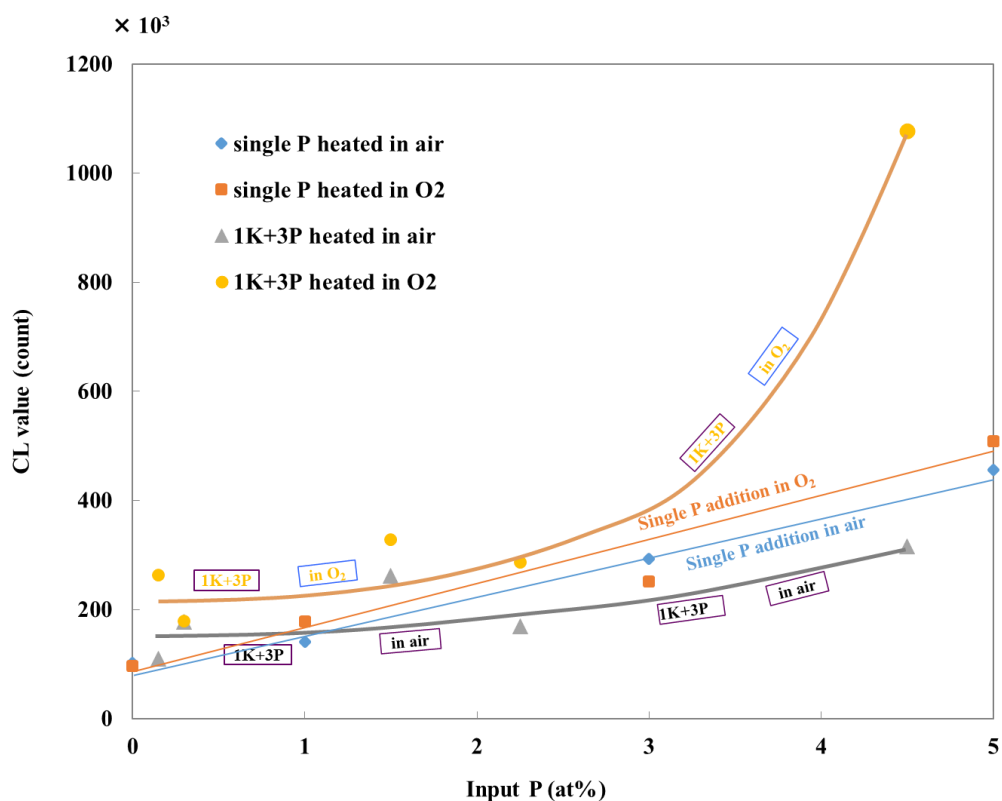
Fig. 5-16 CL values of anatase as a function of input P, which materials are heated at 973 K in air and O_2.

Then, ROS submitted from single doped and co-doped antase powders heated in oxygen atmosphere have been investigated by using CL-scavenger measurements as displayed in Fig.

5-17 and Fig. 5-18. Table 5-3 shows the change in type of ROS which submitted from those powders which heated in air and oxygen atmosphere. It is clear that there is little change in kinds of ROS of all anatase powders and the high oxygen-reduction potential ROS (as shown in Table 5-4 [33]) such as, hydroxyl radical, $\cdot$OH (2.80 V), singlet oxygen, $^1O_2$ (2.42 V) and hydrogen per oxide, H_2O_2 (1.77 V) are contained, here, it should be noted that hydroxyl radical, OH$\cdot$ can change into hydrogen per oxide, H_2O_2, spontaneously, as expressed by following equation:

$$2 \text{ OH}\cdot \leftrightarrow H_2O_2 \quad \text{-----------------(4)}$$
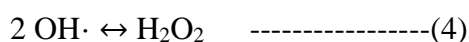
Thus, 1K+3P co-doped anatase heated in oxygen atmosphere reveal high antimicrobial activity under dark conditions.
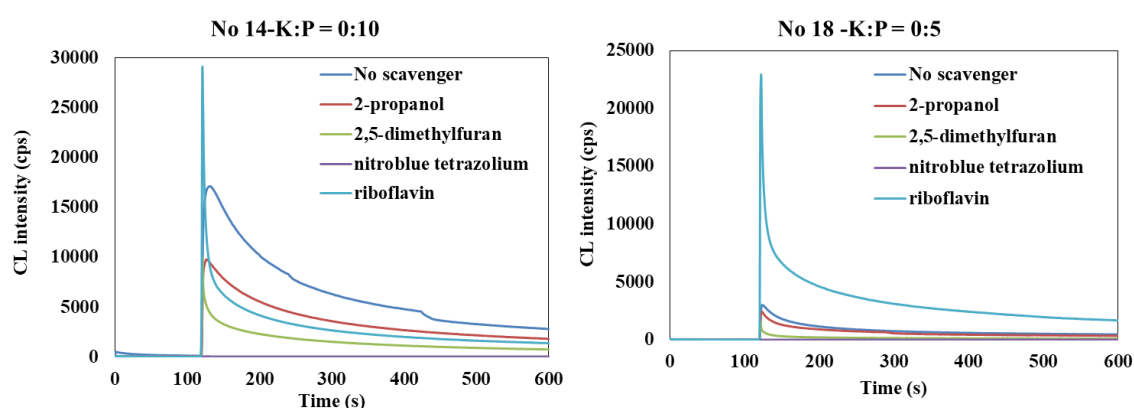
Fig.5-17 CL curves of single doped anatase heated in O_2 with and without various scavengers.
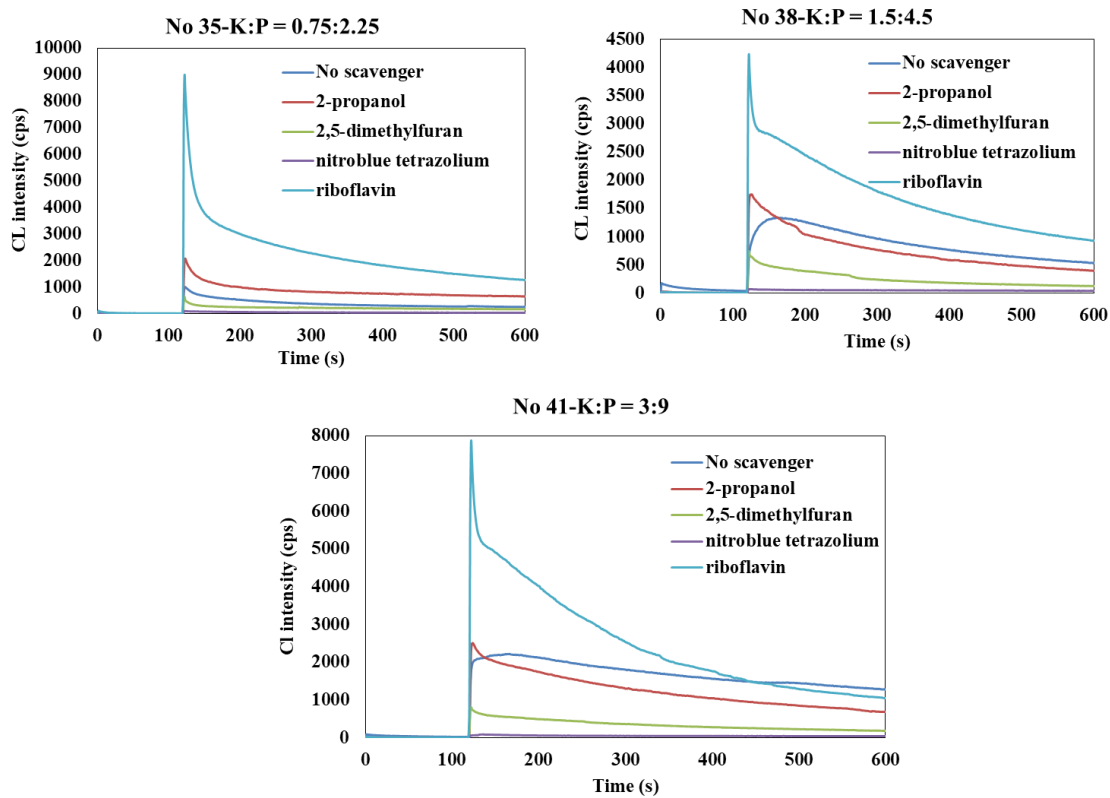
Fig. 5-18 CL curves of co-doped anatase heated in O_2 with and without various

scavengers.

Table 5-3 ROS change of anatase after O_2 heating

	Sample No.	K (at%)	P (at%)	ROS
Air	18	0	5	$\cdot OH, \cdot O_2^-, {}^1O_2$
O_2				${}^1O_2, \cdot O_2^-, \cdot OH$
Air	14	0	10	${}^1O_2, \cdot O_2^-, \cdot OH, H_2O_2$
O_2				${}^1O_2, \cdot O_2^-, \cdot OH, H_2O_2$
Air	35	0.78	2.25	${}^1O_2, \cdot O_2^-, \cdot OH, H_2O_2$
O_2				${}^1O_2, \cdot O_2^-, \cdot OH$
O_2	38	1.5	4.5	${}^1O_2, \cdot O_2^-, \cdot OH$
O_2	41	3	9	${}^1O_2, \cdot O_2^-, \cdot OH, H_2O_2$

Table 5-4 Oxidation-reduction potential of ROS [33]

ROS		Oxidation-reduction Potential (V)
Hydroxyl radical	$\cdot OH$	2.80
Singlet oxygen	${}^1O_2$	2.42
Ozone	O_3	2.07
Hydrogen peroxide	H_2O_2	1.77
Superoxide radical	$\cdot O_2^-$	1.70
Hydrogen chloride	HCl	1.49
Chlorine	Cl_2	1.36

5.4 Conclusions

1. Doped anatase which can submit high amount of ROS in the dark has been prepared. The preparation process is simple with a low cost.

2. CL values of co-doped (1·K+3·P) anatase samples after heating in O_2 at 973 K are highly improved *(5 times higher)* comparing to heating in air.

From Bio-test, doped (1·K+3·P) anatase submicron powder shows higher antibacterial activity than the others.

Acknowledgement

References

1. K. Fischer, A. Gawel, D. Rosen, M. Krause, A. A. Latif, J. Griebe, A. Prage, A. Schulze, Low-Temperature Synthesis of Anatase/Rutile/Brookite TiO_2 Nanoparticles on a Polymer Membrane for Photocatalysis, Catalyst, 7(2017), 209-222.

2. M. Catauro, E. Tranquillo, G. D. Poggetto, M. Pasquali, A. Dell'Era, S. V. Ciprioti, Influence of the Heat Treatment on the Particles Size and on the Crystalline Phase of TiO_2 Synthesized by the Sol-Gel Method, Materials, 11(2018), 2364-2374.

3. M. Pena, X. Meng, G. P. Korfiatis, C. Jing, Adsorption Mechanism of Arsenic on Nanocrystalline Titanium Dioxide, Environ. Sci. Technol., 40(2006), 1257-1262.

4. C. Y. Kuo, C. H. Wu, J. T. Wu, Y. R. Chen, Synthesis and characterization of a phosphorus-doped TiO_2 immobilized bed for the photodegradation of bisphenol A under UV and sunlight irradiation, Reac. Kinet. Mech. Cat., 114(2015), 753-766.

5. J. W. Liou, H. H. Chang, Bactericidal Effects and Mechanisms of Visible Light-Responsive Titanium Dioxide Photocatalysts on Pathogenic Bacteria, Arch. Immunol. Ther. Exp., 60(2012), 267-275.

6. U. G. Akpan, B. H. Hameed, Parameters affecting the photocatalytic degradation of dyes using TiO_2-based photocatalysts: A review, Journal of Hazardous Materials, 170(2009), 520-529.

7. T. Tachikawa, S. Tojo, M. Fujitsuka, T, Majima, Influences of Adsorption on TiO_2 Photocatalytic One-Electron Oxidation of Aromatic Sulfides Studied by Time-Resolved Diffuse Reflectance Spectroscopy, J. Phys. Chem. B, 108(2004), 5859-5866.

8. O. Carp, C.L. Huisman, A. Reller, Photoinduced reactivity of titanium dioxide, Progress in Solid State Chemistry, 32(2004), 33-177.

9. K. Sunada, T. Watanabe, K. Hashimoto, Studies on photokilling of bacteria on TiO_2 thin film, Journal of Photochemistry and Photobiology A: Chemistry, 156(2003), 227-233.

10. O. Akhavan, Lasting antibacterial activities of Ag–TiO_2/Ag/α-TiO_2 nanocomposite thin film photocatalysts under solar light irradiation, Journal of Colloid and Interface Science, 336(2009), 117–124.

11. A. A. Ashkarran, S. M. Aghigh, M. kavianipour, N. J. Farahani, Visible light photo-and bioactivity of Ag/TiO_2 nanocomposite with various silver contents, Current Applied Physics, 11(2011), 1048-1055.

12. C. Sun, Q. Li, S. Gao, L. Cao, J. K. Shang, Enhanced Photocatalytic Disinfection of

Escherichia coli Bacteria by Silver and Nickel Comodification of a Nitrogen-Doped Titanium Oxide Nanoparticle Photocatalyst Under Visible-Light Illumination, J. Am. Ceram. Soc., 93(2010), 531-535.

13. J. C. Yu, W. K. Ho, J. Lin, H. Yip, P. K. Wong, Photocatalytic Activity, Antibacterial Effect, and Photoinduced Hydrophilicity of TiO_2 Films Coated on a Stainless Steel Substrate, Environ. Sci. Technol., 37(2003), 2296-2301.

14. K. Sunada, Y. Kikuchi, K. Hashimoto, A. Fujishima, Bactericidal and Detoxification Effects of TiO_2 Thin Film Photocatalysts, Environ. Sci. Technol., 32(1998), 726-728.

15. F. M. Salih, Enhancement of solar inactivation of Escherichia coli by titanium dioxide photocatalytic oxidation, Journal of Applied Microbiology, 92(2002), 920-926.

16. A. Zaleska, Doped- TiO_2: A Review, Recent Patents on Engineering, 2(2008), 157-164.

17. P. H. Le, T. H. Le, T. N. Lam, T. N. H. Nguyen, V. T. Nguyen, T. C. T. Le, T. P. Pham, J. Leu, Enhanced Photocatalytic Performance of Nitrogen-Doped TiO_2 Nanotube Arrays Using a Simple Annealing Process, Micromachines, 9(2018), 618-630.

18. J. Hou, L. Wang, C. Wang, S. Zhang, H. Liu, S. Li, X. Wang, Toxicity and mechanisms of action of titanium dioxide nanoparticles in living organisms, Journal of Environmental Science, 75(2019), 40-53.

19. D. Venkatasubbu, R. Baskarb, T. Anusuya, C. A. Seshan, R. Chelliah, Toxicity mechanism of titanium dioxide and zinc oxide nanoparticlesagainst food pathogens, Colloids and Surfaces B: Biointerfaces, 148(2016), 600–606.

20. I. Iavicoli, V. Leso, L. Fontana, A. Berganaschi, Toxicological effects of titanium dioxide nanoparticles: a review of in vitro mammalian studies, European Review for Medical and Pharmacological Sciences, 15(2011), 481-508.

21. T. Santhoshkumar, A. A. Rahuman, C. Jayaseelan, G. Rajakumar, S. Marimuthu, A. V. Kirthi, K. Velayutham, J. Thomas, J. Venkatesan, S. K. Kim, Green synthesis of titanium dioxide nanoparticles using Psidium guajava extract and its antibacterial and antioxidant properties, Asian Pacific Journal of Tropical Medicine, (2014), 968-976.

22. K. Hirota, M. Sugimoto, M. Kato, K. Tsukagoshi, T. Tanigawa, H. Sugimoto, Preparation of zinc oxide ceramics with a sustainable antibacterial activity under dark conditions, Ceramics International, 36(2010), 497-506.

23. T. M. P. Nguyen, S. Hirota, Y. Suzuki, M. Kato, K. Hirota, H. Taniguchi, H. Yamada, K. Tsukagoshi, Preparation of ZnO Powders with Strong Antibacterial Activity under Dark Conditions, J. Jpn. Soc. Powder Powder Metall., 65(2018), 316-324.

24. T. M. P. Nguyen, K. Hirota, M. Kato, K. Tsukagoshi, H. Yamada, A. Terabe, H. Mizutani, Dependence of antibacterial activity of ZnO powders on their physicochemical properties, J. Jpn. Powder Powder Metall., 66(2019), 435-441.

25. R. D. Shannon, Revised Effective Ionic Radii and Systematic Studies of Interatomic Distances in Halides and Chalcogenides, Acta Crystallographica Section A, 32(1976), 751-767.

26. F. Huang, A. Yan, H. Zhao, Influences of Doping on Photocatalytic Properties of TiO_2 Photocatalyst, Semiconductor Photocatalysis-Materials, Mechanisms and Applications, Chapter 2 (2016), 31-80.

28. J. Ma, W. Li, N. T. Le, J. A. Díaz-Real, M. Body, C. Legein, J. Światowska, A. Demortiere, O. J. Borkiewicz, E. A. Konstantinova, A. I. Kokorin, N. Alonso-Vante, C. Laberty-Robert, D. Dambournet, Red-Shifted Absorptions of Cation-Defective and Surface Functionalized Anatase with Enhanced Photoelectrochemical Properties, ACS Omega, 4(2019), 10929-10938.

29. S. Y. Mendiola-Alvarez, M. A. Hernández-Ramírez, J. L. Guzmán-Mar, L. L. Garza-Tovar,

L. Hinojosa-Reyes, Phosphorous-doped TiO_2 nanoparticles: synthesis, characterization, and visible photocatalytic evaluation on sulfamethazine degradation, Environ. Sci. Pollut. Res., 26(2019), 4180-4191.

30. Z. Li, Y. Xin, W. Wu, B. Fu, Z. Zhang, Phosphorus Cation Doping: A New Strategy for Boosting Photoelectrochemical Performance on TiO_2 Nanotube Photonic Crystals, ACS Appl. Mater. Interfaces., 45(2016), 30972-30979.

31. K. W. Kim, E. H. Lee, Y. J. Kim, M. H. Lee, K. H. Kim, D. W. Shin, A relation between the non-stoichiometry and hydroxyl radical generated at photocatalytic TiO_2 on 4CP decomposition, Journal of Photochemistry and Photobiology A: Chemistry, 159(2003), 301-310.

32. S. Magder, Reactive oxygen species: toxic molecules or spark of life?, Critical Care, 10(2006), 208-215.

33. K. Asada, M. Nakao, K. Kakinuma, Manual of Measuring Reactive Oxygen Species, p.2, Kodansha Tokyo, Japan (2000).

CHAPTER 6

General Conclusions and Publication List

6.1 General conclusions

In this thesis, the author focused on characterizing the physicochemical properties of metal oxides such as ZnO, α-TiO$_2$ and doped α-TiO$_2$ (with K and P) and developing the preparation methods for enhancing the antibacterial activity of these materials. Moreover, the mechanism of their antibacterial properties under dark conditions was also discussed.

The main achievements of the work are summarized as follows:

In Chapter 2, ZnO powders which were prepared by hydrothermal treatment of 3 M Zn(NO$_3$)$_2$ at 443 K for 25.2×10^3 s, followed by re-oxidation treatment at 873 K for 3.6×10^3 s in air show high antibacterial activity on various kinds of bacteria even in the shade of sun. Ball-milling process under optimized conditions of milling time (3.6×10^3 s), ball size (2 mm diameter of YTZ ball) and rotating speed (400 rpm $\sim$ 41.89 rad/s) has significantly improved the antimicrobial activity due to the increase of the surface area and interstitial Zn into the (101) lattice plane of ZnO structure. This study proved that ZnO powders would be utilized as antibacterial agent for catching disease, such as *Pseudomonad aeruginosa, Salmonella bacterium*, and MRSA.

In Chapter 3, I investigated the antimicrobial activity of 4 kinds of ZnO powders described as follows: No.1 the antibacterial ZnO which the authors have developed and reveals sustainable microbial activity under dark conditions in previous study (Chapter 2); No. 2 is

commercially available ZnO powder (company product's name of "XZ-100F") which is the starting material for No.1; No. 3 is fine ZnO powder ("FINEX-30") and No. 4 is conventional fine ZnO powder. These powders were prepared by different methods. It is proved that the synthesis methods strongly affect on their physicochemical properties. Although, all ZnO powders revealed strong antibacterial activity under dark conditions, it was found that a new relationship between the antibacterial property and physicochemical properties from the values of the δ in nonstoichiometric compound $Zn_{1+\delta}O$ which observed by using photoluminescence (PL) spectra. As the δ indicates the content of Zn_i in the ZnO lattice, and this Zn_i has much influence on the submission of ROS. Therefore, No. 1 can produce high amount of ROS continuously under dark. From the application viewpoints, FINEX-30 or XZ-100F can be applicable for one and short time usage.

In Chapter 4, antibacterial ZnO powder with higher antibacterial power than our previous studies bas been obtained. Granules of ZnO which could be able to use as a water purifier were finally prepared. Moreover, for the evaluation of the tactile properties, the catalytic properties of ZnO were investigated by using acetaldehyde. From the results of CL measurement, it was obvious that the antibacterial activity of granule ZnO was increased with the addition of CNF, and from SEM images, they showed that the morphology of ZnO powders being close to granules was formed. Furthermore, from the catalytic ability tests using acetaldehyde, it could be confirmed that zinc oxide exhibits catalytic properties even in the dark conditions.

In Chapter 5, doped anatase was synthesized from high purity of anatase TiO_2 powder with various contents of K and P as dopants by wet-mixing method, followed by heating in air

or in O_2 at 973 K for 3.6×10^3 s. Then, the relationship between the amount of ROS and the contents of K, P, and combined doped (co-doped) K and P were discussed from the view point of their microstructure and physicochemical properties. It was found that doped anatase (α-TiO_2) powders could submit ROS even under dark and the amounts of ROS are much higher than the previous antibacterial ZnO powders. The preparation process is simple with low cost. Especially, CL values of co-doped ($1 \cdot K + 3 \cdot P$) anatase samples after heating in O_2 at 973 K were highly improved *(5 times higher)* comparing to heating in air. From Bio-test results, doped ($1 \cdot K + 3 \cdot P$) anatase sample showed higher antibacterial activity than the others.

6.2 Publication list

Chapter 2

T. M. P. NGUYEN, S. HIROTA, Y. SUZUKI, M. KATO, K. HIROTA, H. TAGUCHI, H. YAMADA, K. TSUKAGOSHI, "Preparation of ZnO Powders with Strong Antibacterial Activity under Dark Conditions", J. J. Powder Powder Metall. 65 [6](2018), 316-324.

Chapter 3

T. M. P. NGUYEN, K. HIROTA, M. KATO, K. TSUKAGOSHI, H. YAMADA, A. TERABE, H. MIZUTANI, "Dependence of antibacterial activity of ZnO powders on their physicochemical properties", J. J. Powder Powder Metall., 66(2019), 434-441.

Chapter 4

T. M. P. NGUYEN, Y. TOKUOKA, W. IMAI, K. HIROTA, M. KATO, K. TSUKAGOSHI, "The Study of Physicochemical Properties of Antibacterial ZnO Powder - Impurity Doping, Elution and Catalytic Properties", The Harris science review

of Doshisha University, 2019.

Chapter 5

T. M. P. NGUYEN, M. KATO, K. HIROTA, K. TSUKAGOSHI, A. TERABE, H. MIZUTANI, S. KANEHIRA, "Preparation of anatase titanium dioxide powder having strong antibacterial activity under dark conditions by co-doping of K and P", Materials Research Bulletin (submitted Oct 2019).

ACKNOWLEDGEMENT

First of all, I would like to express my deepest gratitude to my supervisor, Professor Ken Hirota for giving me the opportunity to come to Japan and conduct my Ph.D. course at Doshisha University. He has taught me so much about applied chemistry, especially inorganic materials and always guided me to the right research direction. Without his thoughtful advices and revisions, I would not be able to complete all my papers and dissertation this successfully. Besides, he never let me miss any chance to attend conferences, meetings as well as seminars to enhance my knowledge and experiences. From the first days to the end, he has always been there to give me good counsel, encourage and support me whenever I was in need or distracted from my goals so that I could fulfill all the requirements for my doctoral thesis.

Secondly, I would like to send my sincere appreciation to Professor Masaki Kato, who also constantly supported me with my research. He has offered so many constructive opinions for all of my presentations and papers. Especially, his encouragement was priceless to me during my most struggled moments with study and life in Japan.

I am very grateful to Professor Tsukagoshi, Professor Kitagishi, Dr. Taguchi, Ms. Toda and Ms. Morita at Doshisha University for their kindly supporting of my experiments and tests. Also, thank Dr. Yamada at Nara College, Dr. Kanehira at Microwave Chemistry Company, Dr. Yoshida at Meisui Company for their great collaboration and assistance on all the experiments during my doctor course.

Thank all my dear friends and labmates (in Inorganic Chemistry Laboratory, Doshisha University) for creating the best environment I could ask for to accomplish my mission.

Finally, I would like to give special thanks to my family and my dearest friends, Han Nguyen and Thao Nguyen, for giving me the strength I needed, believing in me and emotionally helping me during my toughest time.

Nguyen Phuong Thi Minh

March 2020